1979

Use of adjoint space models for predicting the response of a neutron detector to core parametric fluctuations

Lung-Rui Huang
Iowa State University

INFORMATION TO USERS

This was produced from a copy of a document sent to us for microfilming. While the most advanced technological means to photograph and reproduce this document have been used, the quality is heavily dependent upon the quality of the material submitted.

The following explanation of techniques is provided to help you understand markings or notations which may appear on this reproduction.

1. The sign or "target" for pages apparently lacking from the document photographed is "Missing Page(s)". If it was possible to obtain the missing page(s) or section, they are spliced into the film along with adjacent pages. This may have necessitated cutting through an image and duplicating adjacent pages to assure you of complete continuity.

2. When an image on the film is obliterated with a round black mark it is an indication that the film inspector noticed either blurred copy because of movement during exposure, or duplicate copy. Unless we meant to delete copyrighted materials that should not have been filmed, you will find a good image of the page in the adjacent frame.

3. When a map, drawing or chart, etc., is part of the material being photographed the photographer has followed a definite method in "sectioning" the material. It is customary to begin filming at the upper left hand corner of a large sheet and to continue from left to right in equal sections with small overlaps. If necessary, sectioning is continued again—beginning below the first row and continuing on until complete.

4. For any illustrations that cannot be reproduced satisfactorily by xerography, photographic prints can be purchased at additional cost and tipped into your xerographic copy. Requests can be made to our Dissertations Customer Services Department.

5. Some pages in any document may have indistinct print. In all cases we have filmed the best available copy.

University
Microfilms
International

300 N. ZEEB ROAD, ANN ARBOR, MI 48106
18 BEDFORD ROW, LONDON WC1R 4EJ, ENGLAND

HUANG, LUNG-RUI

USE OF ADJOINT SPACE MODELS FOR PREDICTING THE RESPONSE OF A NEUTRON DETECTOR TO CORE PARAMETRIC FLUCTUATIONS

Iowa State University PH.D. 1979

PLEASE NOTE:

In all cases this material has been filmed in the best possible way from the available copy. Problems encountered with this document have been identified here with a check mark ✓.

1. Glossy photographs ✓
2. Colored illustrations _____
3. Photographs with dark background ✓
4. Illustrations are poor copy _____
5. Print shows through as there is text on both sides of page _____
6. Indistinct, broken or small print on several pages _____ throughout _____
7. Tightly bound copy with print lost in spine _____
8. Computer printout pages with indistinct print _____
9. Page(s) _____ lacking when material received, and not available from school or author _____
10. Page(s) _____ seem to be missing in numbering only as text follows _____
11. Poor carbon copy _____
12. Not original copy, several pages with blurred type _____
13. Appendix pages are poor copy _____
14. Original copy with light type _____
15. Curling and wrinkled pages _____
16. Other _____

Use of adjoint space models for predicting the response of a neutron detector to core parametric fluctuations

by

Lung-Rui Huang

A Dissertation Submitted to the

Graduate Faculty in Partial Fulfillment of the

Requirements for the Degree of

DOCTOR OF PHILOSOPHY

Co-majors: Nuclear Engineering
Electrical Engineering

Approved:

Signature was redacted for privacy.

Signature was redacted for privacy.

In Charge of Major Work

Signature was redacted for privacy.

Signature was redacted for privacy.

For the Major Departments

Signature was redacted for privacy.

For the Graduate College

Iowa State University
Ames, Iowa

1979

TABLE OF CONTENTS

LIST OF TABLES

LIST OF FIGURES

Page

I. INTRODUCTION

The use of noise analysis for nuclear power plant malfunction diagnosis is appealing from both safety and economic points of view, because it does not disturb the normal plant operation nor need additional instrumentation. To ultimately find a place for noise analysis in power reactor operation, a thorough understanding of the power reactor noise field is necessary. However, based on the previous investigations [6, 26, 27, 36, 59, 60, 61, 66, 71], the physical origin of the possible noise sources strongly depends on the specific type of reactor under investigation. This is due to the fact that each type of power reactor has its own dynamic and transmission characteristics depending on its nuclear and thermohydraulic design [36, 66]. It is not very likely, therefore, that a sufficiently general power noise theory can be established which would be applicable to all of the different types of existing reactor systems. Although identification of the actual sources of noise is a first and necessary step, a quantitative understanding of the observed noise data is desirable. This is true especially if the power noise method is used as an on-line diagnostic technique to detect anomalous behavior or malfunction of reactor components [17, 51, 55].

Many attempts have been made to investigate the power reactor noise field driven by, in addition to the fission chain processes, intrinsic reactivity driving forces such as the stochastic generation of

steam bubbles in the coolant [18, 20], core coolant fluctuations [45, 64], mechanical vibration of fuel elements [17], inlet temperature fluctuations [1, 39, 51], etc. with a certain amount of success. One of the most important efforts today in power reactor noise analysis should be directed toward the development of an adequate mathematical model for the neutron detector response with respect to the above mentioned parametric fluctuations inside a nuclear power reactor. This work can aid in the verification of the analytic understanding of the response of a neutron detector to random noise sources and, hopefully, give more information on noise source identification. In order to obtain a good working model for the neutron detector response to random fluctuations, some experimental studies should be done in advance. As a first step, it is desirable to construct a simple phenomenological model based solely on experimental findings and physical intuition rather than on an analytic derivation. This model should then be improved in such a way that it can be supported by theoretical foundations such as neutron diffusion theory or transport theory. The ultimate goal is to develop a generalized detector model which is a function of detector size, strength and characteristic of the noise driving source, the type of detector, and type of nuclear reactor. This, however, is a very difficult goal to attain and one that will probably never be fully realized.

A phenomenological detector model has been constructed and has been successfully applied to the interpretation of the noise spectra obtained using in-core nuetron detectors in boiling water reactors (BWR)

[37, 74]. According to this model, the response of in-core neutron detectors to moderator density fluctuations is composed of a "global" and a "local" part. The local component at a given space point is directly proportional to the fluctuation of the steam content at that space point, while the global component is described by the point reactor model, that is, it is driven by reactivity fluctuations. Based on this model it is predicted that the local component changes rapidly along the vertical core axis and contains frequencies greater than one Hz, whereas the global component is slowly varying in space and dominates in the frequency range below one Hz. This model was improved later by theoretical support via diffusion theory [38, 40], and has proven to be a very good working model for interpretating the noise field in several reactor systems [18, 32, 63]. However, this model was only used to investigate the power noise behavior by analyzing the random fluctuations of neutron flux to noise sources, and the adjoint flux which relates the noise source to neutron detector signals has not been included in those studies.

The main use of the adjoint function in reactor theory is as an importance function in perturbation theory and variational methods [31, 42, 67]. Another field of application is in the determination of some integral quantities, which are otherwise difficult to calculate [23, 24, 57]. It has been shown [4, 25] that by an appropriate adjoint space formulation, the adjoint function can be interpreted as proportional to the response of a detector to a unit source. In reactor noise studies the fluctuations of the neutron detector response

due to noise sources is of main concern rather than the steady state response. By properly utilizing the adjoint space formulation, a neutron detector model, which includes the weighting effects of the adjoint flux and neutron flux, can be developed. Such a detector model was recently proposed by Dam [11, 12].

In spite of lacking a generalized formulation and numerical proof, Dam's detector model provides an important fundamental basis for a better understanding of the neutron detector behavior in a reactor noise field. However, the choice of detector size, noise source volume, and type of detector has been unspecified in this model. Much work is needed to improve this model to get a better analytic, or quantitative, understanding of the neutron noise field as observed from in-core detector measurements.

The purpose of this dissertation is twofold:

1. To develop a generalized model using the detector adjoint function for the detector response to random fluctuation of a reactor core parameter and thus expand on the work of Dam.
2. To support this model by physical interpretation as well as experimental verification and to provide an important fundamental base for better understanding of the noise field in a nuclear reactor.

A generalized detector model has been derived by combining the adjoint space formulation and reactor perturbation theory. Numerical calculations for this proposed model were obtained by utilizing a

modified two neutron energy group, three-dimensional diffusion code taking account of the finite dimensions of neutron detectors as well as noise sources. Experimental measurements were carried out with a water filled bubble generator installed in the central vertical stringer region of the ISU UTR-10 coupled-core reactor. The experimental investigation was concerned with the size of the neutron detector, detector locations relative to the noise source, volume of the noise source, void fraction and noise signal strength. The experimental data were analyzed in the frequency domain using a microcomputer based data acquisition system to calculate the power spectral densities of the detector signals in the frequency range of interest. Experimental results were compared with the theoretical model with an emphasis on a comparison of how well the detector response model agreed with the experimental observations.

II. LITERATURE REVIEW

The historical development of reactor noise analysis has been reviewed by Seifritz and Stegemann [66], Kosaly [36], Saito [59, 60, 61], Thie [71], and Booth [6] in recent years. Seifritz and Stegemann give a complete review of the status of noise analysis, both consider reactor noise and at-power reactor noise, up to 1971. Kosaly gave remarks on a few problems in the theory of power reactor noise that remained unsolved up to that time. Saito attempted to make as clear as possible, the physical-mathematical concepts for power reactor noise by supplementing it with practical physical facts. Thie commented in his review on the 1974 Specialist Meeting on Reactor Noise (SMORN-I) [26] that a depth of zero power reactor noise was exhibited; however, the power reactor noise (both theory and experiment) has not as a whole achieved a similar level of development. The state of the art of noise analysis has progressed considerably since the SMORN-I, the first specialist meeting in Rome, in which only the status of noise analysis in both zero-power and power reactors were covered. In contrast to the first conference, SMORN-II [27] placed emphasis on practical applications of noise analysis for the purpose of increasing the safety and availability of nuclear power plants. However, Booth [6] pointed out in his review on SMORN-II that a problem has arisen since 1974, namely, that stochastic modeling and simulation of power plants have not kept pace with measurement techniques. He suggested that much work is needed to improve the analytical understanding of power reactor noise.

He also strongly suggested more systematic experimental and theoretical investigations must be carried out in order to find out the real efficiency of the method both as a tool for reactor diagnostics and for studying power reactor dynamics in general.

A. Development of At-Power Reactor Noise Models

The investigation of the noise field in nuclear power reactors using in-core neutron detectors has been studied extensively by several authors [3, 37, 38, 40, 74]. Wach and Kosaly [74] developed a simple but space dependent theoretical model to find the transfer function between two neutron detectors placed in the core of a large BWR. The model was constructed in such a way that it is rather phenomenological and based largely on physical intuition. They assumed that the fluctuations of the neutron flux at a given space point inside the reactor are composed of two parts; a local part driven by a local disturbance and a global part driven by fluctuations of reactivity. For the sake of simplicity, it was assumed that the local disturbance in BWR's is due to the fluctuation of the number of steam bubbles at any given axial position. The basic idea of this model was to distinguish between local and global sources of reactor noise and to consider their joint effect. The transfer function between two in-core neutron detectors derived by this model was compared with the experimental results obtained from noise measurements at the Lingen Boiling Water Reactor [63]. It was found that this model not only successfully

predicted the position, in terms of frequency, of resonant structure in the magnitude of the measured transfer function but also gave information on estimating steam-void velocity inside the coolant channel.

This model was modified later by Kosaly et al. [37] to make it more conceivable physically. Firstly, the fluctuation of the steam-void content rather than the fluctuation of number of bubbles was considered as the driving source of the local component of the noise source. Secondly, different velocities were given at different detector positions rather than assuming a constant velocity of steam bubbles along the axis of the reactor, an assumption which is certainly not valid physically. However, the main shortcoming of this revised model was still its phenomenological character. Neither the transfer function which relates the noise source to neutron detector current nor the noise sources has been specified. Furthermore, there was no theoretical support for this model and the validity of this model could be only verified by the experimental results.

Further justification of this phenomenological model was carried out by Kosaly and Mesko [38, 40] again in 1976. Kosaly extended his early work and gave some theoretical support to the model by trying to relate the model to diffusion theory. No localized behavior was found using one-group diffusion theory for calculating the response of the neutron noise field to a propagating disturbance of moderator density. However, it was found that by using two-group diffusion theory, a term in the response to a propagating disturbance of moderator density

resulted which described a small volume of neutron detector sensitivity around the point of observation. By inspection of this model, it was found that the global term dominated in the cross power spectral density (CPSD) for frequency below 1 Hz. In the frequency region between 1 Hz and 10 Hz the local term became gradually more and more important. In this frequency region, the phase of the CPSD was found to approximately follow that of a pure time delay, namely $-\omega\tau_{12}$ (where τ_{12} is the transition time between two in-core detectors), and the gain was found to be independent of frequency. These predictions again agreed with experimental findings of several authors [63, 64, 69].

B. The Adjoint Space Formulations

The adjoint space formulation has been used for a variety of applications and the usefulness of these formulations was clearly demonstrated by several authors [22, 23, 24, 25, 42, 57, 67]. Greenspan [25] stated that even though the theory of the adjoint function in reactor theory is well-established, the scope and volume of applications of adjoint space formulations for the analysis of nuclear systems is scant. He assumed that many reactor physicists and engineers are not familiar enough with adjoint space formulations, or else, do not appreciate their potential benefits.

The relationship between adjoint-space and forward-space formulations was thoroughly developed by Selengut [67] for steady state problems. Lewins [42] extended Selengut's work to the time domain, established the physical meaning of a variety of adjoint functions,

derived the corresponding adjoint functions using physical consideration, and provided a comprehensive account of the theory of adjoint functions. One of his major contributions was the introduction of the time-dependent importance (adjoint) function, which was defined as the expected contribution of any neutron to a meter reading at time t_f; where t_f is the arbitrary time at which the meter reading was taken. In the case of multigroup diffusion theory, the ith group adjoint function may be defined, according to Lewins, as the expected contribution of a neutron of group i to the meter reading at time t_f.

Ronen [57] developed an application of adjoint functions for the calculation of the time integrated neutron density at a given point. The use of adjoint functions leads, according to Ronen, to a reduction of computational efforts. Instead of solving the time dependent transport equations, it is sufficient to solve one adjoint and one forward steady state equations. This technique was applied to a problem from time dependent reactor theory and tested by a numerical example. He concluded that it was possible to obtain certain information on the time transient by solving stationary problems.

Greenspan further generalized the adjoint space formulation to include the delayed neutron precursors [25]. He derived, using formal mathematical techniques, a generalized total importance balance condition and illustrated how this balance condition can be used for interpretating the physical meaning of different adjoint functions. He also provided the mathematical foundation for many different applications of the adjoint formulation. The approach used by Greenspan

showed that the applications of adjoint functions reported in the early literature [22, 23, 24, 47, 57, 67] were special cases of the total importance balance condition. Special contributions of this work, even without the introduction of new principles, included: 1) the generalization of the adjoint equation to include a precursor source term, 2) the definition of the importance function for a precursor detector, and 3) the generalization of the adjoint space formulation for the accumulated detector response.

By combining Greenspan's adjoint space formulation, Kosaly's revised reactor model and reactor perturbation theory, Dam [11] derived, using two group diffusion theory, an expression for the fluctuation of the response of a neutron detector with respect to reactor core parametric fluctuations in the frequency domain. He later extended his detector model to a transport theory formulation [12]. The adjoint fluxes, in his approaches, were assumed to be real within the frequency range of interest. A generalized formulation was not given to treat the adjoint flux as complex quantities. The choice of detector size, noise source size, type of detector and noise source has also been unspecified in this model.

To investigate the local-global behavior of the adjoint flux, instead of the fluctuation of the neutron flux, was the main goal of Behringer et al. [3] paper. It was found from their study using two-group diffusion theory, that the adjoint fluxes were also composed of two terms with different space relaxation characteristics. The term corresponding to a rapid relaxation in space was identified as the

local component while the other term was the global component. However, in his treatment a one-dimensional model was used, a point detector and a point noise source were assumed, and no experiment was carried out to prove the validity of his model.

Pazsit [54] followed Dam's model and provided semi-analytic calculations of the adjoint flux using a one-dimensional two-group diffusion model. In his treatment, again a point detector and a point vibrating absorber were assumed and the calculations were carried out for a slightly enriched, water moderated research reactor. Although his treatment lacks generality, his adjoint function calculations clearly indicated that the imaginary part of the adjoint functions were negligible as compared to the real part in the frequency range of interest. It was also shown that the response of a neutron detector to a moving absorber can be quite different than the response to an absorber of varying strength. This paper again demonstrates the utility of the adjoint formulation for describing the response of a detector to a core perturbation.

III. THE NEUTRON DETECTOR RESPONSE MODEL

A. The Adjoint Equations, Adjoint Flux and the Adjoint Operator

Since the concept of the adjoint flux, adjoint equation and adjoint operator has been used so extensively in this work, their basic definition and properties are reviewed briefly here.

Lewins [42] used the concept of a time-dependent importance function for interpretating the adjoint flux. This adjoint flux has the following physical interpretation:

Suppose the behavior of a reactor at time t_f is characterized by the reading of a single meter at that time. This meter may be connected to several detectors distributed throughout the reactor in an arbitrary manner. Each neutron in the reactor at time t_f makes contribution to the detector reading. Neutrons present in the reactor at times earlier than t_f will affect the meter reading through the accumulated contributions of the neutrons and their progengy from time t to t_f. Neutrons present in the reactor at times later than t_f make no contribution to the meter reading. The adjoint flux, i.e. the importance function $\psi(\vec{r},t)$, is then a time-dependent quantity which can be defined as the accumulated detection probability in the time period from t to t_f due to one neutron introduced at $\vec{r}$ and at time t. For multigroup diffusion theory, the ith group adjoint flux, $\psi_i(\vec{r},t)$, can be defined as the accumulated contribution to the meter reading due to one neutron of the ith group introduced at $\vec{r}$ and time t.

Certain properties of the importance function (the adjoint flux)

can be defined immediately from its definition. First consider two neutrons emitted at the same time but at different spatial locations. Near the outer surface, the neutron has a good chance of leaking out of the system without leaving progeny and therefore without affecting the meter. Hence the importance will be lower near the outer surface than for a neutron near the center. Now consider the relative contribution of two neutrons released at the same position but at different times. The neutron emitted earlier will have more contribution to the meter reading at a given time period (i.e. from t to t_f) than the second neutron. This is the characteristic change of sign of the first order time derivative in an adjoint equation. Although $\psi(\vec{r},t)$ is adjoint to the flux, it is not a flux type function and does not have the flux-type dimensions.

Consider the multigroup, time-dependent diffusion equations with an external source

$$L\underline{\phi}(\vec{r},t) + \underline{S}(\vec{r},t) = V^{-1} \frac{\partial}{\partial t} \underline{\phi}(\vec{r},t) \tag{3.1}$$

where L is the conventional multi-group diffusion operator and is a (GxG) matrix, $\underline{S}(\vec{r},t)$ is the (Gxl) external source vector, $\underline{\phi}(\vec{r},t)$ is the (Gxl) flux vector, and V^{-1} is a (GxG) diagonal velocity matrix.

The corresponding adjoint equations are defined as follows

$$L^{+}\underline{\psi}(\vec{r},t) + \underline{S}^{+}(\vec{r},t) = -V^{-1} \frac{\partial}{\partial t} \psi(\vec{r},t) \tag{3.2}$$

where L^{+} is the adjoint operator and is equal to the transpose of L. The adjoint source $\underline{S}^{+}(\vec{r},t)$, for the time being, is arbitrary. A useful

choice will be discussed later.

Further, the conventional boundary conditions are applied:

$$\underline{\phi}(\vec{r}_b,t) = 0 \tag{3.3a}$$

$$\underline{\psi}(\vec{r}_b,t) = 0 \tag{3.3b}$$

where $\vec{r}_b$ is the boundary surface of the reactor.

In accordance with Lewins [42] the following initial and final conditions are assumed:

$$\underline{\phi}(\vec{r},t_i) = 0 \tag{3.4a}$$

$$\underline{\psi}(\vec{r},t_f) = 0. \tag{3.4b}$$

These conditions imply that the flux equations define an initial value problem, whereas the adjoint equations define a final value problem.

In multigroup diffusion theory, both the operator L and the flux are real; the adjoint operator, L^+, is then defined by the requirement that

$$\langle \underline{\psi}, \underline{L\phi} \rangle = \langle \underline{\phi}, \underline{L^+\psi} \rangle \tag{3.5}$$

which leads, after some manipulation, to

$$L^+ = L^T. \tag{3.6}$$

The notation <,> stands for the inner product between two vectors:

$$\langle A, B \rangle = \int_{\vec{r}} \underline{A}^T \underline{B} d\vec{r} . \tag{3.7}$$

Multiplying Equation (3.1) by $\underline{\psi}(\vec{r},t)$ and Equation (3.2) by $\underline{\phi}(\vec{r},t)$ yields

$$\langle \underline{\psi}, L\underline{\phi} \rangle = \langle \underline{\psi}, -S \rangle + \langle \underline{\psi}, v^{-1} \frac{\partial}{\partial t} \underline{\phi} \rangle \tag{3.8}$$

$$\langle \underline{\phi}, L^{+}\underline{\psi} \rangle = \langle \underline{\phi}, -S^{+} \rangle - \langle \underline{\phi}, v^{-1} \frac{\partial}{\partial t} \underline{\psi} \rangle. \tag{3.9}$$

Subtracting Equation (3.8) from Equation (3.9) and integrating over all t gives

$$\int_t [\langle \underline{\psi}, \underline{S} \rangle - \langle \underline{\phi}, \underline{S}^{+} \rangle] dt$$

$$= \int_t [\langle \underline{\psi}, v^{-1} \frac{\partial}{\partial t} \underline{\phi} \rangle + \langle \underline{\phi}, v^{-1} \frac{\partial}{\partial t} \underline{\psi} \rangle] dt$$

$$= \int_t \int_{\vec{r}} \underline{\psi}^T \frac{\partial}{\partial t} v^{-1} \underline{\phi} d\vec{r} dt + \int_t \int_{\vec{r}} \underline{\phi}^T v^{-1} \frac{\partial}{\partial t} \underline{\psi} d\vec{r} dt. \tag{3.10}$$

Recall that the transponse of a scalar is equal to itself. This leads to the following results:

$$\underline{\phi}^T v^{-1} \frac{\partial}{\partial t} \underline{\psi} = (\underline{\phi}^T v^{-1} \frac{\partial}{\partial t} \underline{\psi})^T$$

$$= (\frac{\partial}{\partial t} \underline{\psi})^T (v^{-1})^T (\underline{\phi}^T)^T$$

$$= \frac{\partial}{\partial t} \underline{\psi}^T v^{-1} \underline{\phi}$$

$$= (\frac{\partial}{\partial t} \underline{\psi}^T) \underline{N} \tag{3.11}$$

where $v^{-1} = (v^{-1})^T$ for a diagonal matrix and $\underline{N}$ is the (Gxl) neutron density vector.

Substituting Equation (3.11) into Equation (3.10), after some manipulations, yields

$$\int_{t_i}^{t_f} [\langle \underline{\psi}, \underline{S} \rangle - \langle \underline{\phi}, \underline{S}^{+} \rangle] dt$$

$$= \langle \underline{\psi}, N \rangle \Big|_{t_f} - \langle \underline{\psi}, \underline{N} \rangle \Big|_{t_i} . \tag{3.12}$$

Applying the time conditions stated in Equations (3.4a) and (3.4b) to Equation (3.12) yields

$$\int_{t_i}^{t_f} dt \langle \underline{\psi}, \underline{S} \rangle = \int_{t_i}^{t_f} dt \langle \underline{\phi}, \underline{S}^{+} \rangle . \tag{3.13}$$

If the adjoint source, $\underline{S}^{+}$, is chosen as $\underline{\Sigma}_d$, the detector cross section, Equation (3.13) can be rewritten as

$$\int_{t_i}^{t_f} dt \langle \underline{\psi}, \underline{S} \rangle = \int_{t_i}^{t_f} \langle \underline{\phi}, \underline{\Sigma}_d \rangle . \tag{3.14}$$

An important physical interpretation of the ith energy group adjoint flux (or function) can be obtained by assuming that

$$\underline{\Sigma}_d = [\Sigma_{d_1}, \Sigma_{d_2}, \ldots \Sigma_{d_G}]^T \tag{3.15a}$$

= The detector cross section

and

$$\underline{S} = [0,0,\ldots,S_i,\ldots 0]^T$$

$$= [0,0,\ldots,1,\ldots,0]^T \delta(\vec{r}-\vec{r}_s)\delta(t-t_i) \tag{3.15b}$$

= A point source of ith group neutrons pulsed at spatial location $\vec{r}_s$ and at time t.

Substituting Equations (3.15a) and (3.15b) into Equation (3.14), the ith energy group adjoint function is obtained as follows

$$\psi_i(\vec{r}_s, t_i) = \int_{t_i}^{t_f}\int_{\Delta\vec{r}_d} [\sum_{i=1}^{G} \Sigma_{di}\phi_i(\vec{r},t)]d\vec{r}dt \qquad (3.16)$$

where $\Delta\vec{r}_d$ is the detector volume.

Equation (3.16) states that the ith energy group adjoint function is the number of neutrons counted by the detector in the period from t_i to t_f as a result of one neutron of the ith energy group introduced at spatial location $\vec{r}_s$ and time t_i. This adjoint function can be referred to as the accumulated detection probability which is the same definition given by Lewins [42].

A well-known special case of Equation (3.14), which is called the detector response to different sources, can be obtained by assuming that there is no time dependence in Equation (3.14). In this case Equation (3.14) reduces to

$$<\underline{\psi}(\vec{r}), \underline{S}(\vec{r})> = <\underline{\phi}(\vec{r}), \underline{\Sigma}_d(r)>. \qquad (3.17)$$

Equation (3.17) has been derived directly from the steady state diffusion equations and thoroughly discussed by Selengut [67]. The right hand side of Equation (3.17) has a very clear physical interpretation whereas the left hand side of Equation (3.17) gives the most convenient formulation for calculating the effect of different sources (or the components of a given source) on a given detector response.

If both the operator and function are complex (as they are in this

research), the definitions given in Equation (3.5) for the adjoint operator and in Equation (3.7) for the scalar product are no longer applicable. The adjoint operator, L^+, must satisfy the fundamental definition [47] that

$$\langle L\underline{\phi}, \underline{\psi}\rangle = \langle \underline{\phi}, L^+\underline{\psi}\rangle \tag{3.18}$$

and the inner product is defined by

$$\langle \underline{A}, \underline{B}\rangle = \int_{\vec{r}} (\underline{A}^T)^* \underline{B} d\vec{r} \,. \tag{3.19a}$$

Note that the inner product is in general a complex quantity

$$\langle \underline{A}, \underline{B}\rangle^* = \langle \underline{B}, \underline{A}\rangle. \tag{3.19b}$$

From Equations (3.18) and (3.19), the adjoint operator L^+ is equal to the complex conjugate of the transpose of L

$$L^+ = (L^T)^*. \tag{3.20}$$

The definition of the adjoint operator given by Equation (3.5) has been used very extensively in reactor theory [4, 25]. This is because in reactor theory most of the calculations are carried out in the time domain and in that case both the operator (diffusion operator or transport operator) and the flux are real. However, in reactor noise theory, the most convenient formulation was found to be in the frequency domain and in this case both the operator and the function are complex. Therefore, Equations (3.18), (3.19) and (3.20) must be used for noise analysis in the frequency domain.

Note here that Equation (3.18) and Equation (3.19) can be reduced to Equation (3.5) and Equation (3.6), respectively, if both the operator and the function are real (or the inner product is real).

B. Derivation of the Detector Response Model

The objective of this section is to develop a generalized neutron detector response model with respect to core parameter fluctuation. The adjoint space formulation via perturbation theory and neutron diffusion theory is utilized. The assumptions made for this model are as follows:

1. Zero power reactor effects are neglected; i.e., if various parameters of the reactor system did not fluctuate, the neutron flux would not fluctuate.
2. Feedback effect are neglected.
3. The fluctuation in macroscopic parameters (such as δD, $\delta \Sigma$) are assumed to be small, so that first-order perturbation theory is applicable.
4. Neutron noise is driven by certain perturbations affecting the neutron field via the fluctuation of macroscopic group constants.

1. One-group diffusion model

For one energy group and six delayed neutron groups, the time dependent neutron diffusion equations are, in usual notation,

$$\nabla\cdot D(\vec{r},t)\nabla\phi(\vec{r},t) + \nu\Sigma_f(\vec{r},t)\phi(\vec{r},t) - \Sigma_a(\vec{r},t)\phi(\vec{r},t)$$

$$= v^{-1}\frac{\partial}{\partial t}\phi(\vec{r},t) \tag{3.21a}$$

$$\beta\nu\Sigma_f(\vec{r},t)\phi(\vec{r},t) - \lambda_i C_i(\vec{r},t) = \frac{\partial}{\partial t} C_i(\vec{r},t) \tag{3.21b}$$

$$i = 1,2,\ldots,6.$$

The nuclear parameters of the reactor experience fluctuation as

$$\begin{aligned} D(\vec{r},t) &= D_o(\vec{r}) + \delta D(\vec{r},t) \\ \Sigma_a(\vec{r},t) &= \Sigma_{ao}(\vec{r}) + \delta\Sigma_a(\vec{r},t) \\ \Sigma_f(\vec{r},t) &= \Sigma_{fo}(\vec{r}) + \delta\Sigma_f(\vec{r},t) \end{aligned} \tag{3.22}$$

where $D_o(\vec{r})$, $\Sigma_{ao}(\vec{r})$ and $\Sigma_{fo}(\vec{r})$ are the steady state nuclear parameters before the perturbation is introduced.

These parametric fluctuations give rise to fluctuation of flux and the concentration of the delayed neutron precursors as follows

$$\begin{aligned} \phi(\vec{r},t) &= \phi_o(\vec{r}) + \delta\phi(\vec{r},t) \\ C_i(\vec{r},t) &= C_{io}(\vec{r}) + \delta C_i(\vec{r},t) \end{aligned}$$

where $\phi_o(\vec{r})$ and $C_{io}(\vec{r})$ are the steady state flux and the steady state ith group delayed neutron precursor. These satisfy the following equations

$$\nabla\cdot D_o(\vec{r})\nabla\phi_o(\vec{r}) + \nu\Sigma_{fo}(\vec{r})\phi_o(\vec{r}) - \Sigma_{ao}(\vec{r})\phi_o(\vec{r}) = 0 \tag{3.24}$$

$$\beta\nu\Sigma_{fo}(\vec{r})\phi_o(\vec{r}) - \lambda_i C_{io}(\vec{r}) = 0 \tag{3.25}$$

$$i = 1,2,\ldots,6.$$

Substituting Equations (3.22) and (3.23) into Equation (3.21a) and (3.21b), subtracting steady state terms and neglecting second order terms yields

$$\begin{aligned}
&\nabla\cdot D_o(\vec{r})\nabla\delta\phi(\vec{r},t) - \Sigma_{ao}(\vec{r})\delta\phi(\vec{r},t) + \sum_{i=1}^{6}\lambda_i\delta C_i(\vec{r},t) \\
&\quad + (1-\beta)\nu\Sigma_{fo}(\vec{r})\delta\phi(\vec{r},t) - v^{-1}\frac{\partial}{\partial t}\delta\phi(\vec{r},t) \\
&\quad = -\nabla\cdot\delta D(\vec{r},t)\nabla\phi_o(\vec{r}) + \delta\Sigma_a(\vec{r},t)\phi_o(\vec{r}) \\
&\quad - (1-\beta)\nu\delta\Sigma_f(\vec{r},t)\phi_o(\vec{r})
\end{aligned} \tag{3.26}$$

$$\begin{aligned}
&\beta_i\nu\Sigma_{fo}(\vec{r})\delta\phi(\vec{r},t) - \lambda_i\delta C_i(\vec{r},t) - \frac{\partial}{\partial t}\delta C_i(\vec{r},t) \\
&\quad = -\beta_i\nu\delta\Sigma_f(\vec{r},t)\phi_o(\vec{r})
\end{aligned} \tag{3.27}$$

$$i = 1,2,\ldots,6.$$

Taking the Fourier Transform of Equation (3.27) and rearranging gives

$$\delta C_i(\vec{r},\omega) = [\beta_i\nu\Sigma_{fo}(\vec{r})\delta\phi(\vec{r},\omega) + \beta_1\nu\delta\Sigma_f(\vec{r},\omega)\phi_o(\vec{r})]/(\lambda_i+j\omega)$$

$$i = 1,2,\ldots,6. \tag{3.28}$$

Taking the Fourier Transform of Equation (3.26), substituting Equation (3.28), and rearranging yields

$$\nabla \cdot D_o(\vec{r})\nabla\delta(\vec{r},\omega) - [\Sigma_{ao}(\vec{r}) + \frac{j\omega}{v}]\delta\phi(\vec{r},\omega) + \nu\Sigma_{fo}(\vec{r})[1-\beta+\sum_{i=1}^{6}\frac{\lambda_i\beta_i}{\lambda_i+j\omega}]\delta\phi(\vec{r},\omega) = S(\vec{r},\omega) \tag{3.29}$$

where

$$S(\vec{r},\omega) = -\nabla\cdot\delta D(\vec{r},\omega)\nabla\phi_o(\vec{r}) + \delta\Sigma_a(\vec{r},\omega)\phi_o(\vec{r}) - \nu\delta\Sigma_f(\vec{r},\omega)[1-\beta+\sum_i\frac{\lambda_i\beta_i}{\lambda_i+j\omega}]\phi_o(\vec{r}) \tag{3.30}$$

= noise source.

Note here that the noise source given by Equation (3.30) is composed of the fluctuation of group constants multiplied by the steady state flux $\phi_o(\vec{r})$.

Equation (3.29) can be rewritten as

$$L\delta\phi(\vec{r},\omega) = S(\vec{r},\omega) \tag{3.31}$$

where

$$L = \nabla\cdot D_o(\vec{r})\nabla - \Sigma_{ao}(\vec{r}) - \frac{j\omega}{v} + \nu\Sigma_{go}(\vec{r})(1-\beta+\sum_{i=1}^{6}\frac{\lambda_i\beta_i}{\lambda_i+j\omega})$$

and $S(\vec{r},\omega)$, the noise source, is defined in Equation (3.30).

Now define the adjoint equation for the adjoint function $\psi(\vec{r},\omega)$ which is dependent on the detector cross section $\Sigma_d(\vec{r})$ (if it is assumed that the detector cross section is frequency independent)

$$L^+\psi(\vec{r},\omega) = \Sigma_d(\vec{r}) \tag{3.32}$$

where, according to Equation (3.20), the adjoint operator L^+ is

$$L^+ = (L^T)^*$$

$$= \nabla\cdot D_o(\vec{r}) - \Sigma_{ao}(\vec{r}) + \frac{j\omega}{v} + \nu\Sigma_{fo}(\vec{r})(1-\beta+\sum_{i=1}^{6}\frac{\lambda_i\beta_i}{\lambda_i-j\omega}). \qquad (3.33)$$

The adjoint flux in the frequency domain, i.e., $\psi(\vec{r},\omega)$, is in general

1. a complex quantity, and
2. frequency dependent and space dependent.

Now, let

$$\psi(\vec{r},\omega) = \psi_R(\vec{r},\omega) + j\chi(\vec{r},\omega) \qquad (3.34)$$

where $\psi_R(\vec{r},\omega)$ and $\chi(\vec{r},\omega)$ are the real part and the imaginary part of $\psi(\vec{r},\omega)$ respectively.

Substituting Equation (3.34) into Equation (3.32) and equating the real parts and imaginary parts of the equation yields

$$\nabla\cdot D_o\nabla\psi_R - \Sigma_{ao}\psi_R - \frac{\omega}{v}\chi + \nu\Sigma_{fo}(1-\sum_i\frac{\beta_i\omega^2}{\lambda_i^2+\omega^2})\psi_R$$

$$- \nu\Sigma_{fo}(\sum_i\frac{\lambda_i\beta_i\omega}{\lambda_i^2+\omega^2})\chi = \Sigma_d \qquad (3.35a)$$

$$\nabla\cdot D_o\nabla\chi - \Sigma_{ao}\chi + \frac{\omega}{v}\psi_R + \nu\Sigma_{fo}(\sum_i\frac{\lambda_i\beta_i\omega}{\lambda_i^2+\omega^2})\psi_R$$

$$+ \nu\Sigma_{fo}(1-\sum_i\frac{\beta_i\omega^2}{\lambda_i^2+\omega^2})\chi = 0. \qquad (3.35b)$$

Note that in Equations (3.35a) and (3.35b), ψ_R and χ are functions of $\vec{r}$ and ω, whereas the macroscopic constants are function of $\vec{r}$ only.

The solution for $\psi_R(\vec{r},\omega)$ and $\chi(\vec{r},\omega)$ for different ω's can be obtained by utilizing any static two-group diffusion code which can handle upscattering and an external source.

In Equation (3.31) both the operator L and the function $\delta\phi(\vec{r},\omega)$ are complex so that the definitions for the adjoint operator and inner product should follow those given by Equation (3.18) and Equation (3.19) respectively.

Applying the adjoint technique to Equation (3.31) and Equation (3.32) yields

$$<L\delta\phi(\vec{r},\omega),\ \psi(\vec{r},\omega)> = <S(\vec{r},\omega),\ \psi(\vec{r},\omega)> \tag{3.36}$$

$$<\delta\phi(\vec{r},\omega),\ L^{+}\psi(\vec{r},\omega)> = <\delta\phi(\vec{r},\omega),\ \Sigma_d(\vec{r})>. \tag{3.37}$$

From the definition of the adjoint operator, the left hand sides of Equation (3.26) and Equation (3.27) are equal. This leads to the results

$$<S(\vec{r},\omega),\ \psi(\vec{r},\omega)> = <\delta\phi(\vec{r},\omega),\ \Sigma_d(\vec{r})>$$

or

$$<\psi(\vec{r},\omega),\ S(\vec{r},\omega)> = <\Sigma_d(\vec{r}),\ \delta\phi(\vec{r},\omega)> \tag{3.38}$$

which is equivalent to the integral representation

$$\int_{\vec{r}} \psi^*(\vec{r},\omega)\ S(\vec{r},\omega)d\vec{r} = \int_{\vec{r}} \Sigma_d{}^*(\vec{r})\delta\phi(\vec{r},\omega)d\vec{r}$$

$$= \int_{\vec{r}} \Sigma_d(\vec{r})\delta\phi(\vec{r},\omega)d\vec{r}\ . \tag{3.39}$$

For a neutron detector with a cross section $\Sigma_d(\vec{r})$ located at $\vec{r}_d$ with volume $\Delta\vec{r}_d$, the response to a volume noise source located at $\vec{r}_s$ with volume $\Delta\vec{r}_s$, expressed in the frequency domain, can be defined, from Equation (3.39), as

$$\delta R(\vec{r}_s,\vec{r}_d,\omega) = \int_{\Delta\vec{r}_d} \Sigma_d(\vec{r})\,\delta\phi(\vec{r},\omega)\,d\vec{r} \tag{3.40a}$$

or

$$\delta R(\vec{r}_s,\vec{r}_d,\omega) = \int_{\Delta\vec{r}_s} \psi^*(\vec{r},\vec{r}_d,\omega)\,S(\vec{r},\omega)\,d\vec{r} \tag{3.40b}$$

where

$\psi(\vec{r},\vec{r}_d,\omega)$ = solution of the adjoint flux for detector at $\vec{r}_d$.

Equation (3.40b) is the most convenient formulation to use to obtain the detector response function in the frequency domain. This equation provides a generalized representation for the detector response in a one-group model without any constraints on either the noise source, $S(\vec{r},\omega)$, or on the adjoint flux, $\psi(\vec{r},\omega)$.

In order to investigate δR in more detail, substitute Equation (3.30) into Equation (3.40b). This leads to the following representation

$$\begin{aligned}\delta R(\vec{r}_s,\vec{r}_d,\omega) &= \int_{\Delta\vec{r}_s} \psi^*(\vec{r},\vec{r}_d,\omega)\,S(\vec{r},\omega)\,d\vec{r} \\ &= -\int_{\Delta\vec{r}_s} \nabla\cdot\delta D(\vec{r},\omega)\nabla\phi_o(\vec{r})\psi^*(\vec{r},\vec{r}_d,\omega)\,d\vec{r} \\ &\quad + \int_{\Delta\vec{r}_s} \delta\Sigma_a(\vec{r},\omega)\phi_o(\vec{r})\psi^*(\vec{r},\vec{r}_d,\omega)\,d\vec{r} \\ &\quad - \int_{\Delta\vec{r}_s} \nu\delta\Sigma_f(\vec{r},\omega)\,(1-\beta+\sum_i \frac{\lambda_i\beta_i}{\lambda_i+j\omega})\phi_o(\vec{r})\psi^*(\vec{r},\vec{r}_d,\omega)\,d\vec{r}\,.\end{aligned} \tag{3.41}$$

The first term on the right hand side of Equation (3.41) can be reduced to

$$\int_{\Delta\vec{r}_s} \delta D(\vec{r},\omega)\nabla\phi_o(\vec{r})\nabla\psi^*(\vec{r},\omega)d\vec{r}$$

by applying the Divergence Theorem and the boundary conditions for ψ which vanishes at the reactor surface.

Thus, the generalized one-group model representation of $\delta R(\vec{r}_s,\vec{r}_d,\omega)$ can be written as

$$\begin{aligned}\delta R(\vec{r}_s,\vec{r}_d,\omega) = &\int_{\Delta\vec{r}_s} \delta D(\vec{r},\omega)\nabla\phi_o(\vec{r})\nabla\psi^*(\vec{r},\vec{r}_d,\omega)d\vec{r} \\ &+ \int_{\Delta\vec{r}_s} \delta\Sigma_a(\vec{r},\omega)\phi_o(\vec{r})\psi^*(\vec{r},\vec{r}_d,\omega)d\vec{r} \\ &- \int_{\Delta\vec{r}_s} \nu\delta\Sigma_f(\vec{r},\omega)\left(1-\beta+\sum_i \frac{\lambda_i\beta_i}{\lambda_i+j\omega}\right)\phi_o(\vec{r})\psi^*(\vec{r},\vec{r}_d,\omega)d\vec{r}.\end{aligned} \tag{3.42}$$

Note here that $\phi_o(\vec{r})$ is the steady state flux given in Equation (3.24), and the adjoint flux is the solution from Equation (3.32) (or from the equivalent Equations (3.35a) and (3.35b).

The detector response function, δR, defined in Equations (3.40b) and (3.42) is different than the well-known steady state detector response given in Equation (3.17). The differences between these formulations are summarized as follows:

1. δR is the Fourier Transform of the fluctuation of the detector response due to the fluctuation of neutron flux (refer to Equation (3.40a)) resulting from the noise source

(the parametric fluctuation). The quantity defined by Equation (3.17) is the steady state detector readings due to the neutrons introduced at $\vec{r}_s$.

2. δR is defined in the frequency domain and is a complex quantity whereas Equation (3.17) is defined in the time domain and is a real quantity.

3. δR is weighted by the complex conjugate of the adjoint flux whereas Equation (3.17) is weighted by the adjoint flux itself.

2. Two-group diffusion model

For a time-dependent two-group diffusion model with six group of delayed neutrons, the applicable equations are

$$\nabla\cdot D_1(\vec{r},t)\nabla\phi_1(\vec{r},t) - \Sigma_1(\vec{r},t)\phi_1(\vec{r},t) + \nu\Sigma_f(\vec{r},t)\phi_2(\vec{r},t) = v_1^{-1}\frac{\partial}{\partial t}\phi_1(\vec{r},t)$$

$$\nabla\cdot D_2(\vec{r},t)\nabla\phi_2(\vec{r},t) - \Sigma_2(\vec{r},t)\phi_2(\vec{r},t) + \Sigma_{12}(\vec{r},t)\phi_1(\vec{r},t) = v_2^{-1}\frac{\partial}{\partial t}\phi_2(\vec{r},t)$$

$$\beta_i\nu\Sigma_f(\vec{r},t)\phi_2(\vec{r},t) - \lambda_i C_i(\vec{r},t) = \frac{\partial}{\partial t}C_i(\vec{r},t)$$

$$i = 1,2,\ldots,6 \qquad (3.43)$$

where the fast fission effect is neglected and all the fission neutrons are assumed to appear in the fast group.

The fluctuation of the reactor parameters are of the following form

$$D_1(\vec{r},t) = D_1(\vec{r}) + \delta D_1(\vec{r},t)$$

$$D_2(\vec{r},t) = D_2(\vec{r}) + \delta D_2(\vec{r},t)$$

$$\Sigma_1(\vec{r},t) = \Sigma_1(\vec{r}) + \delta\Sigma_1(\vec{r},t) \tag{3.44}$$

$$\Sigma_2(\vec{r},t) = \Sigma_2(\vec{r}) + \delta\Sigma_2(\vec{r},t)$$

$$\Sigma_{12}(\vec{r},t) = \Sigma_{12}(\vec{r}) + \delta\Sigma_{12}(\vec{r},t).$$

The parametric fluctuations give rise to fluctuations of flux and delayed neutron precursors

$$\phi_1(\vec{r},t) = \phi_1(\vec{r}) + \delta\phi_1(\vec{r},t)$$

$$\phi_2(\vec{r},t) = \phi_2(\vec{r}) + \delta\phi_2(\vec{r},t) \tag{3.45}$$

$$C_i(\vec{r},t) = C_i(\vec{r}) + \delta C_i(\vec{r},t).$$

Following the same procedures described in the one-group model, the resulting equations in the frequency domain are

$$\nabla\cdot D_1(\vec{r})\nabla\delta\phi_1(\vec{r},\omega) - [\Sigma_1(\vec{r}) + \frac{j\omega}{v_1}]\delta\phi_1(\vec{r},\omega)$$
$$+ \nu\Sigma_f(\vec{r})[1-\beta+\Sigma_i\frac{\lambda_i\beta_i}{\lambda_k+j\omega}]\delta\phi_2(\vec{r},\omega) = S_1(\vec{r},\omega)$$

$$\nabla\cdot D_2(\vec{r})\nabla\delta\phi_2(\vec{r},\omega) - [\Sigma_2(\vec{r}) + \frac{j\omega}{v_2}]\delta\phi_2(\vec{r},\omega) + \Sigma_{12}(\vec{r})\delta\phi_1(\vec{r},\omega)$$
$$= S_2(\vec{r},\omega) \tag{3.46}$$

where

$$S_1(\vec{r},\omega) = \text{Noise source for fast group}$$

$$= -\nabla\cdot\delta D_1(\vec{r},\omega)\nabla\phi_1(\vec{r})+\delta\Sigma_1(\vec{r},\,)\phi_1(\vec{r})$$

$$-\nu\delta\Sigma_f(\vec{r},\omega)\left[1-\beta+\sum_i \frac{\lambda_i\beta_i}{\lambda_i+j\omega}\right]\phi_2(\vec{r}) \qquad (3.47)$$

$$S_2(\vec{r},\omega) = \text{Noise source for thermal group}$$

$$= -\nabla\cdot\delta D_2(\vec{r},\omega)\nabla\phi_2(\vec{r})+\delta\Sigma_2(\vec{r},\omega)\phi_2(\vec{r})-\delta\Sigma_{12}(\vec{r},\omega)\phi_1(\vec{r}).$$

Note here that $\phi_1(\vec{r})$ and $\phi_2(\vec{r})$ are the steady state fast flux and thermal flux respectively. $\delta\phi_1(\vec{r},\omega)$ and $\delta\phi_2(\vec{r},\omega)$ are the fluctuations of the fast and thermal flux in the frequency domain. $\Sigma_1(\vec{r})$, $\Sigma_2(\vec{r})$, $\Sigma_{12}(\vec{r})$, $\nu\Sigma_f(\vec{r})$, $D_1(\vec{r})$, $D_2(\vec{r})$ are steady state group constants.

Equation (3.46) can be formulated in the matrix form as

$$L\delta\underline{\phi}(\vec{r},\omega) = \underline{S}(\vec{r},\omega) \qquad (3.48a)$$

where

$$L = \begin{bmatrix} \nabla\cdot D_1(\vec{r})\nabla-\Sigma_1(\vec{r})-\dfrac{j\omega}{v_1} & \nu\Sigma_f(\vec{r})\left(1-\beta+\sum_i \dfrac{\lambda_i\beta_i}{\lambda_i+j\omega}\right) \\ \Sigma_{12}(\vec{r}) & \nabla\cdot D_2(\vec{r})-\Sigma_2(\vec{r})-\dfrac{j\omega}{v_2} \end{bmatrix} \qquad (3.48b)$$

$$\delta\underline{\phi}(\vec{r},\omega) = [\delta\phi_1(\vec{r},\omega),\ \delta\phi_2(\vec{r},\omega)]^T \qquad (3.48c)$$

$$\underline{S}(\vec{r},\omega) = [S_1(\vec{r},\omega),\ S_2(\vec{r},\omega)]^T . \qquad (3.48d)$$

The corresponding adjoint equation for Equation (3.48), taking the detector cross section as the adjoint source, can be written as

$$L^{+}\underline{\psi}(\vec{r},\omega) = \underline{\Sigma}_{d}(\vec{r}) \tag{3.49a}$$

where

L^{+} = The adjoint operator of L

$$= (L^{T})^{*}$$

$$= \begin{bmatrix} \nabla\cdot D_1(\vec{r}) - \Sigma_1(\vec{r}) + \frac{j\omega}{v_1} & \Sigma_{12}(\vec{r}) \\ \nu\Sigma_f(\vec{r})\,(1-\beta+\sum_i \frac{\lambda_i\beta_i}{\lambda_i - j\omega}) & \nabla\cdot D_2(\vec{r})\nabla - \Sigma_2(\vec{r}) + \frac{j\omega}{v_2} \end{bmatrix} \tag{3.49b}$$

$$\underline{\psi}(\vec{r},\omega) = [\psi_1(\vec{r},\omega),\ \psi_2(\vec{r},\omega)]^{T} \tag{3.49c}$$

$$\underline{\Sigma}_{d}(\vec{r}) = [\Sigma_{d1}(\vec{r},\omega),\ \Sigma_{d2}(\vec{r})]^{T}. \tag{3.49d}$$

The equations for the real and imaginary parts of the adjoint flux can be obtained by letting

$$\begin{aligned} \psi_1(\vec{r},\omega) &= \psi_{1R}(\vec{r},\omega) + j\chi_1(\vec{r},\omega) \\ \psi_2(\vec{r},\omega) &= \psi_{2R}(\vec{r},\omega) + j\chi_2(\vec{r},\omega) \end{aligned} \tag{3.50}$$

and substituting Equation (3.50) into Equation (3.49)

$$\nabla\cdot D_1\nabla\psi_{1R} - \Sigma_1\psi_{1R} - \frac{\omega}{v_1}\chi_1 + \Sigma_{12}\psi_{2R} = \Sigma_{d1} \tag{3.51a}$$

$$\nabla\cdot D_1\nabla\psi_1 - \Sigma_1\chi_1 + \frac{\omega}{v_1}\psi_{1R} + \Sigma_{12}\chi_2 = 0 \tag{3.51b}$$

$$\begin{aligned} &\nabla\cdot D_2\nabla\psi_{2R} - \Sigma_2\psi_{2R} + \nu\Sigma_f(1-\sum_i \frac{\omega^2\beta_i^2}{\lambda_i^2+\omega^2})\psi_{1R} \\ &\quad - \nu\Sigma_f(\sum_i \frac{\omega\lambda_i\beta_i}{\lambda_i^2+\omega^2})\chi_1 - \frac{\omega}{v_2} = \psi_{d2} \end{aligned} \tag{3.51c}$$

$$\nabla\cdot D_2\nabla\chi_2-\Sigma_2\chi_2+\frac{\omega}{v_2}\psi_{2R}+\nu\Sigma_f\left(\sum_i\frac{\lambda_i\beta_i\omega}{\lambda_i^2+\omega^2}\right)\psi_{1R}$$

$$+\nu\Sigma_f\left(1-\sum_i\frac{\omega^2\beta_i}{\lambda_i^2+\omega^2}\right)\chi_1=0 \qquad (3.51d)$$

where in the above equations, for the sake of simplicity, all arguments are omitted.

For any fixed frequency, Equations (3.51a) through (3.51d) can be solved by any static four-group diffusion code, which can handle the upscattering effect and external source, with certain modifications. Usually it is tedious to solve these equations analytically.

Applying the inner product to Equation (3.48) and Equation (3.49) yields

$$\langle\underline{\psi}(\vec{r},\omega),\ \underline{S}(\vec{r},\omega)\rangle = \langle\underline{\Sigma}_d(\vec{r}),\ \delta\underline{\phi}(\vec{r},\omega)\rangle. \qquad (3.52)$$

Thus, the response of a detector at $\vec{r}_d$ with volume $\vec{r}_d$ to a finite volume noise source at $\vec{r}_s$, expressed in the frequency domain, can be written as

$$\delta R(\vec{r}_s,\vec{r}_d,\omega) = \int_{\Delta\vec{r}_d}\underline{\Sigma}_d^T(\vec{r})\,\delta\underline{\phi}(\vec{r},\omega)\,d\vec{r}$$

$$= \int_{\Delta\vec{r}_d}[\Sigma_{d1}(\vec{r}),\ \Sigma_{d2}(\vec{r})]\begin{bmatrix}\delta\phi_1(\vec{r},\omega)\\ \delta\phi_2(\vec{r},\omega)\end{bmatrix}d\vec{r}$$

$$= \int_{\Delta\vec{r}_d}[\Sigma_{d1}(\vec{r})\delta\phi_1(\vec{r},\omega)+\Sigma_{d2}(\vec{r})\delta\phi_2(\vec{r},\omega)]\,d\vec{r}. \qquad (3.53)$$

It is clear from Equation (3.53) that δR is the fluctuation of the response of a given detector in the frequency domain due to the fluctuation of the flux induced by the parametric fluctuations inside the reactor (i.e. the fluctuations of macroscopic group constants).

The more convenient form for calculating δR is the adjoint space formulation

$$\delta R(\vec{r}_s,\vec{r}_d,\omega) = \int [\underline{\psi}^*(\vec{r},\omega)]^T \underline{S}(\vec{r},\omega)d\vec{r}$$

$$= \int_{\Delta\vec{r}_s} [\psi_1^*(\vec{r},\vec{r}_d,\omega)S_1(\vec{r},\omega)+\psi_2^*(\vec{r},\vec{r}_d,\omega)S_2(\vec{r},\omega)]d\vec{r} \tag{3.54}$$

where $\psi_1(\vec{r},\vec{r}_d,\omega)$ and $\psi_2(\vec{r},\vec{r}_d,\omega)$ are the solutions of the fast and thermal adjoint flux due to the detector at $\vec{r}_d$ respectively.

Substituting Equation (3.47), the expressions for the noise source, into Equation (3.54) yields

$$\delta R(\vec{r}_s,\vec{r}_d,\omega) = \int_{\Delta\vec{r}_s} \delta D_1(\vec{r},\omega)\nabla\phi_1(\vec{r})\nabla\psi_1^*(\vec{r},\vec{r}_d,\omega)d\vec{r}$$

$$+ \int_{\Delta\vec{r}_s} \delta D_2(\vec{r},\omega)\nabla\phi_2(\vec{r})\nabla\psi_2^*(\vec{r},\vec{r}_d,\omega)d\vec{r} + \int_{\Delta\vec{r}_s} \delta\Sigma_1(\vec{r},\omega)\phi_1(\vec{r})\psi_1^*(\vec{r},\vec{r}_d,\omega)d\vec{r}$$

$$+ \int_{\Delta\vec{r}_s} \delta\Sigma_2(\vec{r},\omega)\phi_2(\vec{r})\psi_2^*(\vec{r},\vec{r}_d,\omega)d\vec{r} - \int_{\Delta\vec{r}_s} \delta\Sigma_{12}(\vec{r},\omega)\phi_1(\vec{r})\psi_2^*(\vec{r},\vec{r}_d,\omega)d\vec{r}$$

$$- \int_{\Delta\vec{r}_s} \nu\delta\Sigma_f(\vec{r},\omega)\,(1-\beta+\sum_i \frac{\lambda_i\beta_i}{\lambda_i+j\omega})\phi_2(\vec{r})\psi_1^*(\vec{r},\vec{r}_d,\omega)d\vec{r}. \tag{3.55}$$

It should be noted again here that $\phi_1(\vec{r})$ and $\phi_2(\vec{r})$ are the steady state fast and thermal fluxes respectively and are the solutions of the following equation

$$\begin{bmatrix} \nabla\cdot D_1(\vec{r})\nabla-\Sigma_1(\vec{r}) & \nu\Sigma_f(\vec{r}) \\ \Sigma_{12}(\vec{r}) & \nabla\cdot D_2(\vec{r})\nabla-\Sigma_{12}(\vec{r}) \end{bmatrix} \begin{bmatrix} \phi_1(\vec{r}) \\ \phi_2(\vec{r}) \end{bmatrix} = \begin{bmatrix} 0 \\ 0 \end{bmatrix}. \qquad (3.56)$$

3. The multigroup diffusion model

The detector response model can be extended to the multigroup case very easily by letting (for simplicity, all arguments in $\underline{\psi}$ and $\underline{S}$ are omitted)

$$\underline{\psi} = \underline{\psi}_R + j\chi$$

$$\underline{S} = \underline{S}_R + j\underline{S}_I$$

where $\underline{S}_R$ and $\underline{S}_I$ are the real part and the imaginary part of $\underline{S}$ (the noise source) respectively.

The detector response function in a multigroup formulation is then given by

$$\delta R = \langle \underline{\psi}, \underline{S} \rangle$$

$$= \int_{\vec{r}} [\underline{\psi}^*]^T \underline{S} \, d\vec{r}$$

$$= \int_{\vec{r}} [\underline{\psi}_R - j\underline{\chi}]^T [\underline{S}_R + j\underline{S}_I] d\vec{r}$$

$$= \int_{\vec{r}} [\psi_{1R} - j\chi_1, \psi_{2R} - j\chi_2, \ldots, \psi_{GR} - j\chi_G] \begin{bmatrix} S_{1R}+jS_{1I} \\ S_{2r}+jS_{2I} \\ \vdots \\ S_{GR}+jS_{GI} \end{bmatrix} d\vec{r}$$

$$= \int_{\vec{r}} \sum_{i=1}^{G} (\psi_{iR} S_{iR} + \chi_i S_{iI}) d\vec{r} + j \int_{\vec{r}} \sum_{i=1}^{G} (\psi_{iR} S_{iI} - \chi_i S_{iR}) d\vec{r}$$

$$= \delta R_R + j \delta R_I$$

$$= |\delta R| e^{j\theta} \tag{3.57}$$

where

$$\delta R_R = \int_{\vec{r}} \sum_{i=1}^{G} (\psi_{iR} S_{iR} + \chi_i S_{iI}) d\vec{r} \tag{3.58a}$$

= the real part of δR

$$\delta R_I = \int_{\vec{r}} \sum_{i=1}^{G} (\psi_{iR} S_{iI} - \chi_i S_{iR}) d\vec{r} \tag{3.58b}$$

= the imaginary part of δR

$$|\delta R| = [(\delta R_R)^2 + (\delta R_I)^2]^{1/2} \tag{3.58c}$$

= the amplitude of δR

$$\theta = \tan^{-1}\left(\frac{\delta R_I}{\delta R_R}\right) \tag{3.58d}$$

= the phase of δR

S_{iR} = real part of the ith group noise source

S_{iI} = imaginary part of the ith group noise source

ψ_{iR} = real part of the ith group adjoint flux

ψ_{iI} = imaginary part of the ith group adjoint flux.

It can be seen from Equation (3.57) that δR has both a spatial and frequency dependence and, in general, is a complex quantity.

C. The Evaluation of the Detector Response Model

From the analysis presented in previous sections, it has been shown that a G-energy group model requires the solution of 2G simultaneous equation to obtain the adjoint function in the frequency domain, i.e. $\underline{\psi}(\vec{r},\omega)$. This requires a significant amount of computer time even if only a two-group model is to be used since each frequency requires a separate calculation and the problem is of the source-type which typically results in slow convergence. However, some assumptions can be applied to the model such that the calculational effort will be reduced without losing too much accuracy in the physical description.

The frequency range of interest for many reactor applications extends from 0.1 Hz up to about 10 Hz [11, 38, 40], which roughly coincides with the plateau region of the zero-power reactor transfer

function, given by

$$\lambda << \omega << \beta/\ell \tag{3.59}$$

Here β is the total delayed neutron fraction, ℓ is the neutron lifetime and λ is the decay constant for the delayed neutron precursors and is defined as

$$\lambda = \frac{1}{\beta} \sum_{i=1}^{6} \lambda_i \beta_i \ . \tag{3.60a}$$

For $\lambda << \omega << \beta/\ell$, the coefficients of $\psi_R(\vec{r},\omega)$ and $\chi(\vec{r},\omega)$ in Equations (3.35a) and (3.35b) reduce to

$$1 - \sum_i \frac{\beta_i \omega^2}{\lambda_i^2+\omega^2} \simeq 1 - \sum_i \beta_i = 1-\beta \tag{3.60b}$$

$$\frac{\omega}{v} + \nu\Sigma_{fo}(\vec{r}) \sum_i \frac{\lambda_i \beta_i \omega}{\lambda_i^2+\omega^2} \simeq \frac{\omega}{v} + \nu\Sigma_{fo}(\vec{r}) \frac{\sum_i \lambda_i \beta_i}{\omega} \ . \tag{3.60c}$$

Note that the coefficient given in Equation (3.60c) is negligible compared to other coefficients in Equations (3.35a) and (3.35b).

Thus, Equation (3.35a) and Equation (3.35b) can be rewritten as

$$\nabla \cdot D_o(\vec{r}) \Delta\psi_R(\vec{r},\omega) - \Sigma_{ao}(\vec{r})\psi_R(\vec{r},\omega) + \nu\Sigma_{fo}(\vec{r})(1-\beta)\psi_R(\vec{r},\omega) = \Sigma_d(\vec{r}) \tag{3.61a}$$

$$\nabla \cdot D_o(\vec{r}) \Delta\chi(\vec{r},\omega) - \Sigma_{ao}(\vec{r})\chi(\vec{r},\omega) + \nu\Sigma_{fo}(\vec{r})(1-\beta)\chi(\vec{r},\omega) = 0 . \tag{3.61b}$$

The form of Equations (3.61a) and (3.61b) suggests the following:

1. $\psi_R(\vec{r},\omega)$ and $\chi(\vec{r},\omega)$ are no longer frequency dependent for $\lambda << \omega << \beta/\ell$.

2. $\psi_R(\vec{r})$ can be solved by applying any static one-group diffusion code with an external source, $\Sigma_d(\vec{r})$.

3. $\chi(\vec{r})$ can be solved by the same static one-group diffusion code for the homogeneous case, i.e. without an external source.

4. Equation (3.61a) and Equation (3.61b) are no longer coupled.

Similarly, the two-group model solutions given in Equations (3.51a) through (3.51d) can be obtained, in the frequency range $\lambda << \omega << \beta/\ell$, from the following equations

$$\nabla\cdot D_1(\vec{r})\Delta\psi_{1R}(\vec{r})-\Sigma_1(\vec{r})\psi_{1R}(\vec{r}) + \Sigma_{12}(\vec{r})\psi_{2R}(\vec{r}) = \Sigma_{d1}(\vec{r}) \tag{3.62a}$$

$$\nabla\cdot D_2(\vec{r})\Delta\psi_{2R}(\vec{r})-\Sigma_2(\vec{r})\psi_{2R}(\vec{r}) + (1-\beta)\nu\Sigma_f(\vec{r})\psi_{1R}(\vec{r}) = \Sigma_{d2}(\vec{r}) \tag{3.62b}$$

$$\nabla\cdot D_1(\vec{r})\chi_1(\vec{r})-\Sigma_1(\vec{r})\chi_1(\vec{r}) + \Sigma_{12}(\vec{r})\chi_2(\vec{r}) = 0 \tag{3.62c}$$

$$\nabla\cdot D_2(\vec{r})\chi_2(\vec{r})-\Sigma_2(\vec{r})\chi_2(\vec{r}) + (1-\beta)\nu\Sigma_f(\vec{r})\chi_1(\vec{r}) = 0. \tag{3.62d}$$

Thus, in the frequency range $\lambda << \omega << \beta/\ell$, the real part of the adjoint functions, $\psi_{1R}(\vec{r})$ and $\psi_{2R}(\vec{r})$, can be solved from Equations (3.62a) and (3.62b) whereas the imaginary part of the adjoint functions, $\chi_1(\vec{r})$ and $\chi_2(\vec{r})$, can be obtained from Equations (3.62c) and (3.62d).

Since the real part of the adjoint functions are not coupled with the imaginary part of the adjoint functions, the above equations can be rewritten in two separate matrix equations as follows

$$\begin{bmatrix} \nabla\cdot D_1(\vec{r})\nabla-\Sigma_1(\vec{r}) & \Sigma_{12}(\vec{r}) \\ (1-\beta)\nu\Sigma_f(\vec{r}) & \nabla\cdot D_2(\vec{r})\nabla-\Sigma_2(\vec{r}) \end{bmatrix} \begin{bmatrix} \psi_{1R}(\vec{r}) \\ \psi_{2R}(\vec{r}) \end{bmatrix} = \begin{bmatrix} \Sigma_d(\vec{r}) \\ \Sigma_{d2}(\vec{r}) \end{bmatrix} \tag{3.63}$$

and

$$\begin{bmatrix} \nabla\cdot D_1(\vec{r})\nabla-\Sigma_1(\vec{r}) & \Sigma_{12}(\vec{r}) \\ (1-\beta)\nu\Sigma_f(\vec{r}) & \nabla\cdot D_2(\vec{r})\nabla-\Sigma_2(\vec{r}) \end{bmatrix} \begin{bmatrix} \chi_1(\vec{r}) \\ \chi_2(\vec{r}) \end{bmatrix} = \begin{bmatrix} 0 \\ 0 \end{bmatrix}. \tag{3.64}$$

It is observed that the operators in Equation (3.63) and Equation (3.64) are the same. This operator resembles the transpose of the two-group diffusion operator except for the $\nu\Sigma_f(\vec{r})$ term multiplied by $(1-\beta)$. Thus, $\psi_{1R}(\vec{r})$ and $\psi_{2R}(\vec{r})$ can be solved by a two-group diffusion code, which can handle an external source, with certain modifications. The imaginary parts, $\chi_1(\vec{r})$ and $\chi_2(\vec{r})$, then can be obtained by utilizing the same code but for the homogeneous case, i.e. no external source.

The shortcoming of this approach, although it reduces the four group calculation to two two-group calculations, are

1. only the shapes of $\chi_1(\vec{r})$ and $\chi_2(\vec{r})$ can be calculated, and
2. the relative amplitude of χ's to ψ_R's are not available because Equation (3.63) and Equation (3.64) are uncoupled.

However, in the frequency range of interest the imaginary part of the adjoint functions is negligible compared to the real party. This has been proposed by Dam [11], and proved by Pazsit [54] using a one-dimensional, two-group calculations for water

moderated reactors. This conclusion was also verified by private communication with Mansur Al-Ammar[1], who found, using a one-dimensional, two-group diffusion analysis for the Iowa State University UTR-10 reactor, that the real part of the adjoint function is about ten times larger than the imaginary part.

Thus, in the frequency range of interest, i.e. $\lambda << \omega << \beta/\ell$, Equation (3.55) can be reduced to

$$\begin{aligned}
\delta R(\vec{r}_s,\vec{r}_d,\omega) = & \int_{\Delta\vec{r}_s} \delta D_1(\vec{r},\omega)\nabla\phi_1(\vec{r})\nabla\psi_{1R}(\vec{r},\vec{r}_d)d\vec{r} \\
& + \int_{\Delta\vec{r}_s} \delta D_2(\vec{r},\omega)\nabla\phi_2(\vec{r})\nabla\psi_{2R}(\vec{r},\vec{r}_d)d\vec{r} \\
& + \int_{\Delta\vec{r}_s} \delta\Sigma_1(\vec{r},\omega)\phi_1(\vec{r})\psi_{1R}(\vec{r},\vec{r}_d)d\vec{r} \\
& + \int_{\Delta\vec{r}_s} \delta\Sigma_2(\vec{r},\omega)\phi_2(\vec{r})\psi_{2R}(\vec{r},\vec{r}_d)d\vec{r} \\
& - \int_{\Delta\vec{r}_s} \delta\Sigma_{12}(\vec{r},\omega)\phi_1(\vec{r})\psi_{1R}(\vec{r},\vec{r}_d)d\vec{r} \\
& - \int_{\Delta\vec{r}_s} \nu\delta\Sigma_f(\vec{r},\omega)\left(1-\beta+\Sigma_i\frac{\lambda_i\beta_i}{\lambda_i+j\omega}\right)\phi_2(\vec{r})\psi_{1R}(\vec{r},\vec{r}_d)d\vec{r} \qquad (3.65)
\end{aligned}$$

---

[1] M. Al-Ammar, Ph.D. candidate of the Department of Nuclear Engineering, Iowa State University. Proposed topic of dissertation lies in the area of the investigation of vibrating absorbers using reactor noise theory.

where $\psi_{1R}(\vec{r})$ and $\psi_{2R}(\vec{r})$ are solutions of the matrix Equation (3.63). $\phi_1(\vec{r})$ and $\phi_2(\vec{r})$ are the steady state fast and thermal fluxes and are given by the matrix Equation (3.56).

D. The Evaluation of the APSD of the Detector Response Function

As mentioned earlier in this chapter, the detector response function, $\delta R(\vec{r},\omega)$, represents the Fourier Transform of the fluctuation of the neutron detector current due to an input noise source $F(\vec{r},\omega)$. This relationship can be represented by the block diagram shown in Figure 3.1.

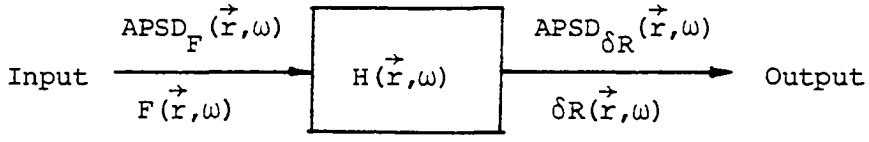

Figure 3.1. Block diagram for detector response to noise source

For the system given in Figure 3.1, the following relationship, according to Bendat [5] and Uhrig [73], holds:

$$\delta R(\vec{r},\omega) = H(\vec{r},\omega)F(\vec{r},\omega) \tag{3.66}$$

$$APSD_{\delta R}(\vec{r},\omega) = |H(\vec{r},\omega)|^2 APSD_F(\vec{r},\omega) \tag{3.67}$$

where

$F(\vec{r},\omega)$ = Fourier Transform of the input noise source

$APSD_F(\vec{r},\omega)$ = APSD of the input noise source

$APSD_{\delta R}(\vec{r},\omega)$ = APSD of the detector response function.

Taking the complex conjugate of Equation (3.66) and multiplying the results by Equation (3.66) yields

$$\delta R(\vec{r},\omega)\delta R^*(\vec{r},\omega) = H(\vec{r},\omega)H^*(\vec{r},\omega)F(\vec{r},\omega)F^*(\vec{r},\omega) .$$

This leads to

$$|H(\vec{r},\omega)|^2 = |\delta R(\vec{r},\omega)|^2/|F(\vec{r},\omega)|^2. \tag{3.68}$$

Comparing Equation (3.68) and Equation (3.67) gives

$$|H(\vec{r},\omega)|^2 = \frac{|\delta R(\vec{r},\omega)|^2}{|F(\vec{r},\omega)|^2} = \frac{APSD_{\delta R}(\vec{r},\omega)}{APSD_F(\vec{r},\omega)} . \tag{3.69}$$

The APSD of the detector response then can be written, according to Equation (3.69), as

$$APSD_{\delta R}(\vec{r},\omega) = \frac{APSD_F(\vec{r},\omega)}{|F(\vec{r},\omega)|^2} |\delta R(\vec{r},\omega)|^2. \tag{3.70}$$

In this research a fixed-location noise source (not a moving noise source) is investigated and the shape of $APSD_{\delta R}$'s as a function of the separation between the detector and the noise source is of main interest. Thus, $F(\vec{r},\omega)$ and $APSD_F(\vec{r},\omega)$ will be unchanged in the entire investigation. The normalized $APSD_{\delta R}$ with respect to a reference detector location $\vec{r}_f$ can be written, according to Equation (3.70), as

$$NAPSD_{\delta R}(\vec{r},\omega) = \frac{APSD_{\delta R}(\vec{r},\omega)}{APSD_{\delta R}(\vec{r}_f,\omega)} = \left|\frac{\delta R(\vec{r},\omega)}{\delta R(\vec{r}_f,\omega)}\right|^2$$

$$= |N\delta R(\vec{r},\omega)|^2 \tag{3.71}$$

where

$$N\delta R(\vec{r},\omega) = \frac{\delta R(\vec{r},\omega)}{\delta R(\vec{r}_f,\omega)} \tag{3.72}$$

= normalized detector response function.

IV. THE WHIRLAWAY-H CODE

As pointed out in Chapter III, the purpose of this research is to evaluate the detector response function, $\delta R(\vec{r}_s, \vec{r}_d, \omega)$, by a two-group, three-dimensional calculation and verify the proposed detector response model by experimental observations performed on the Iowa State University UTR-10 reactor. It was found to be difficult to find an existing three-dimensional diffusion code which would fit the formulation for the detector model evaluation without significant modifications. WHIRLAWAY [15], a FORTRAN II programmed, two-group, three-dimensional neutron diffusion code in rectangular geometry was chosen because the program solves equations which are similar to those used for the detector response model calculation.

In this chapter, the WHIRLAWAY code and modifications that were made for the WHIRLAWAY-H version are described. Procedures for the preparation of input data and the output format are discussed. A three-dimensional model for the UTR-10 reactor is developed. Then, using the WHIRLAWAY-H code and the three-dimensional UTR-10 model, the calculation of steady state flux and the adjoint flux distributions is described.

Nine CHAIN links were used in WHIRLAWAY so that the whole program (which needs about 380K bits storage) can be executed in a segmental fashion and linked by the CHAIN structure on a computer with small storage like an IBM 7090. The steady state two-group, three-dimensional neutron diffusion equation and the corresponding adjoint

equation solved in the WHIRLAWAY code are

$$L\underline{\phi}(\vec{r}) = 0 \tag{4.1}$$

$$L^{+}\underline{\psi}(\vec{r}) = 0 \tag{4.2}$$

where L is the two-group diffusion operator, L^{+} is the adjoint operator and is equal to the transpose of L.

The revised version, the WHIRLAWAY-H code, has basically the same structures as WHIRLAWAY with the following modifications:

1. The CHAIN links in WHIRLAWAY were removed and, in addition, a main program was added which will perform the linkage between the nine CHAIN links. Each CHAIN link was rewritten in subroutine form.
2. The FORTRAN II language was rewritten in the corresponding FORTRAN IV language.
3. The main additions provided in the WHIRLAWAY code include:
   a. an option for flux calculation with or without an external source in one region;
   b. an option for adjoint flux calculations with or without an external adjoint source in one region;
   c. an option for selecting any initial flux and/or initial adjoint flux guesses through a tape unit other than the zero initial flux distribution built in the original WHIRLAWAY code, and
   d. an option to plot the flux and/or adjoint flux distributions along any line in either the X, Y, or Z directions.

The revised WHIRLAWAY-H code allows two energy groups, 99 regions and 12,750 mesh points. Arbitrary distributions of materials and mesh spacing are permitted. The code will, if desired, compute the

associated flux-adjoint flux regional integrals that are useful for the detector response function evaluation.

A. The Program Structure

WHIRLAWAY-H consists of a main program and 15 subroutines. The name and functions of the subroutines together with the main program are listed in Table 4.1. A simplified flow diagram of WHIRLAWAY-H is shown in Figure 4.1. The input data preparation, sample input and the output are described in Appendix A.

B. The Computational Method

The method used in WHIRLAWAY (WHIRLAWAY-H basically follows the same iterative process) is called 'EQUIPOISE' which is a method proposed by Fowler and Tobias [15]. The basic conjecture of the 'EQUIPOSE' method is that there is no need to perform separate inner and outer iterations, as used by most of the diffusion codes, and these two processes can be successfully merged. Besides being a much simpler iterative process than the inner-outer iterative method, it was found, by Tobias from his experience with diffusion codes EQUIPOSE, TWENTY GRAND and WHIRLAWAY, that this method was rapid and reliable in solving few-group, Lambda-mode neutron diffusion equations in two and three dimensions [72].

Table 4.1. The functions of the main program and subroutines of the WHIRLAWAY-H code

Name	Functions
A. Main Program	Linking all subroutines
B. Subroutines	
1. INPT	Reads input data, selecting the desired initial flux distribution through one type unit
2. FLUX	Does flux and/or adjoint flux calculation. Also does the convergence test and eigenvalue calculations
3. OUT 1	Calculates the regional absorptions and volumes
4. KON 1 5. KON 2	Provides the coefficients of difference equations used in Subroutines FLUX and OUT 1
6. OUT 2	Prints the flux and/or adjoint flux distribution, the source distribution, the regional integral group absorptions and the region volume, or the regional integrals of adjoint flux times flux as required
7. SOUR	Calculates the fission source at each octant of each internal mesh point
8. KON 3	Calculates the octant volume needed for subroutine SOUR
9. ADJ 1	Calculates the flux time adjoint flux regional integrals for each group
10. ADJ 2	"
11. ADJ 3	"
12. ADJ 4	"
13. KON 4 14. KON 5	Supplementary to subroutines ADJ 1, ADJ 2, ADJ 3 and ADJ 4 for evaluating the regional volumes and surfaces
15. KON 6	"

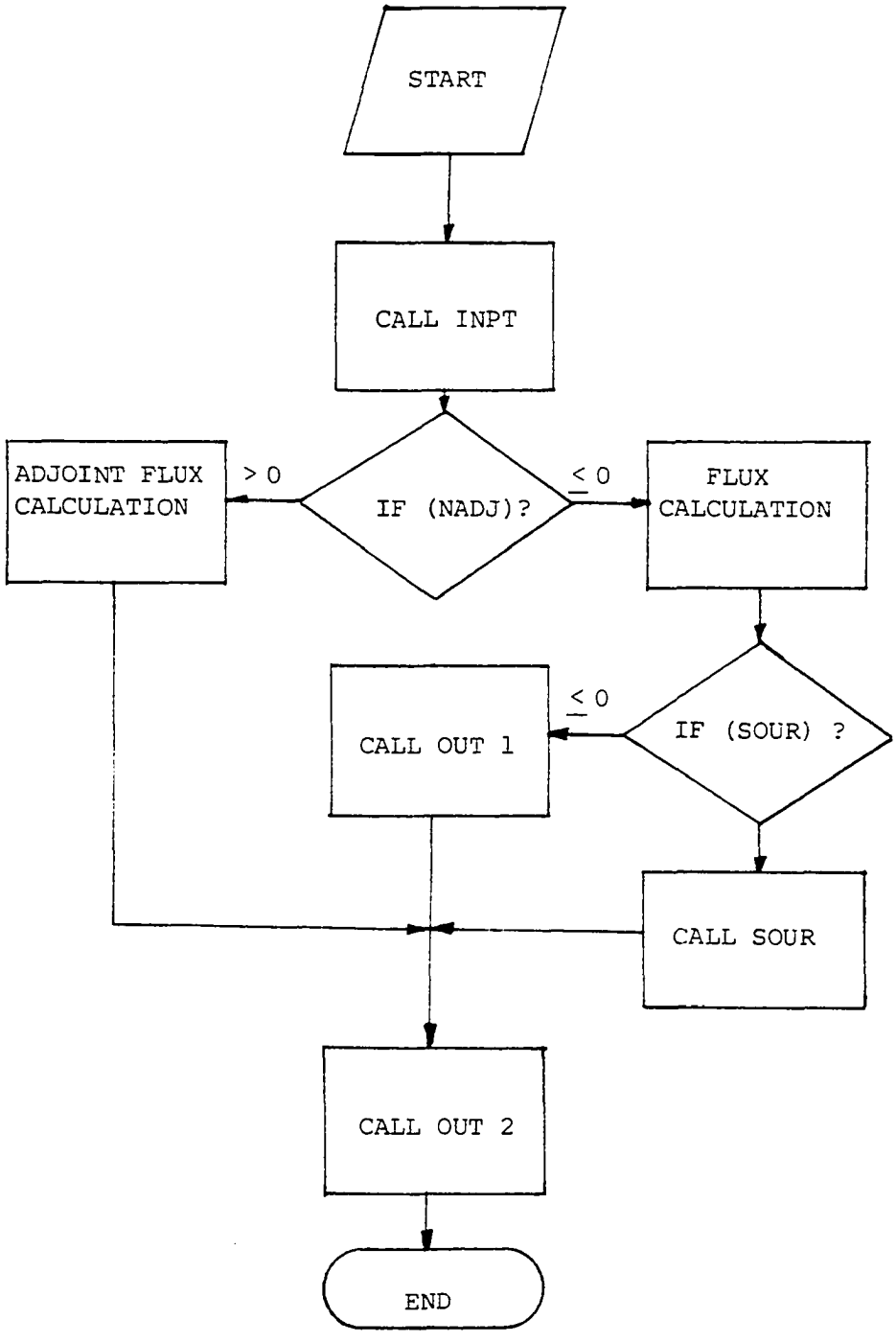

Figure 4.1. The flow diagram of the WHIRLAWAY-H code

C. The Three-dimensional Modeling of the UTR-10 Reactor

Nuclear parameters, necessary inputs to WHIRLAWAY-H, were calculated by using LEOPARD [2], a zero-dimensional cross section code. To obtain accurate macroscopic nuclear parameters from LEOPARD requires an accurate model for the UTR-10 reactor. Specific details of the UTR-10 are given in the reactor manuals [52] and by Nowark [50]. A brief description of the UTR-10 reactor core region will be given in Section A of Chapter VI. Several researchers at Iowa State University [7, 48] have used a one-dimensional model which includes five regions; two external graphite reflectors, one internal graphite reflector region and two fuel regions. The flux distributions across the reactor using the one-dimensional model agree fairly well with those provided by the American Standard Company [50].

In order to evaluate the detector response function for the two-group, three-dimensional formulation given by Equation (3.65), a three-dimensional model of the UTR-10 reactor was developed. The three-dimensional model used for the UTR-10 reactor core region follows the exact reactor as close as possible. It includes the fuel region in the core tank, the graphite reflector regions, and the experimental additions to the reactor including the water bubbler region and the detector region. Quarter symmetry was used in the model so as to reduce the computational effort. Control rods, air gaps and some structure materials are not included so as to reduce the

complexity of the model without loss of accuracy. The fuel region is treated as a homogenized mixture of a UAl_4 fuel metallic matrix, water and aluminum. The detailed modeling of the UTR-10 reactor and the calculated two-group, macroscopic parameters from LEOPARD for different regions in the UTR-10 are given in Appendix B. A sample input to the LEOPARD code is given in Appendix C.

Figure 4.2 shows a schematic cross-sectional diagram for the UTR-10 reactor in quarter symmetry.

To check the operation of WHIRLAWAY-H and to provide data for the detector model, the three-dimensional reactor model and the calculated macroscopic parameters from LEOPARD were used to calculate the steady state fluxes and the adjoint fluxes for the UTR-10 reactor core. In the WHIRLAWAY-H calculation, a total number of 7200 mesh points (20 mesh points in X direction, 12 in Y direction and 30 in Z direction) were used, and the normal reactor configuration was used which did not include the bubbler region or the detector region.

The calculated steady state flux and the adjoint flux distributions, using WHIRLAWAY-H, for different axes across the UTR-10 reactor are shown in Figures 4.3 through 4.18. It is found from Figure 4.5 that the shapes of the fast flux and the thermal flux are very similar to that obtained by Nowark [50] and Munson [48] using a two-group, one-dimensional diffusion model.

From an examination of the adjoint flux distributions shown in these figures, some interesting results are found:

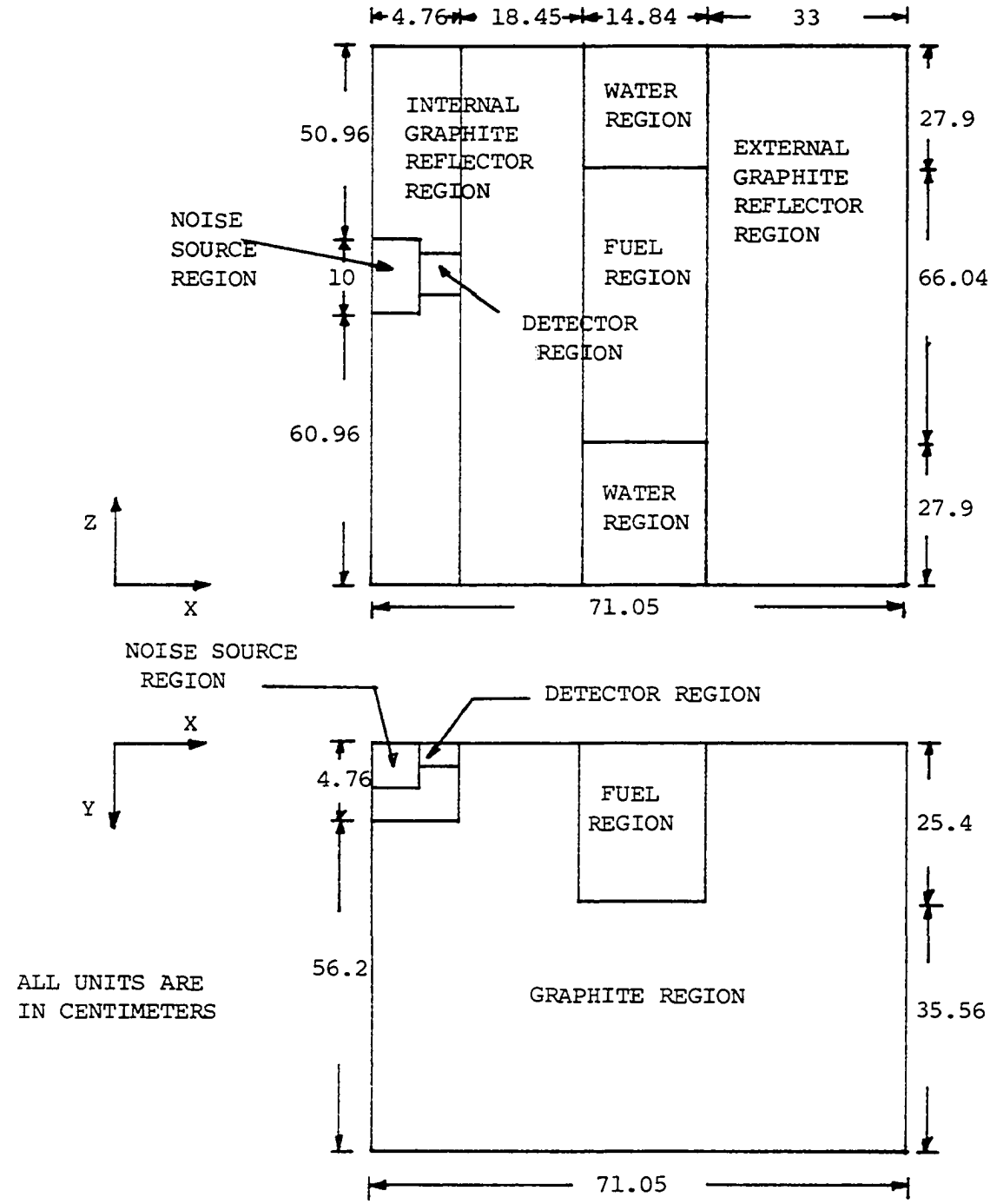

Figure 4.2. Schematic cross-sectional diagram for the UTR-10 reactor (all units are in centimeters)

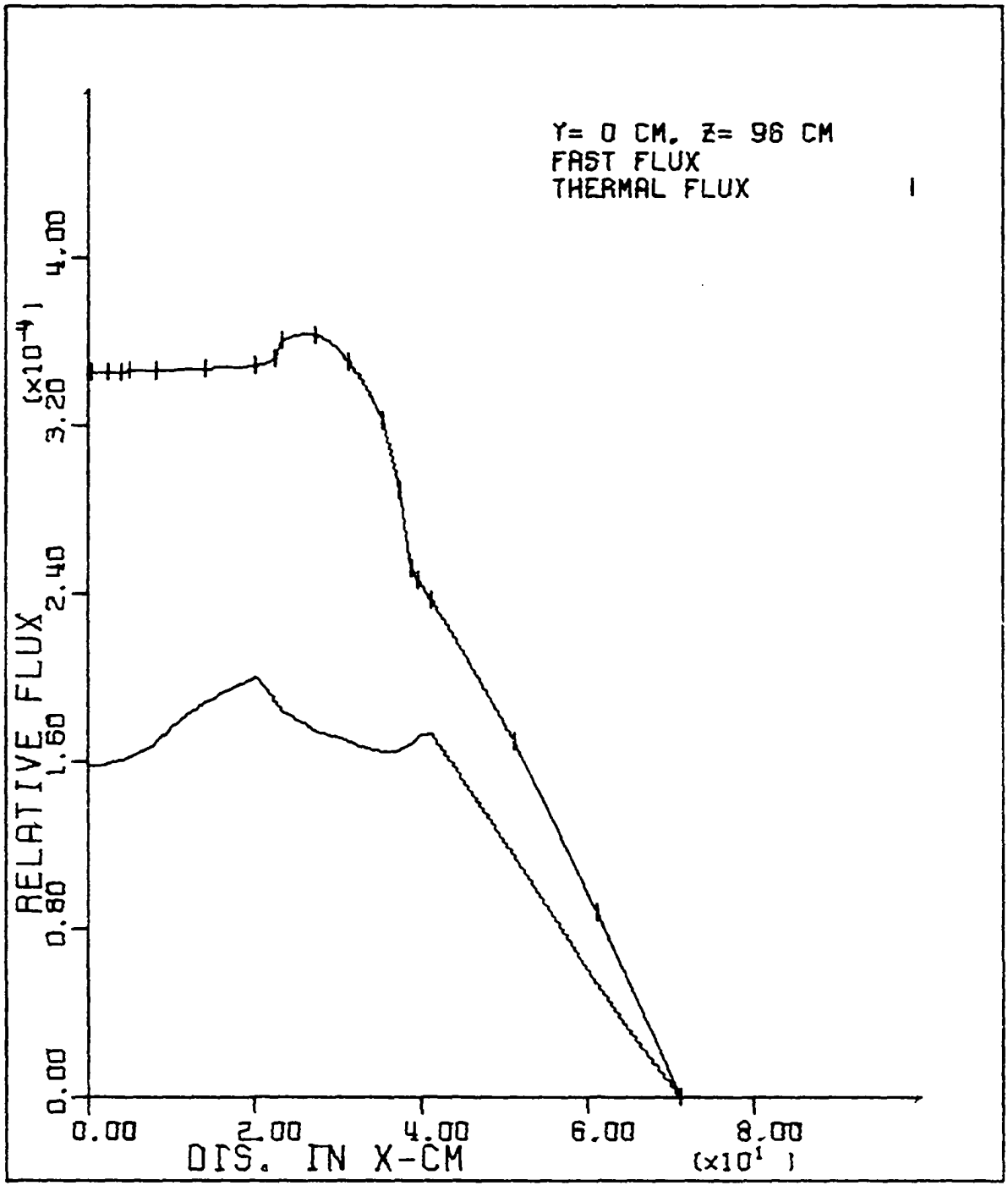

Figure 4.3. Fast and thermal flux distribution along the X-axis crossing the water region in the core tank of the UTR-10

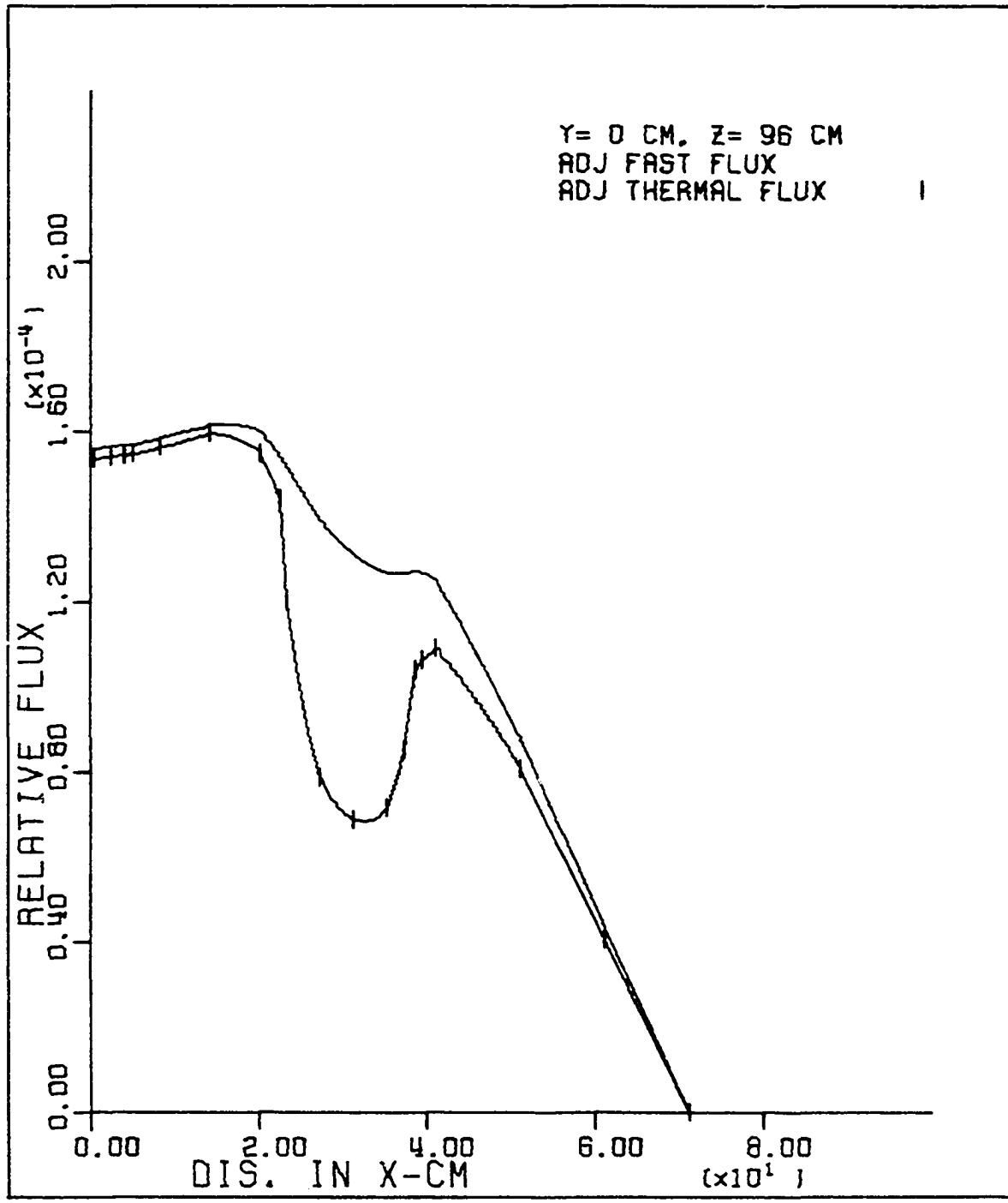

Figure 4.4. Fast and thermal adjoint flux distribution along the X-axis crossing the water region in the core tank of the UTR-10

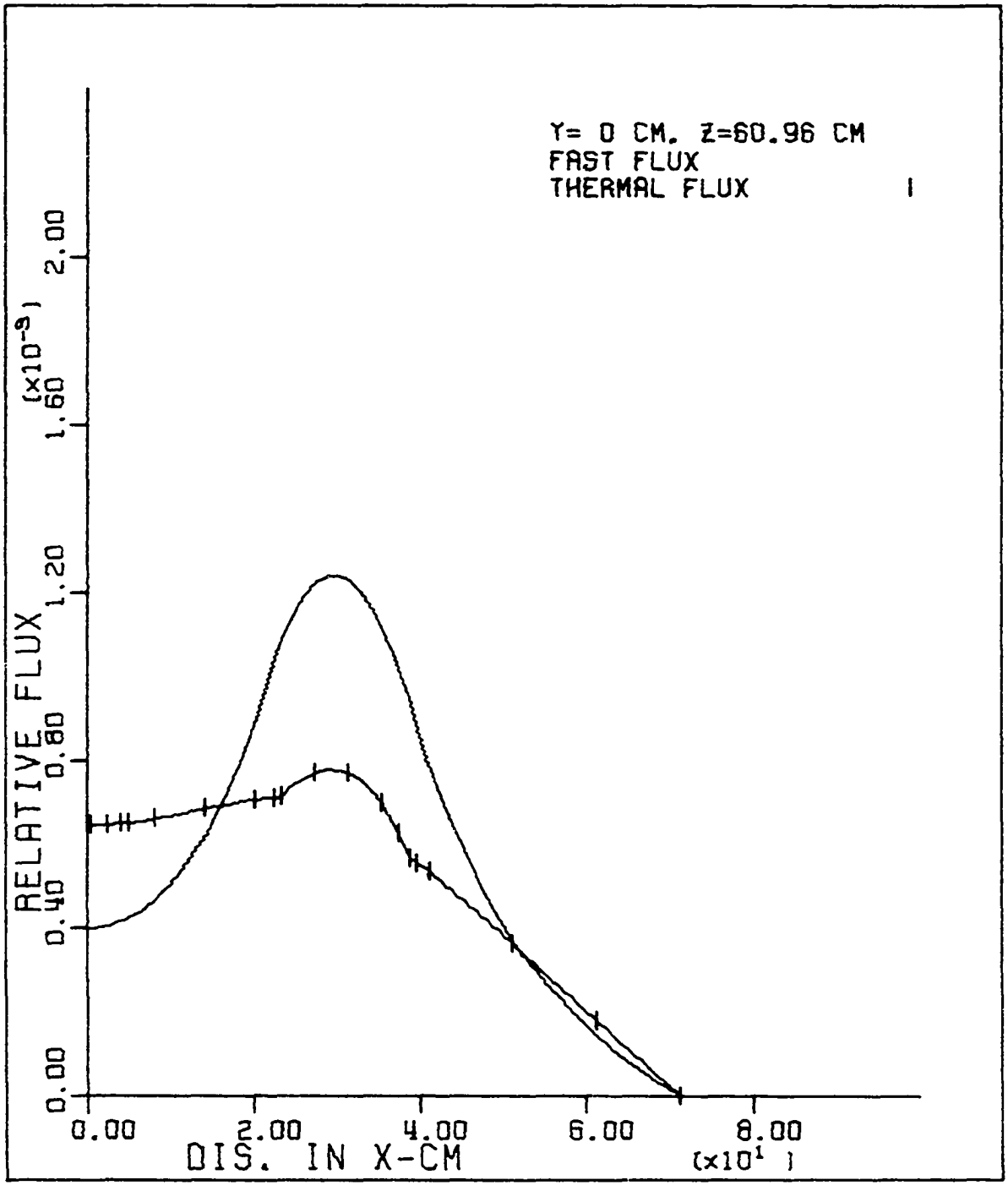

Figure 4.5. Fast and thermal flux distribution along the X-axis crossing the fuel region in the core tank of the UTR-10

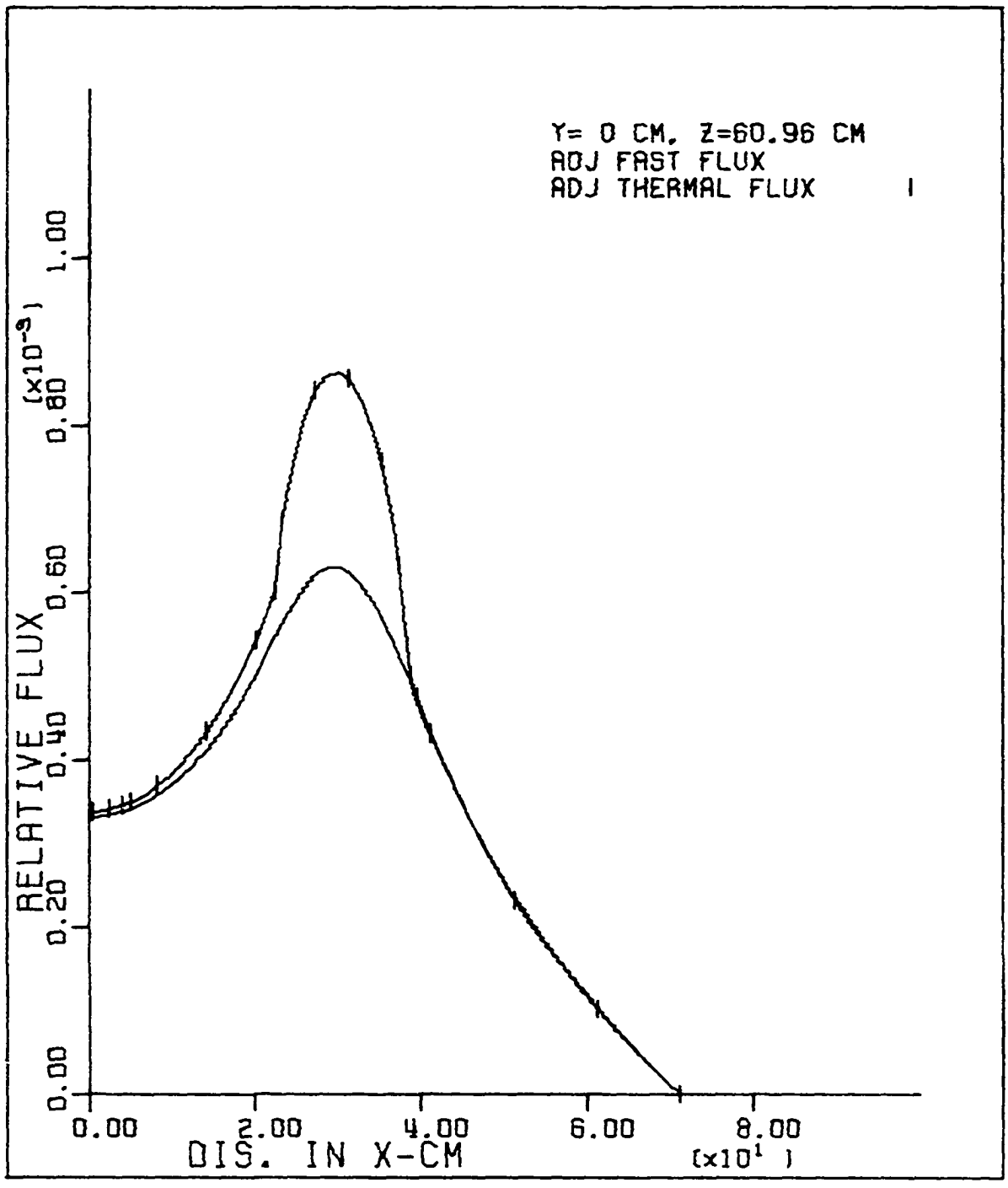

Figure 4.6. Fast and thermal adjoint flux distribution along the X-axis crossing the fuel region in the core tank of the UTR-10

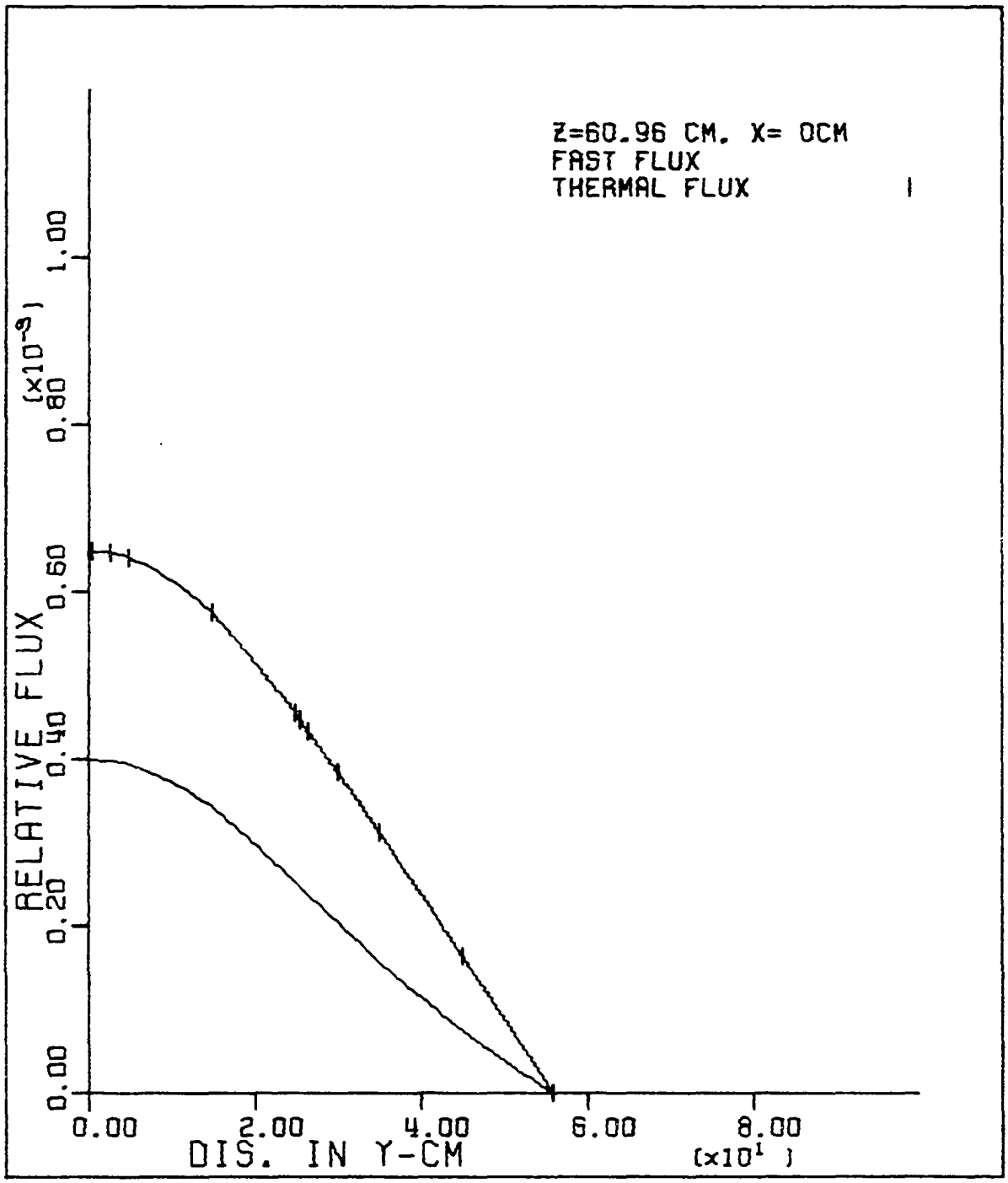

Figure 4.7. Fast and thermal flux distribution along the Y-axis crossing the internal graphite reflector region of the UTR-10

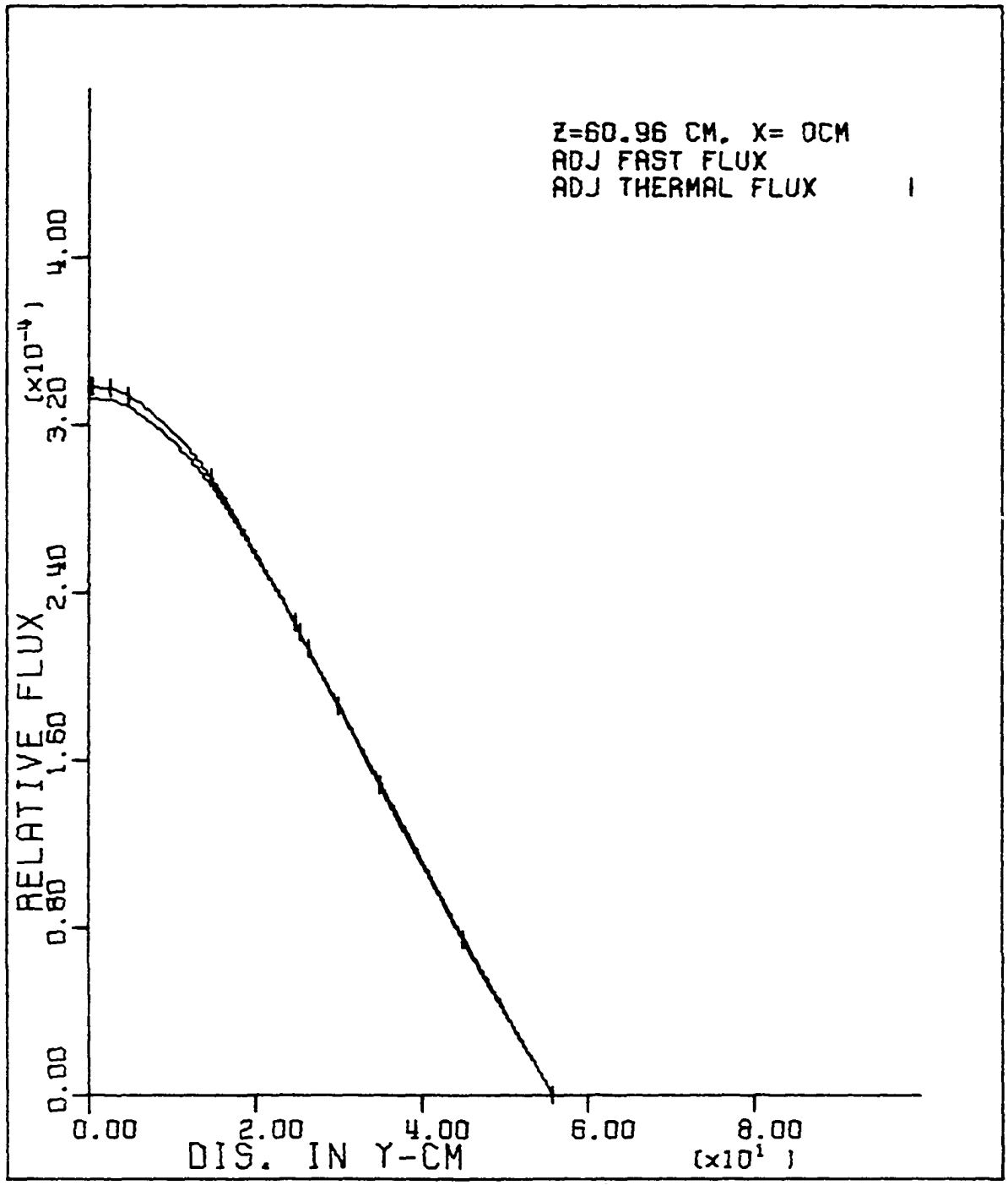

Figure 4.8. Fast and thermal adjoint flux distribution along the Y-axis crossing the internal graphite reflector region of the UTR-10

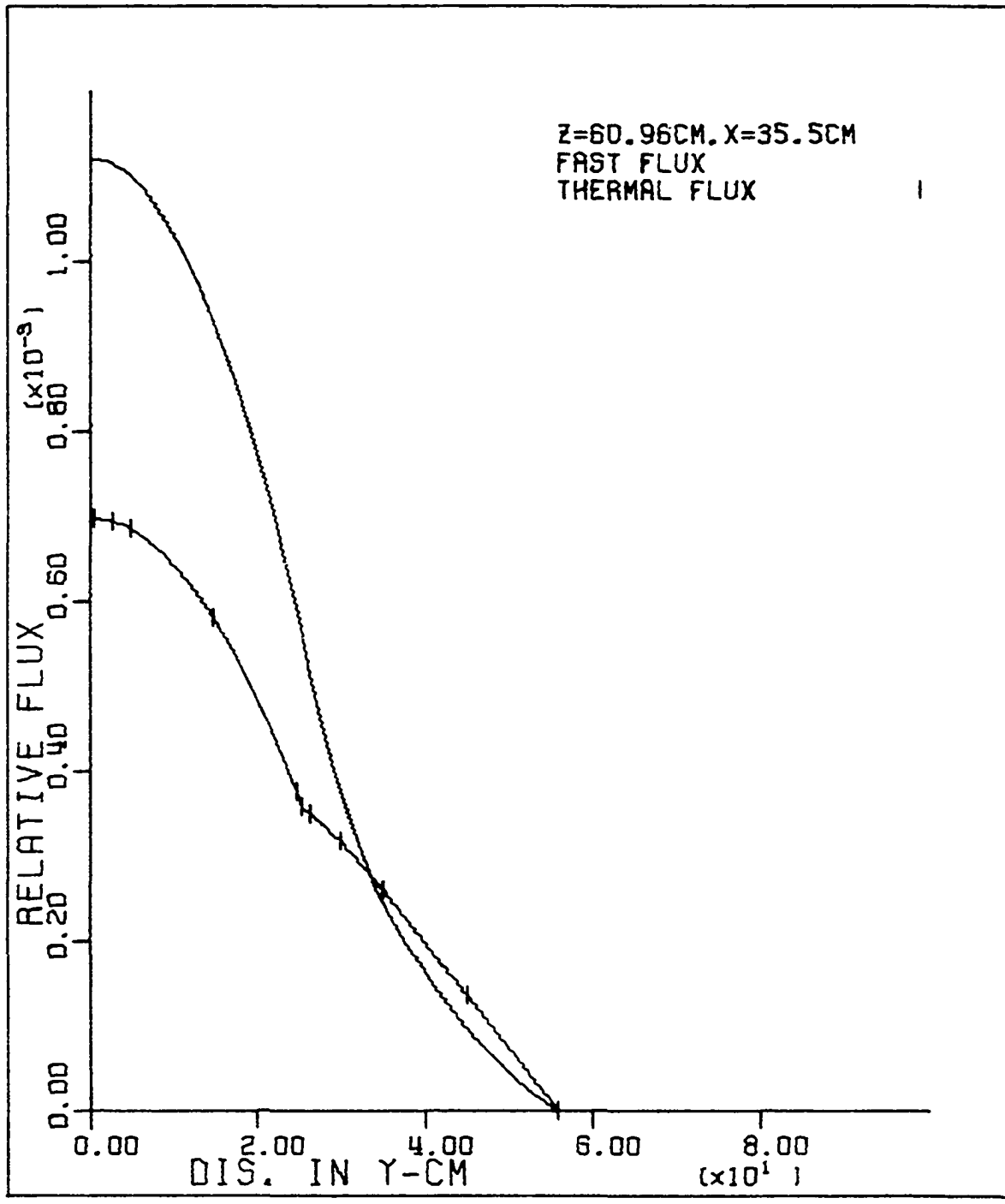

Figure 4.9. Fast and thermal flux distribution along the Y-axis crossing the fuel region of the UTR-10

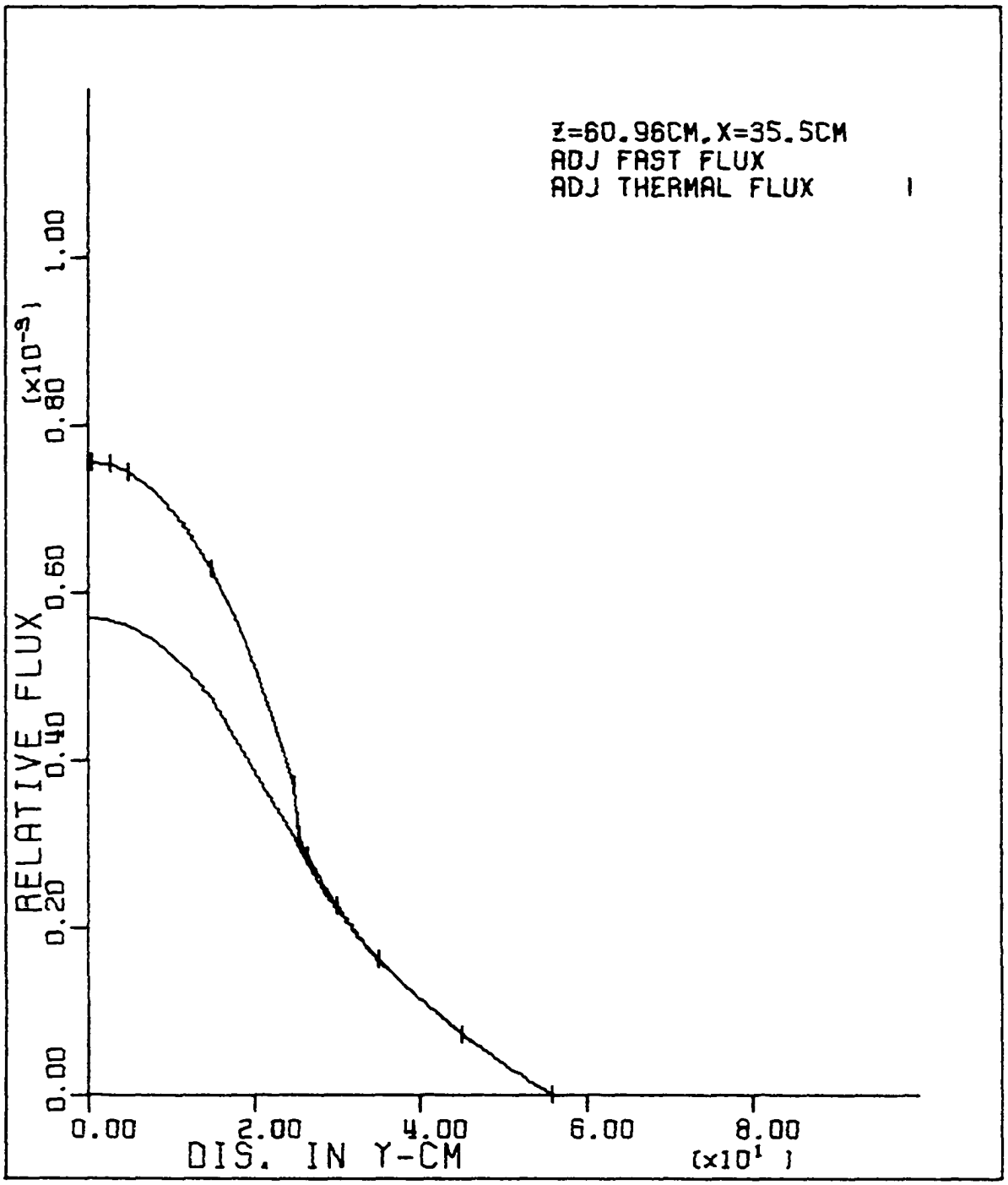

Figure 4.10. Fast and thermal adjoint flux distribution along the Y-axis crossing the fuel region of the UTR-10

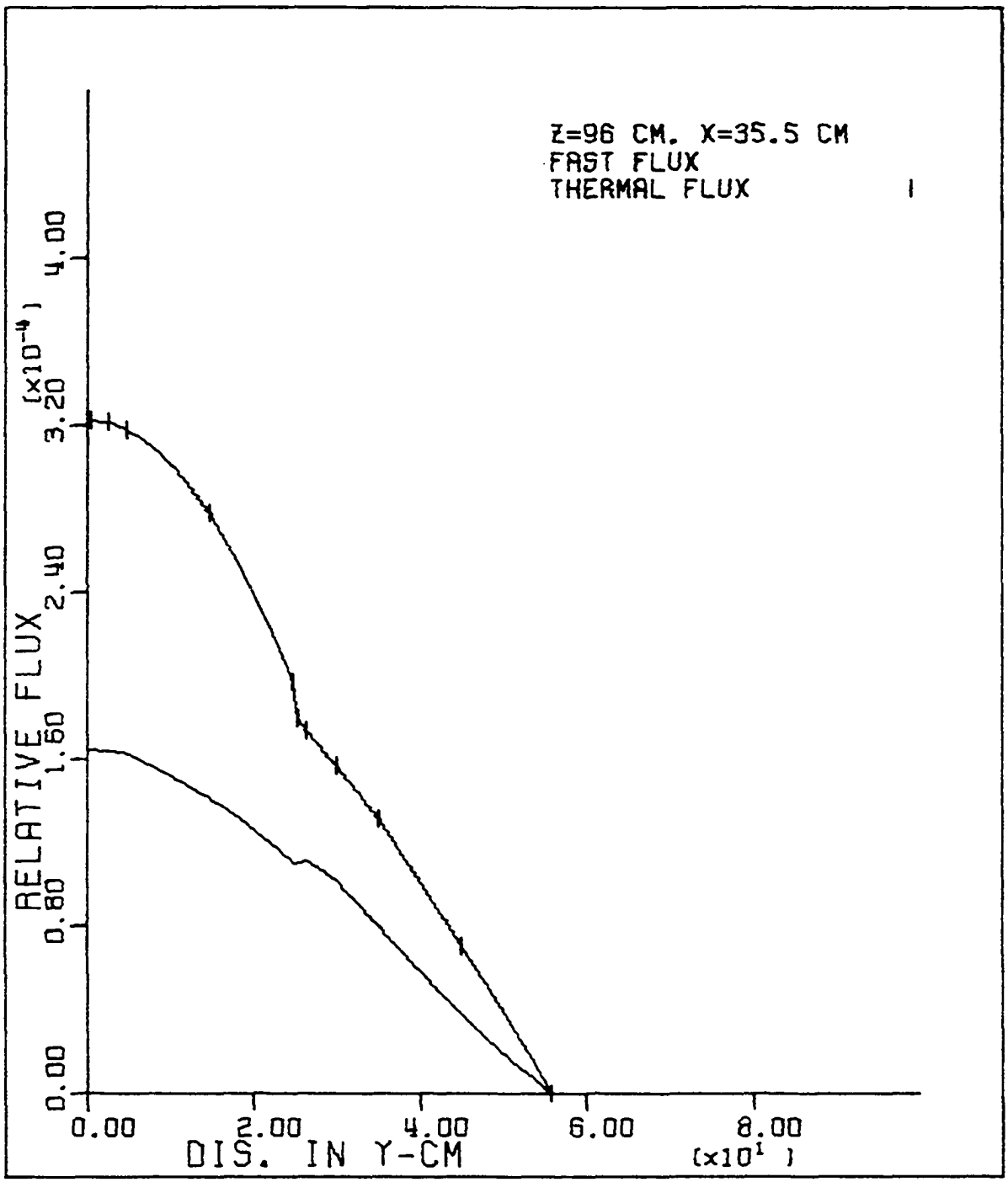

Figure 4.11. Fast and thermal flux distribution along the Y-axis crossing the water region in the core tank of the UTR-10

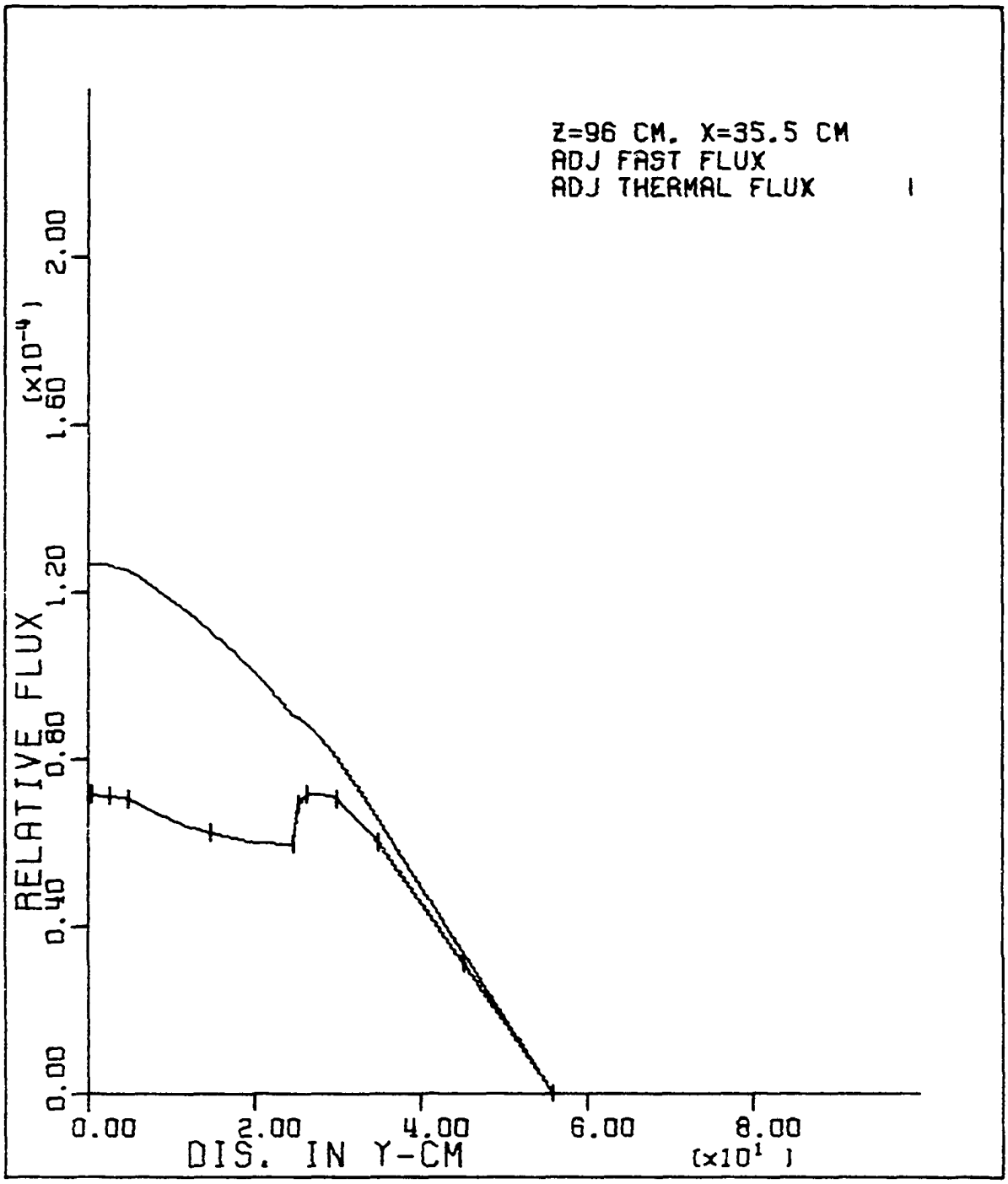

Figure 4.12. Fast and thermal adjoint flux distribution along the Y-axis crossing the water region in the core tank of the UTR-10

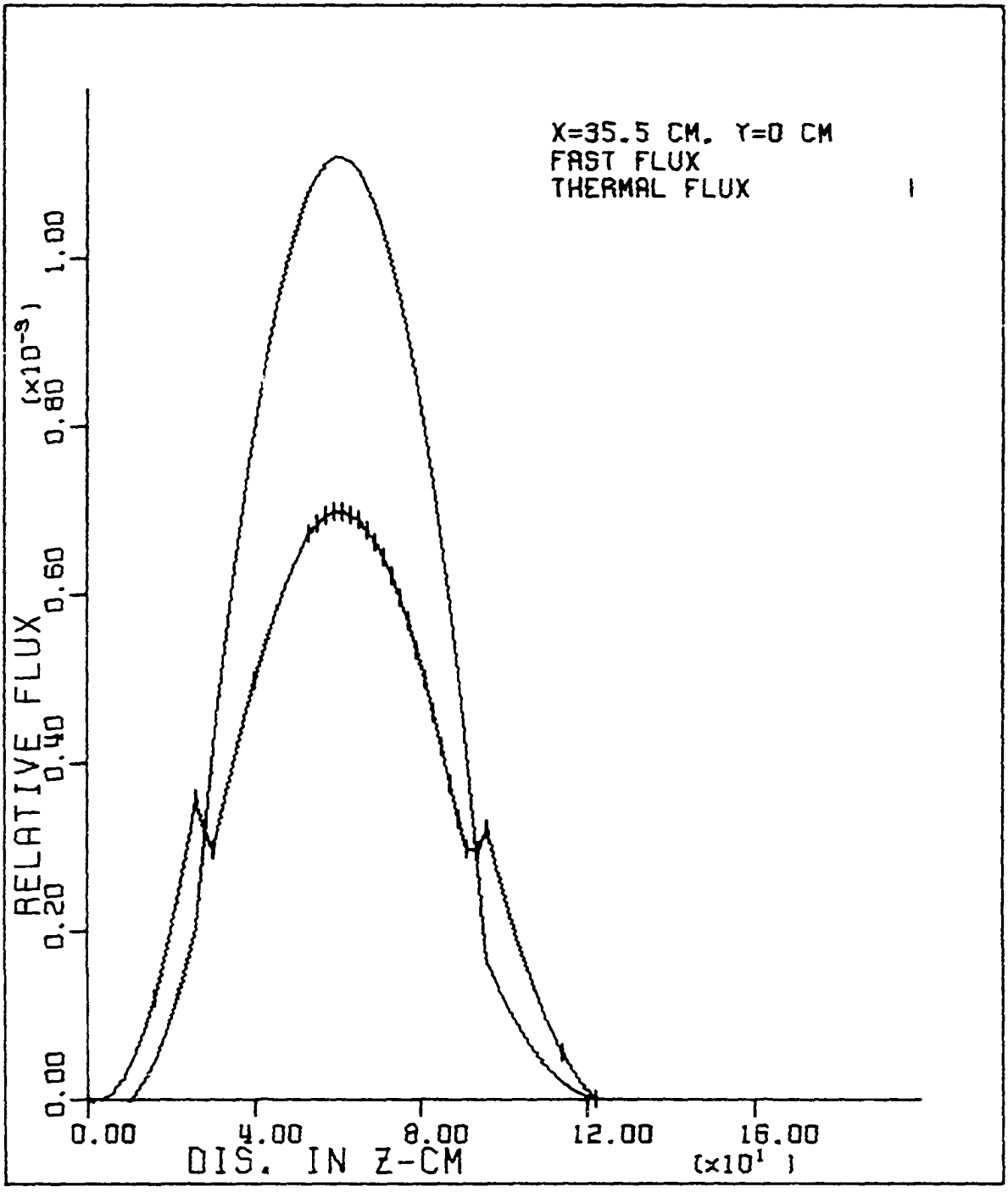

Figure 4.13. Fast and thermal flux distribution along the Z-axis in the core tank of the UTR-10

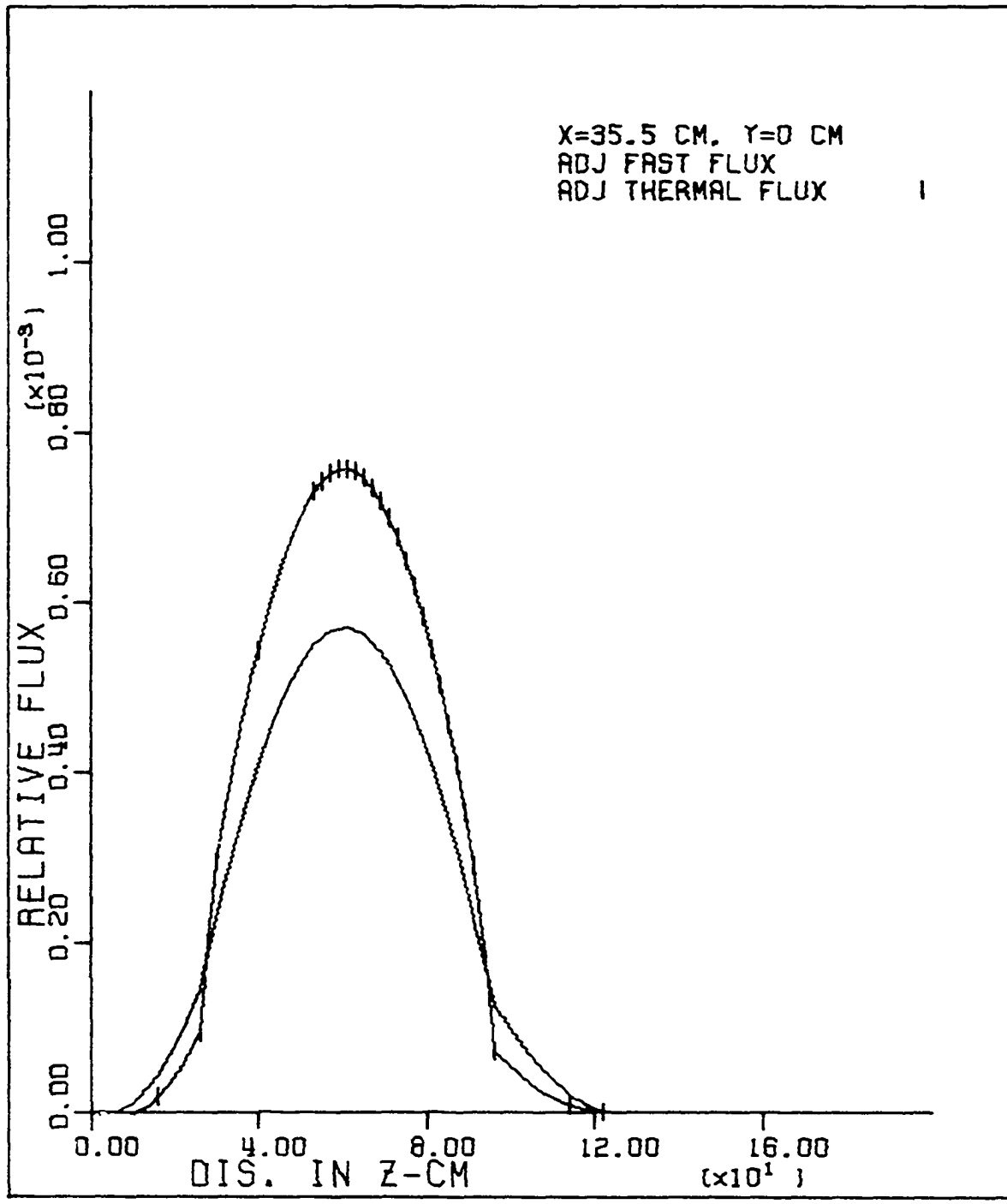

Figure 4.14. Fast and thermal adjoint flux distribution along the Z-axis in the core tank of the UTR-10

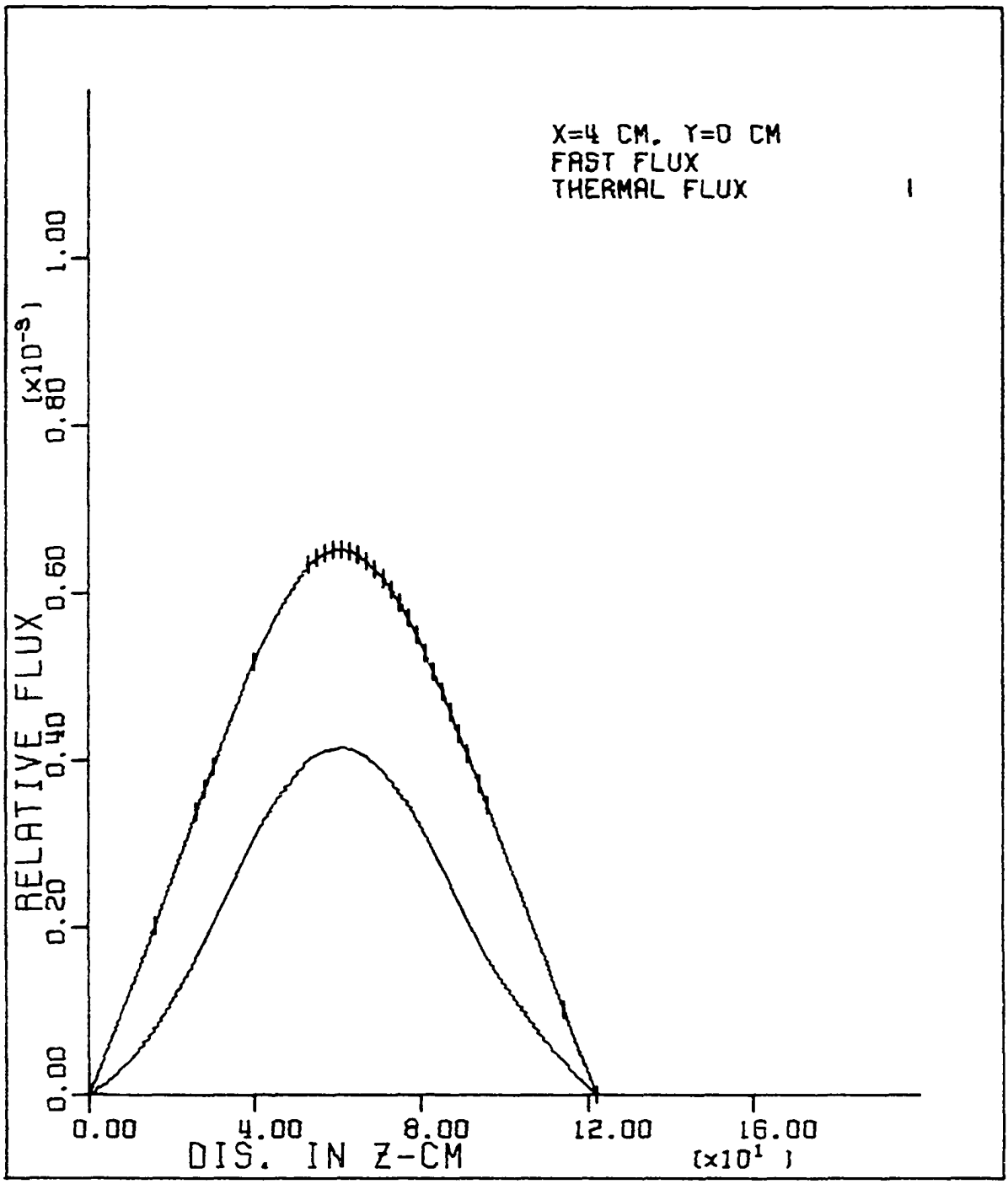

Figure 4.15. Fast and thermal flux distribution along the Z-axis in the internal graphite reflector region of the UTR-10

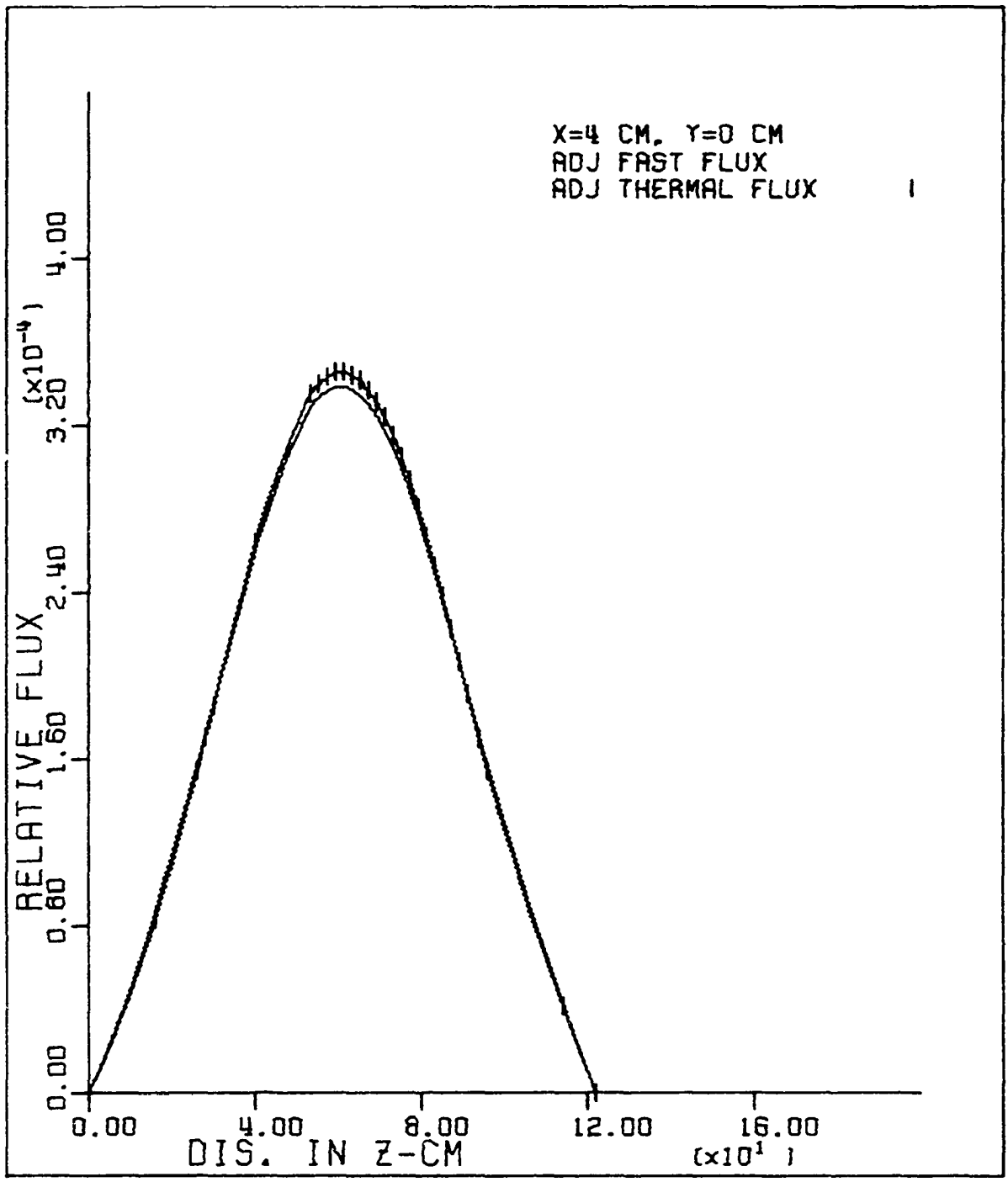

Figure 4.16. Fast and thermal adjoint flux distribution along the Z-axis in the internal graphite reflector region of the UTR-10

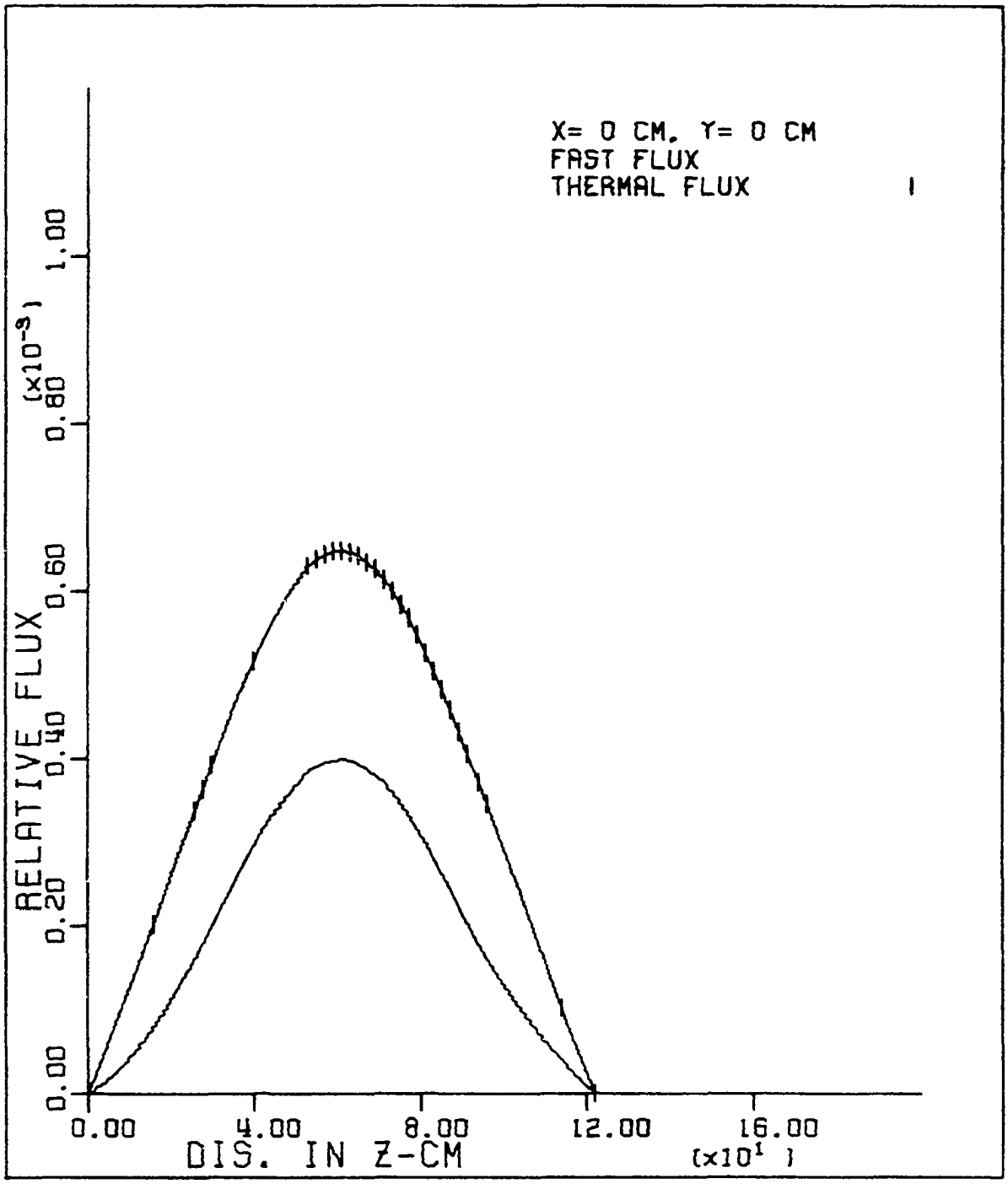

Figure 4.17. Fast and thermal flux distribution along the Z-axis at the centerline of the internal graphite reflector region of the UTR-10

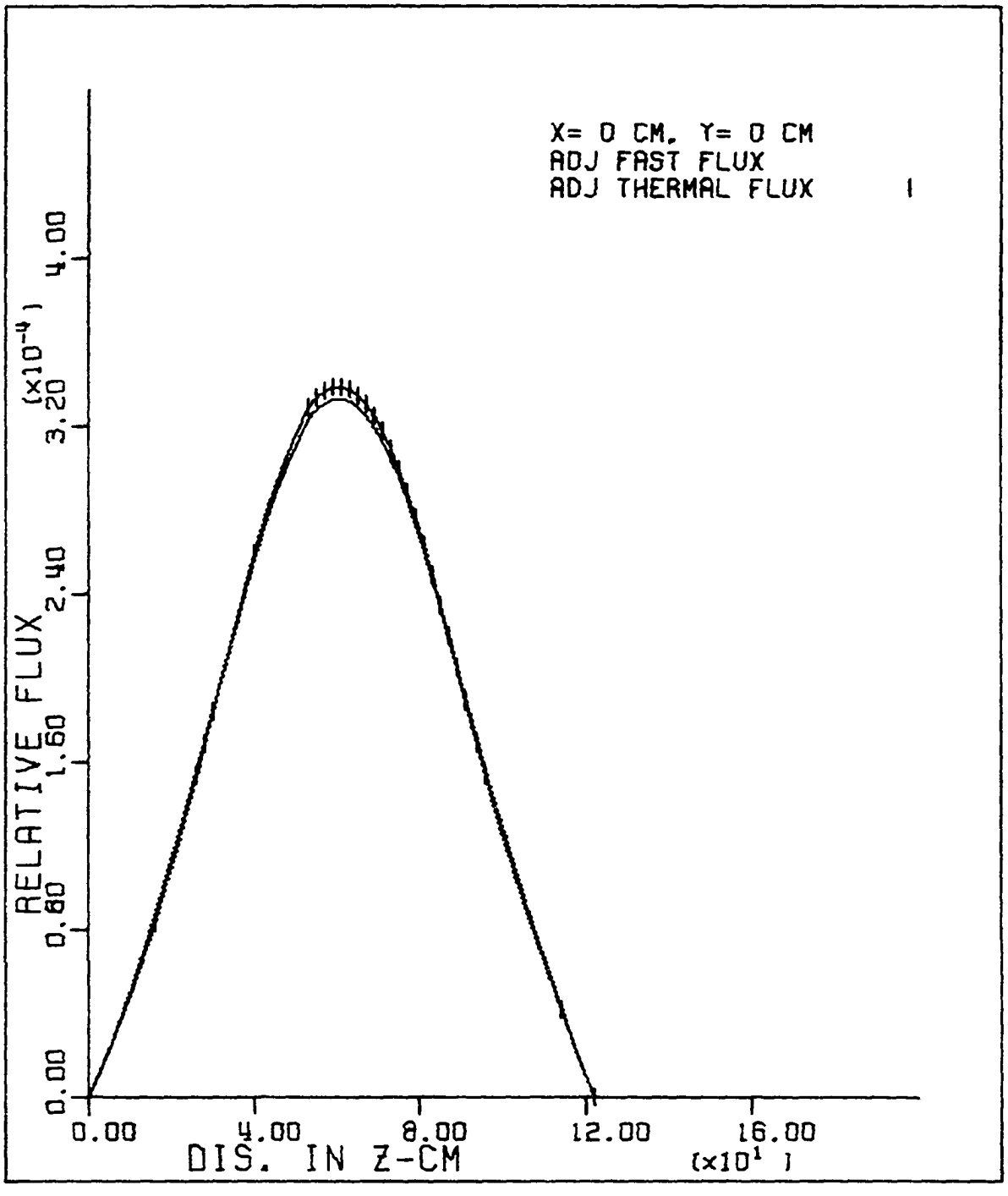

Figure 4.18. Fast and thermal adjoint flux distribution along the Z-axis at the centerline of the internal graphite reflector region of the UTR-10

1. The amplitude of the thermal adjoint flux is higher than that of the fast adjoint flux in the fuel region. This is because that, in a thermal reactor, almost all of the fission events are induced by thermal neutrons. The result is that the thermal neutrons are more important than the fast neutrons in the fuel region.
2. The amplitude of the thermal adjoint flux is lower than that of the fast adjoint flux in the water region of the core tank. This is mainly due to the fact that in the water region, the water serves as an absorber of the thermal neutrons. Thus, the thermal neutrons are less important than the fast neutrons in the water regions. Thermal neutrons have less chance of reaching the fuel region and producing a fission than fast neutrons.

The calculation of the adjoint fluxes with a noise source and the detector, and the evaluation of the detector response function will be shown and discussed in Chapter V.

V. WHIRLAWAY-H RESULTS

The purpose of this chapter is to discuss the calculated results and the analytical techniques used in evaluating the detector response model developed in Chapter III. The WHIRLAWAY-H code and the three-dimensional UTR-10 model described in Chapter IV were used in the modeling calculation. At different detector positions the fluxes and the adjoint fluxes were calculated and compared with their steady state values. The flux-adjoint flux regional integrals and then the detector response model described by Equation (3.65) were calculated for the frequency range of interest; i.e., $\lambda << \omega << \beta/\ell$.

The source of the noise disturbance was assumed to be due to the uniform void generation inside a water bubbler 5 cm in diameter and 10 cm in height. This water bubbler was placed in the center of the graphite central vertical stringer region. A neutron detector, 2.5 cm in diameter and 5 cm long, was placed adjacent to the noise source region. Since the WHIRLAWAY-H code handles only rectangular geometry, the dimensions of the noise source were taken to be 5 cm x 5 cm x 10 cm and the neutron detector taken as 2.5 cm x 2.5 cm x 5 cm in the modeling calculations. The schematic cross-sectional diagram for the above configuration is shown in Figure 4.2. It should be noted that the center point of this detector is located at X = 4 cm, Y = 0 cm and Z = 60.96 cm as shown in Figure 4.2.

In all the modeling calculations, the frequency range of interest was taken to be between 0.1 Hz to 10 Hz. In this frequency

region, ψ_1 and ψ_2 are real and are frequency independent as shown in Chapter III. The bubbles generated inside the water bubbler were assumed to be infinitely small, and produce a uniformly distributed void distribution. Thus, the fluctuations δD and $\delta\Sigma$ can be treated as spatial independent inside the noise source region.

A. The Adjoint Flux Distribution for Different Detector Positions

As pointed out in Chapter III, the two-group adjoint fluxes can be calculated from Equation (3.63)

$$L^{+}\underline{\psi}(\vec{r}) = \underline{\Sigma}_d(\vec{r}) \ . \tag{3.63}$$

The response of a neutron detector to the fluctuation of nuclear parameters is given by Equation (3.40a) and (3.40b)

$$\delta R(\vec{r}_s,\vec{r}_d,\omega) = \langle \underline{\Sigma}_d(\vec{r}),\ \delta\underline{\phi}(\vec{r},\omega)\rangle \tag{3.40a}$$

$$= \langle \underline{\psi}(\vec{r}),\ \underline{S}(\vec{r},\omega)\rangle . \tag{3.40b}$$

Note that δR depends on the location of the detector relative to the perturbation. The adjoint flux, $\psi(\vec{r})$, scales directly as $\underline{\Sigma}_d(\vec{r})$, so increasing $\underline{\Sigma}_d(\vec{r})$ increases $\psi(\vec{r})$ directly. Changing $\underline{\Sigma}_d(\vec{r})$ also reflects directly in changing δR in Equation (3.40a). This implies that the detector cross section $\underline{\Sigma}_d(\vec{r})$ can be arbitrarily chosen without affecting the relative amplitudes of δR at different detector positions. The shape of the detector response function δR rather than the absolute value of δR is the main interest of this research. Thus,

for a thermal neutron detector, $\underline{\Sigma}_d(\vec{r})$ can be chosen as

$$\underline{\Sigma}_d(\vec{r}) = \begin{bmatrix} \Sigma_{d1}(\vec{r}) \\ \Sigma_{d2}(\vec{r}) \end{bmatrix} = \begin{bmatrix} 0 \\ 1 \end{bmatrix} \tag{5.1}$$

in the modeling calculation.

Using the reactor configuration shown in Figure 4.2, the adjoint fluxes were calculated using WHIRLAWAY-H by solving Equations (3.63) and (5.1). Some illustrative results are shown in Figures 5.1, 5.2 and 5.3. Figure 5.1 shows the solutions for the adjoint fluxes along the X axis with a 5 cm x 5 cm x 10 cm water bubbler (noise source) placed at the center of the central vertical stringer region and a 2.5 cm x 2.5 cm x 5 cm neutron detector located at X = 4 cm, Y = 0 cm and Z = 60.96 cm. Comparing Figure 5.1 with Figure 4.6, the adjoint fluxes without a neutron detector, some important differences are noted:

1. The thermal adjoint flux of Figure 5.1 has a very sharp peak at the detector position whereas the thermal adjoint flux without the detector (Figure 4.6) peaks at the center of the fuel region.
2. The relative amplitude of the thermal adjoint flux at the detector position, as shown in Figure 5.1, is four to five times higher than the fast adjoint flux. However, the relative amplitude of the thermal adjoint flux to fast adjoint flux shown in Figure 4.6 is almost unity.

The difference between the adjoint flux distribution with and

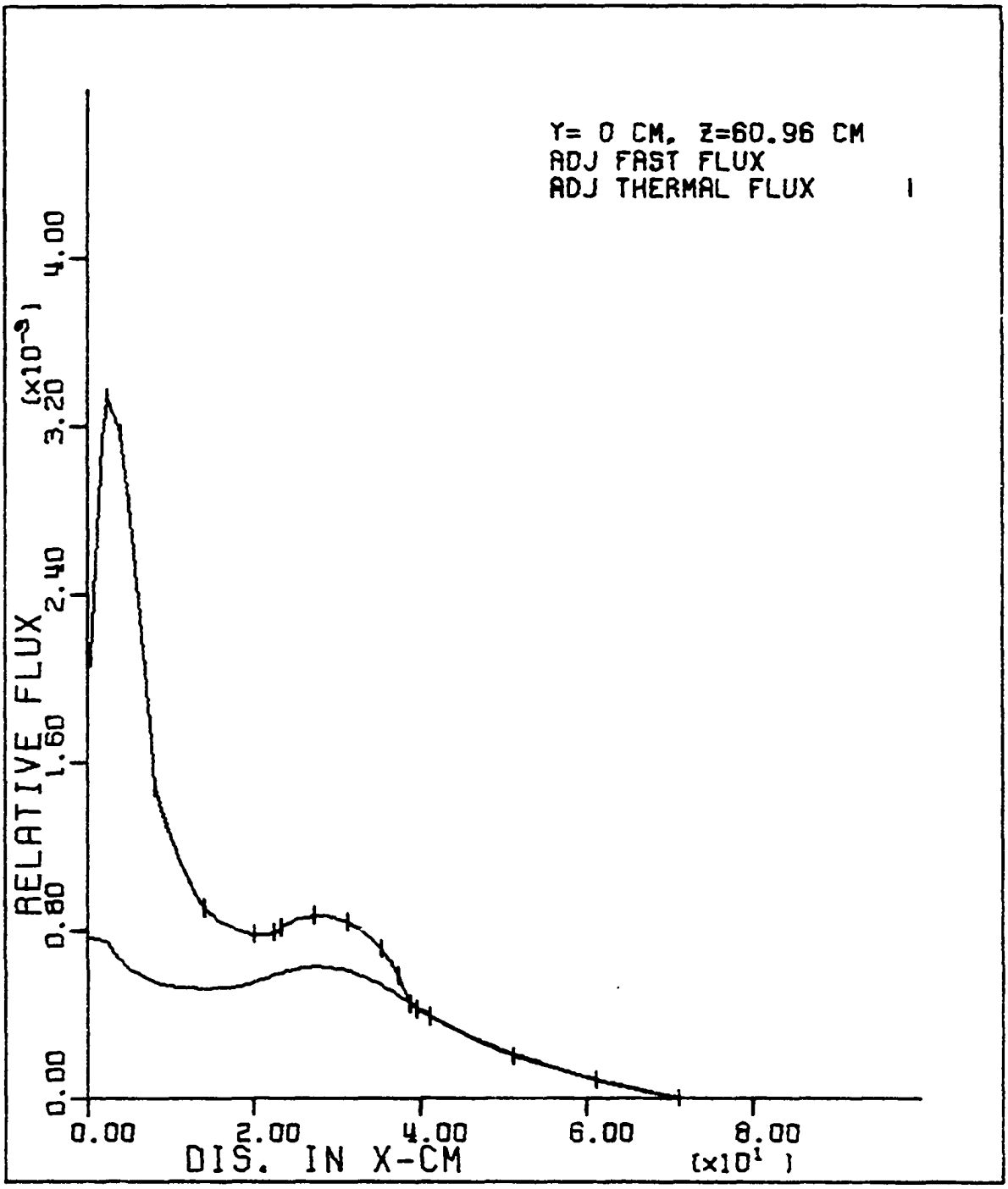

Figure 5.1. Fast and thermal adjoint flux distribution along the X-axis with a water bubbler at the origin and a detector at X = 4 cm

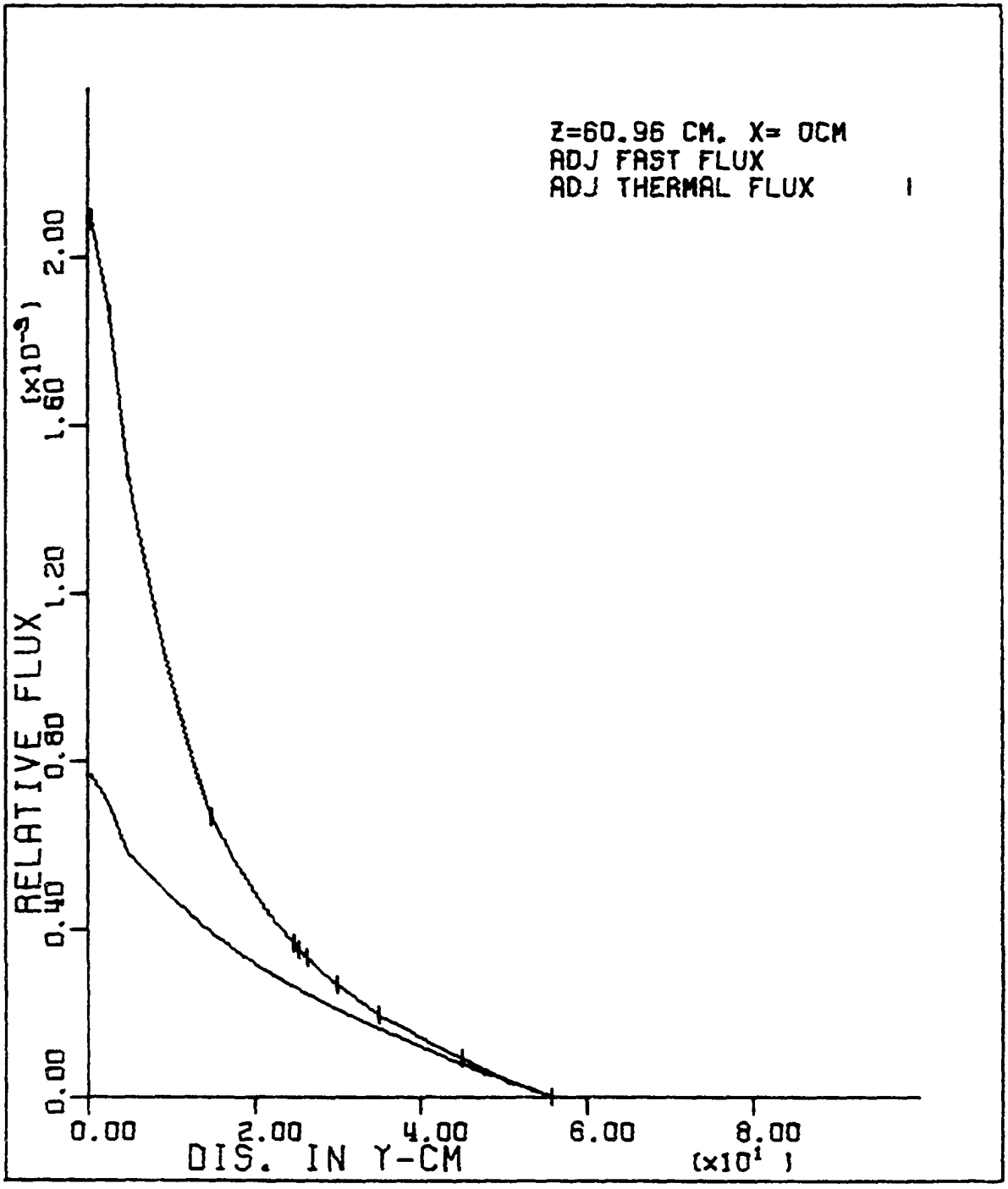

Figure 5.2. Fast and thermal adjoint flux distribution along the Y-axis with a water bubbler at the origin and a detector at Y = 0 cm

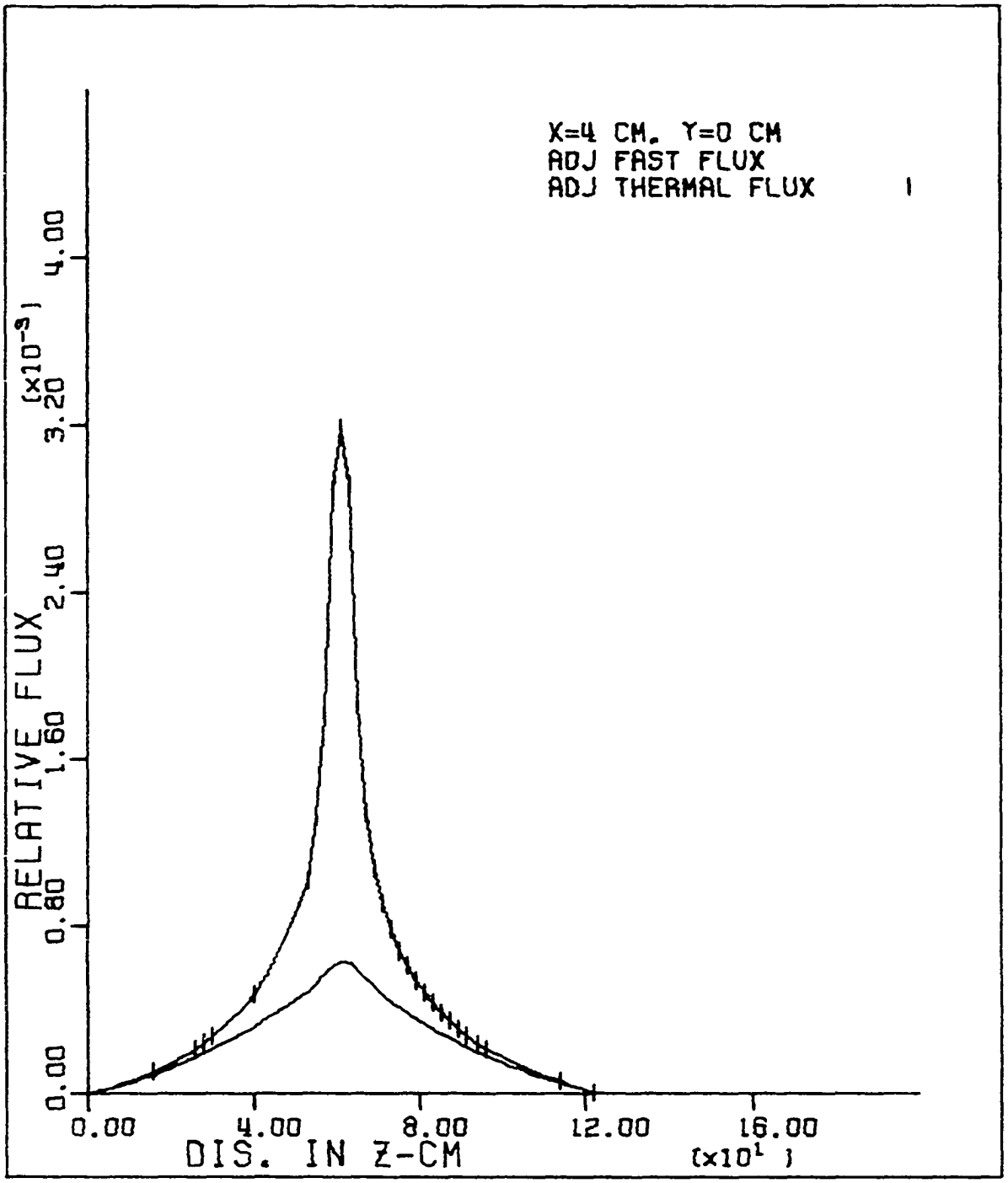

Figure 5.3. Fast and thermal adjoint flux distribution along the X-axis with a water bubbler and a detector at Z = 60.96 cm

without a detector can be seen very clearly by comparing Figure 5.2 and Figure 4.8, and also Figure 5.3 and Figure 4.16.

The flux distributions with a noise source (water bubbler) and detector were also calculated using Equation (3.56)

$$L\underline{\phi}(\vec{r}) = 0. \tag{3.56}$$

Some of the sample results for the flux distribution are shown in Figures 5.4, 5.5 and 5.6. The change of the flux shapes in the noise source region can be seen very clearly by comparing Figures 5.4, 5.5 and 5.6 to Figures 4.5, 4.7 and 4.15 respectively.

As the detector is moved upward from its original position in the center vertical stringer region, the peak positions of the adjoint fluxes also change. As expected the peaks appear at the corresponding detector positions. The results are shown in Figures 5.7 and 5.8. The relative amplitude of the thermal adjoint flux to the fast adjoint flux, and the difference between the two fluxes are shown in Figure 5.9.

B. The Detector Response Function

Before starting the evaluation of the detector response function, defined in Equation (3.65), a simple analysis is given here to illustrate the correlations between the adjoint functions and the detector response.

Consider a point source given in the form

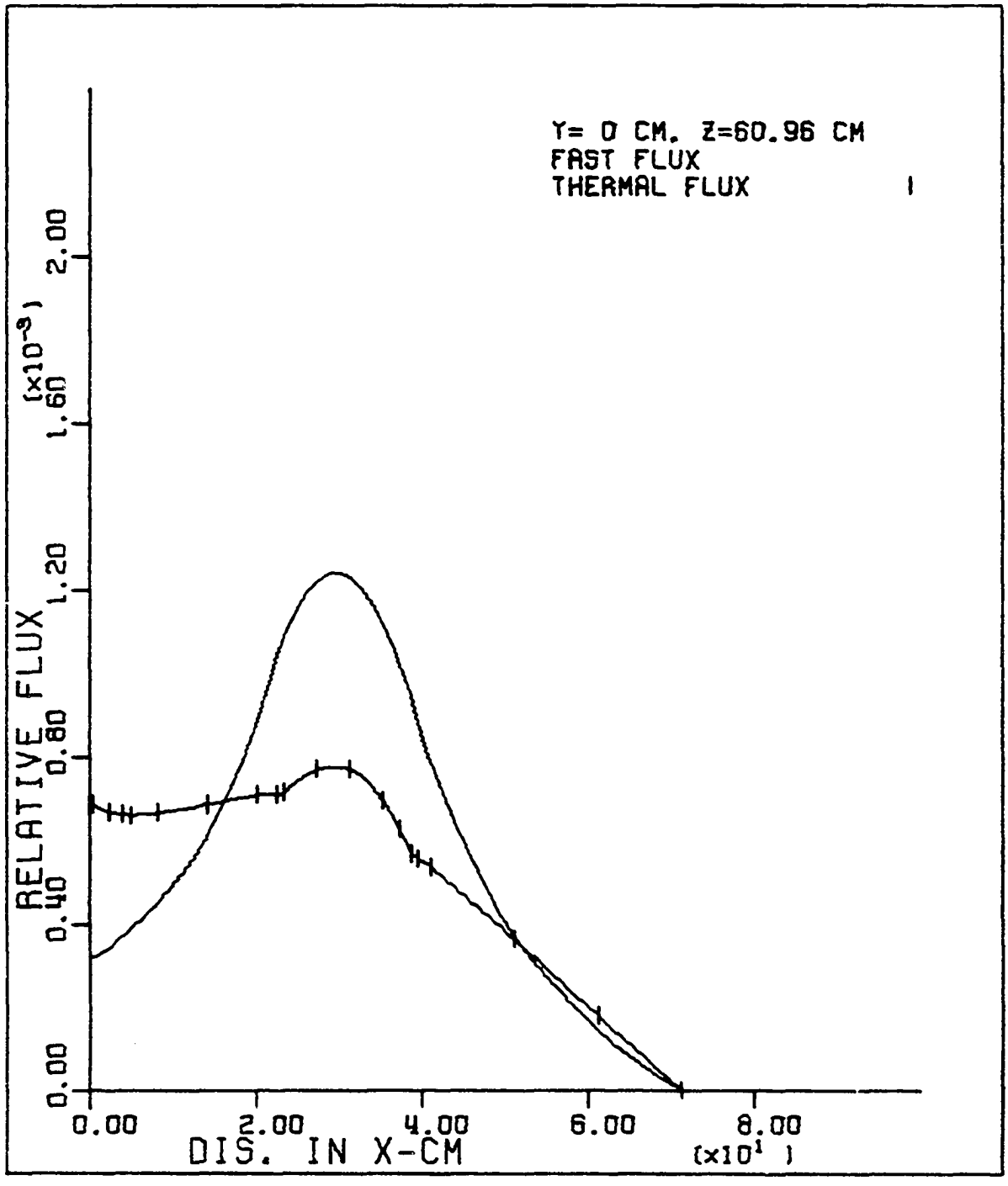

Figure 5.4. Fast and thermal flux distribution along the X-axis with a 5 cm x 5 cm x 10 cm water bubbler at the origin

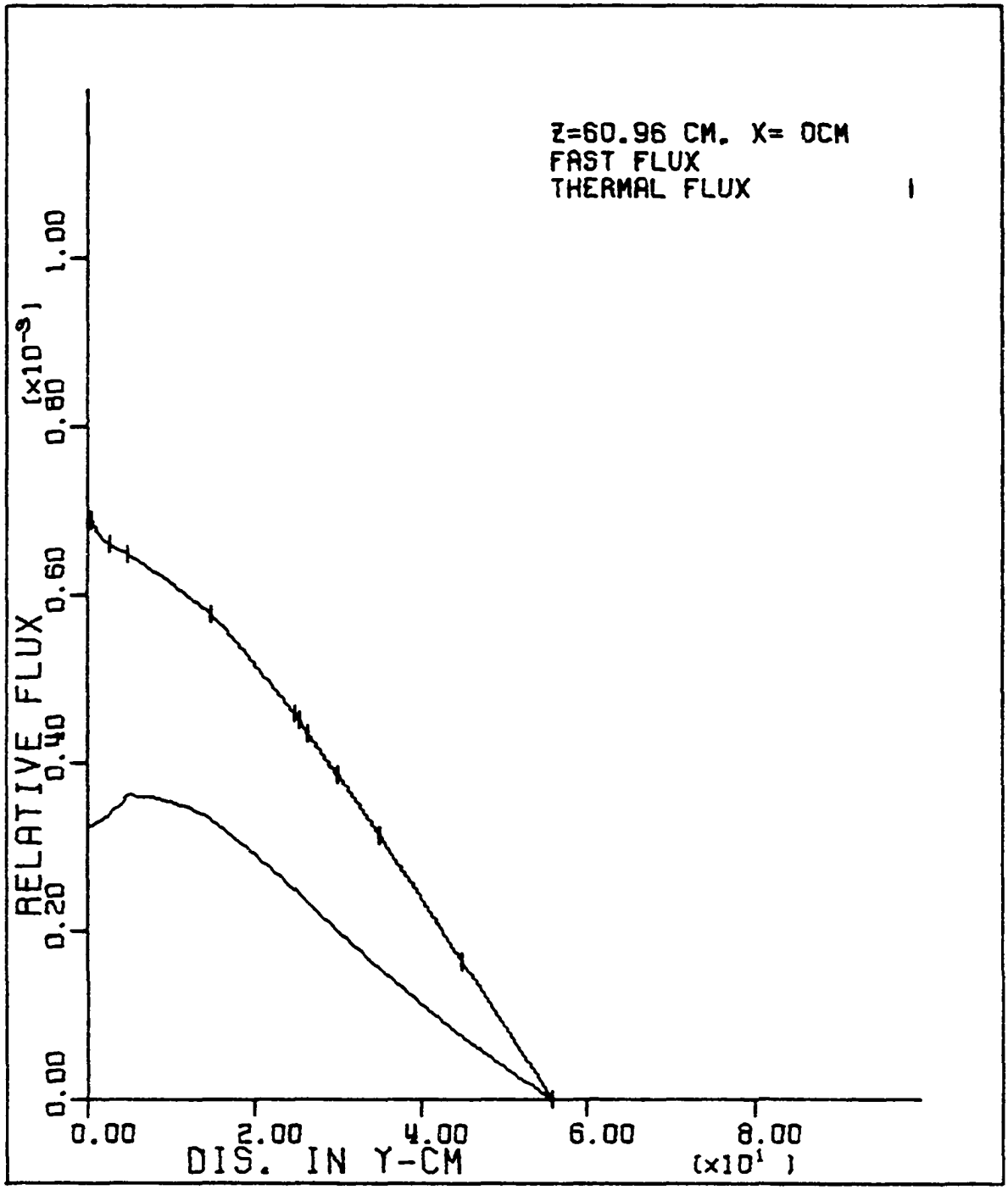

Figure 5.5. Fast and thermal flux distribution along the Y-axis with a 5 cm x 5 cm x 10 cm water bubbler at the origin

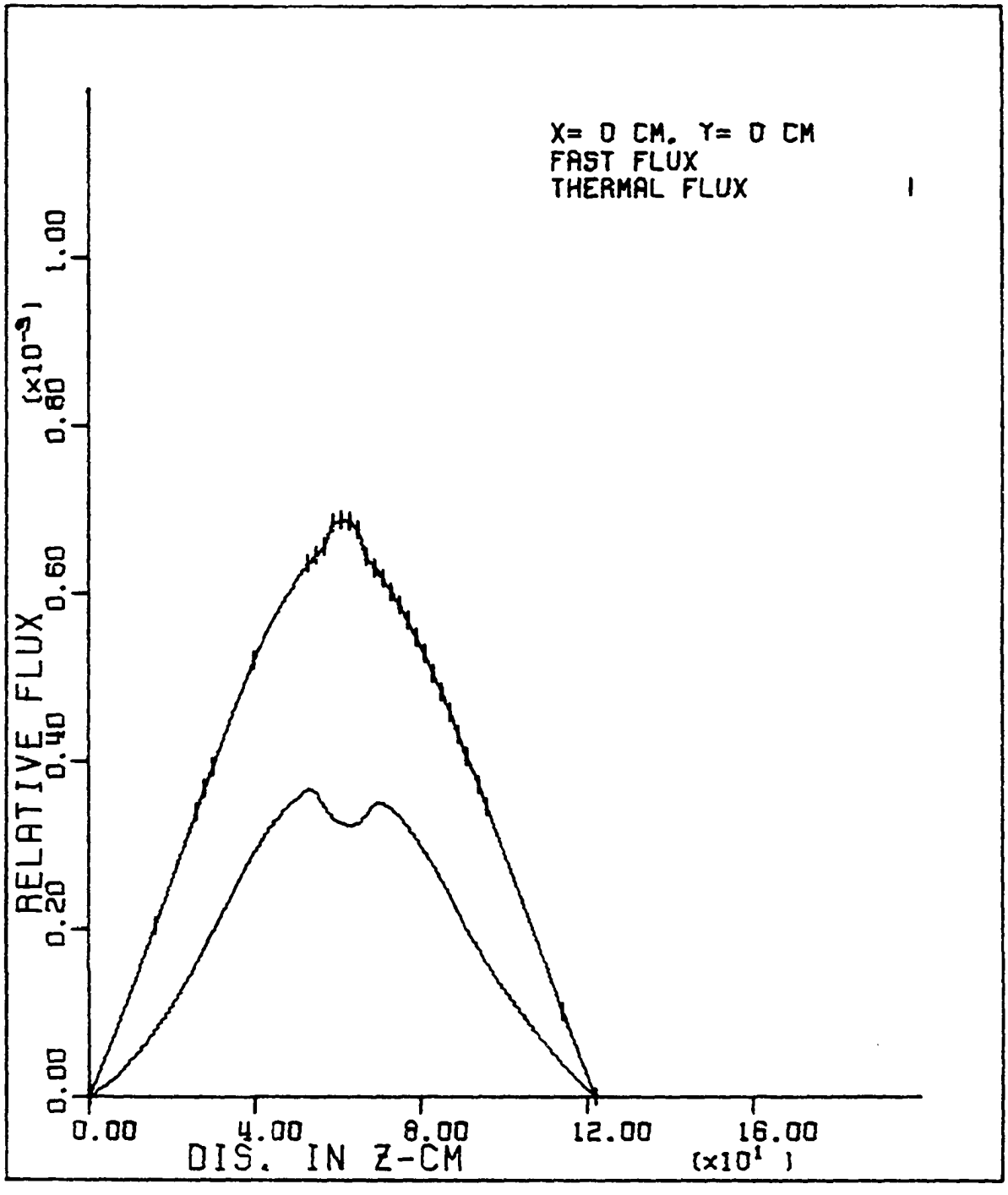

Figure 5.6. Fast and thermal flux distribution along the Z-axis for a 5 cm x 5 cm x 10 cm water bubbler at Z = 60.96 cm

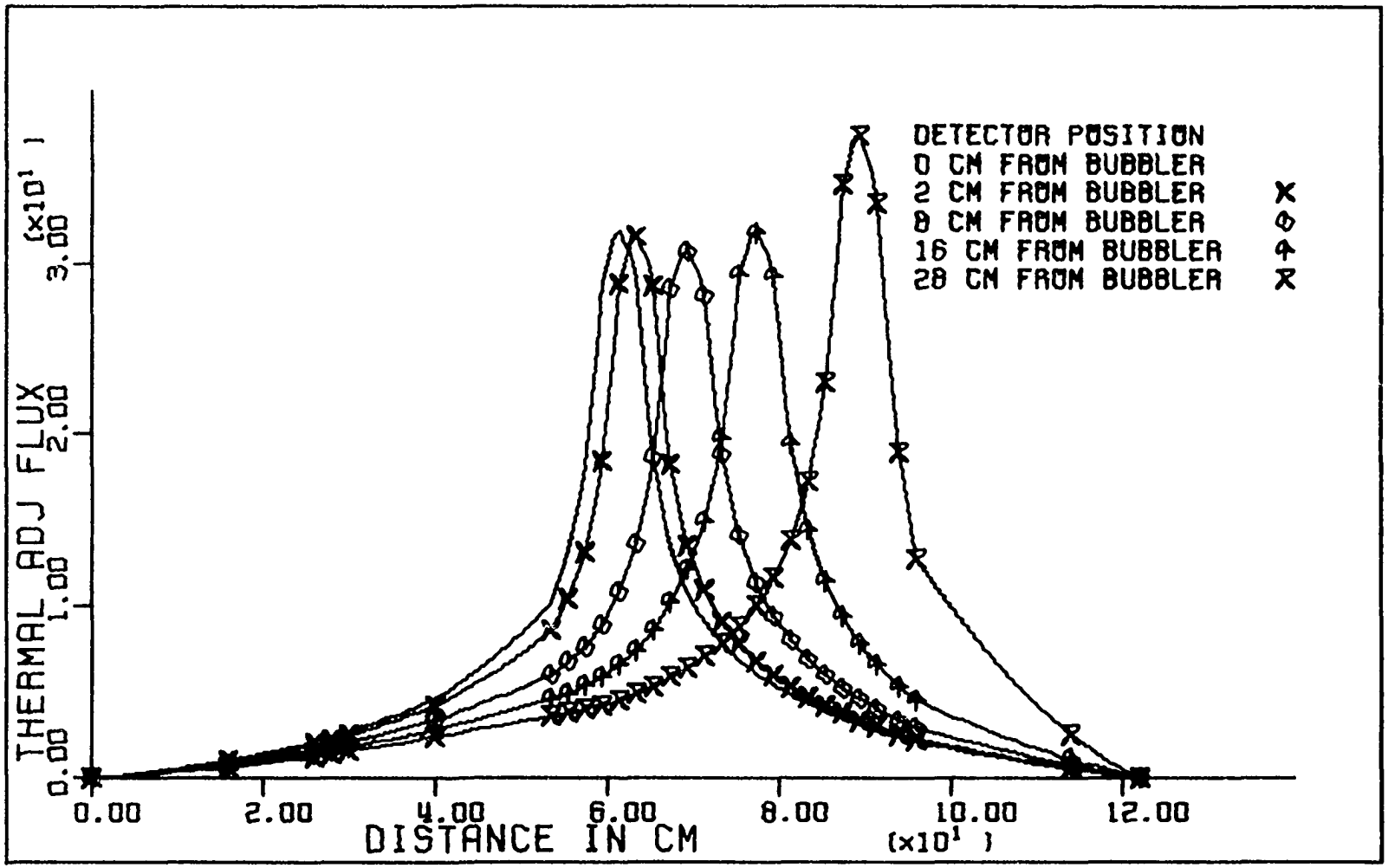

Figure 5.7. The thermal adjoint fluxes for different detector positions from the water bubbler located at Z = 60.96 cm

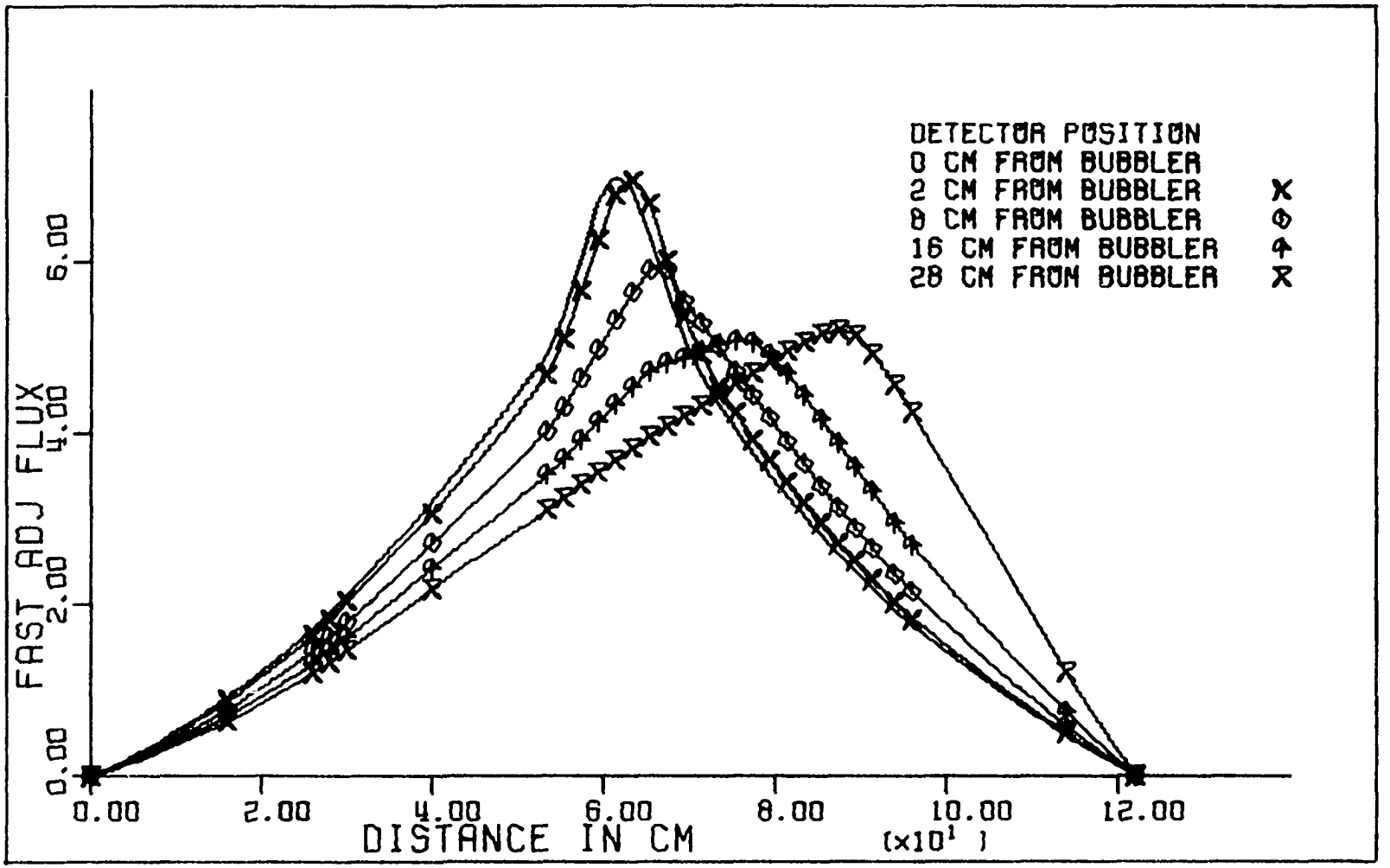

Figure 5.8. The fast adjoint fluxes for different detector positions from the water bubbler located at Z = 60.96 cm

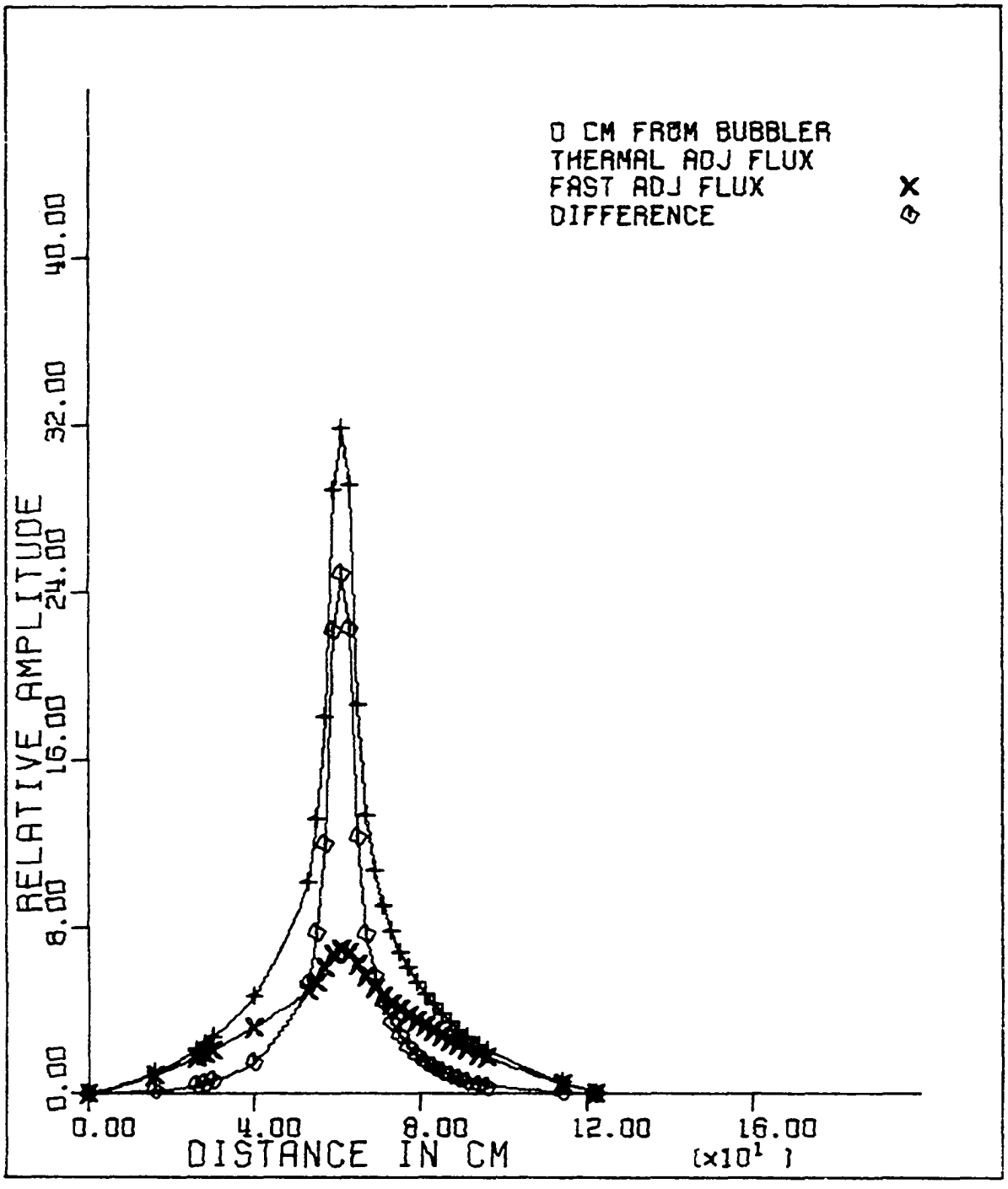

Figure 5.9. The comparison of fast and thermal adjoint fluxes at the detector position 0 cm from water bubbler

$$\delta\Sigma_2(\vec{r},\omega) = \delta\Sigma_2(\omega)\delta(\vec{r}-\vec{r}_s). \tag{5.2}$$

This perturbation corresponds to the case of a localized thermal absorber of variable strength (for different ω) introduced at $\vec{r}_s$. Substituting Equation (5.2) into Equation (3.65) yields

$$\begin{aligned}\delta R(\vec{r}_s,\vec{r}_d,\omega) &= \int_{\Delta\vec{r}_d} \Sigma_{d2}(\vec{r})\,\delta\phi_2(\vec{r},\omega)\,d\vec{r} \\ &= \int_{\Delta\vec{r}_s} \delta\Sigma_2(\omega)\delta(\vec{r}-\vec{r}_s)\phi_2(\vec{r})\psi_2(\vec{r},\vec{r}_d)\,d\vec{r} \\ &= \delta\Sigma_2(\omega)\phi_2(\vec{r}_s)\psi_2(\vec{r}_s,\vec{r}_d)\end{aligned} \tag{5.3}$$

where $\psi_2(\vec{r}_s,\vec{r}_d)$ is the value of the thermal adjoint flux at $\vec{r}_s$ due to the detector at $\vec{r}_d$.

Equation (5.3) states that, with the point perturbation in the form of Equation (5.2), the fluctuation of the detector response is weighted by

1. the fluctuation of the flux at $\vec{r}_d$ multiplied by the detector cross section Σ_{d2}, or
2. the magnitude of the perturbation $\delta\Sigma_2(\omega)$, the steady state thermal flux at $\vec{r}_s$, and the value of the thermal adjoint flux at $\vec{r}_s$ due to the detector at $\vec{r}_d$, $\psi_2(\vec{r}_s,\vec{r}_d)$.

The function $\psi_2(\vec{r}_s,\vec{r}_d)$ here plays a very important role in the detector response function. Note that, from Equation (5.3), $\delta\Sigma_2(\omega)$ is only a function of ω and $\phi_2(\vec{r}_s)$ is not a function of the detector location $\vec{r}_d$. Thus, for different detector locations $\vec{r}_{dl}$

and $\vec{r}_{d2}$ the ratio of the detector response functions is

$$\frac{\delta R(\vec{r}_s,\vec{r}_{d1},\omega)}{\delta R(\vec{r}_s,\vec{r}_{d2}(\omega)} = \frac{\delta\Sigma_2(\omega)\phi_2(\vec{r}_s)\psi_2(\vec{r}_s,\vec{r}_{d1})}{\delta\Sigma_2(\omega)\phi_2(\vec{r}_s)\psi_2(\vec{r}_s,\vec{r}_{d2})}$$

$$= \frac{\psi_2(\vec{r}_s,\vec{r}_{d1})}{\psi_2(\vec{r}_s,\vec{r}_{d2})} . \qquad (5.4)$$

This implies that the ratio of δR for different detector positions is equal to the ratio of $\psi_2(\vec{r}_s,\vec{r}_d)$. Thus, $\psi_2(\vec{r}_s,\vec{r}_d)$ will give a measure of the relative amplitude of δR for different detector positions.

A cross plot of the thermal adjoint flux, $\psi_2(\vec{r}_s,\vec{r}_d)$, for different detector displacements from the point noise source defined in Equation (5.2) is shown in Figure 5.10. In Figure 5.10, the point perturbation is introduced at the origin and the detector is moved away from the source of the perturbation. The function $\psi_2(\vec{r}_s,\vec{r}_d)$, which is a measure of the detector response function δR, drops very rapidly first and then decreases gradually. This clearly implies that near the point source the detector sees both the local and global component of the perturbation. As the detector is moved further away, the local component dies out and only the global component is detected. This confirms the facts found in several references [11, 37, 38, 40, 54, 74].

By a similar approach the cross plot of the fast adjoint flux, $\psi_1(\vec{r}_s,\vec{r}_d)$, was also obtained and is included in Figure 5.10. However, $\psi_1(\vec{r}_s,\vec{r}_d)$ does not have a significant local peak. This is due to the fact that the detector used in the modeling calculation is a

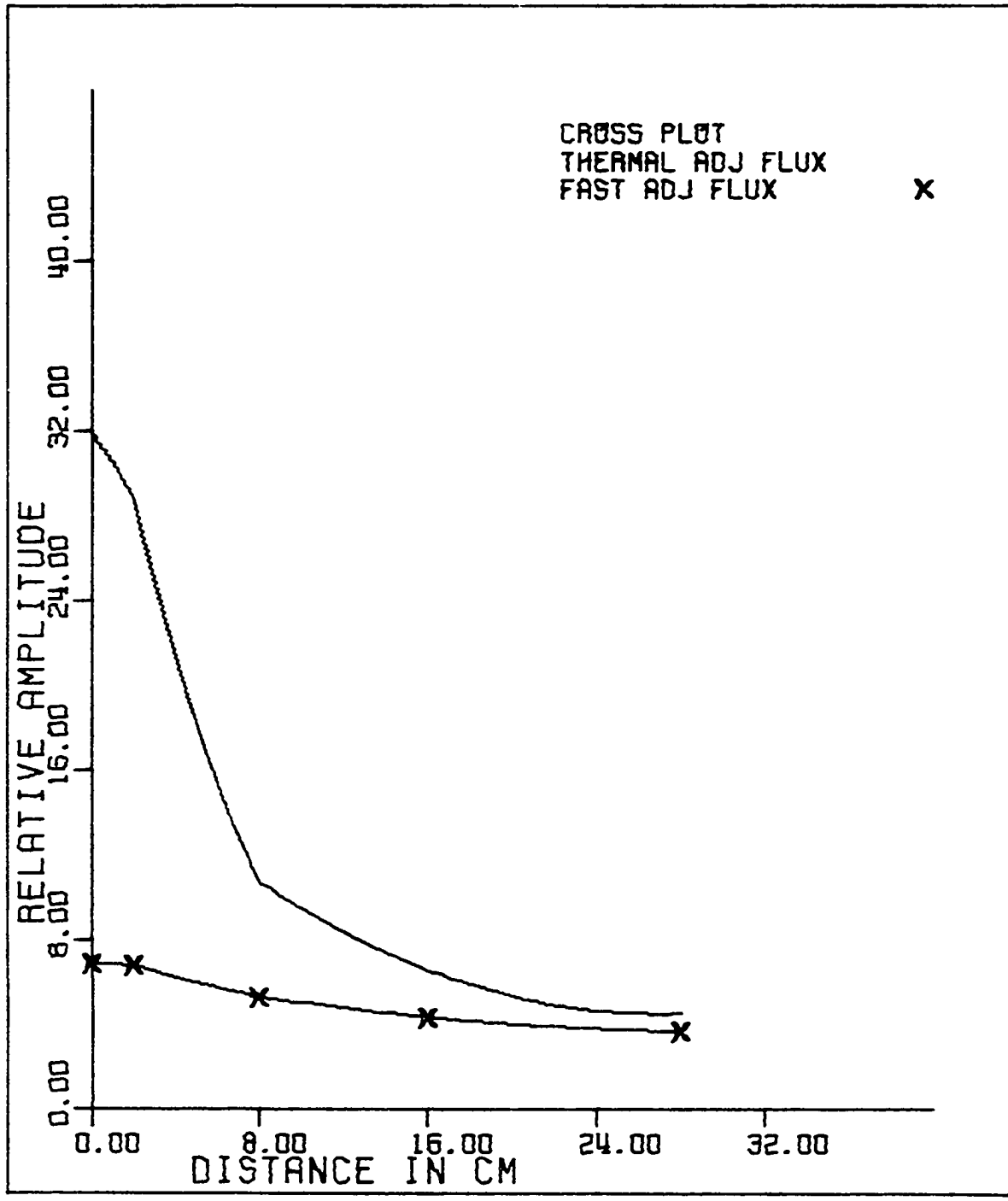

Figure 5.10. The plots of $\psi_1(\vec{r}_s,\vec{r}_d)$ and $\psi_2(\vec{r}_s,\vec{r}_d)$ as a function of detector distance from the water bubbler located at the origin

thermal neutron detector and will not detect fast neutrons.

The ratio of the APSD's$_{\delta R}$ (APSD of the detector response function) for different detector positions, according to Equations (3.71) and (5.4), can be written as

$$\frac{APSD_{\delta R}(\vec{r}_s,\vec{r}_{d1},\omega)}{APSD_{\delta R}(\vec{r}_s,\vec{r}_{d2},\omega)} = \left|\frac{\delta R(\vec{r}_s,\vec{r}_{d1},\omega)}{\delta R(\vec{r}_s,\vec{r}_{d2},\omega)}\right|^2$$

$$= \left[\frac{\psi_2(\vec{r}_s,\vec{r}_{d1})}{\psi_2(\vec{r}_s,\vec{r}_{d2})}\right]^2. \qquad (5.5)$$

This implies that the ratio of APSD$_{\delta R}$ for different detector positions is equal to the ratio of $[\psi_2(\vec{r}_s,\vec{r}_d)]^2$. If $\vec{r}_{d2}$ is chosen as the reference detector location $\vec{r}_f$, the normalized APSD$_{\delta R}$ is given by

$$NAPSD_{\delta R}(r_s,\omega) = |N\delta R(\vec{r}_s,\omega)|^2$$

$$= [\psi_{2N}(\vec{r}_s)]^2 \qquad (5.6)$$

where

$$\psi_{2N}(\vec{r}_s) = \frac{\psi_2(\vec{r}_s,\vec{r}_{d1})}{\psi_2(\vec{r}_s,\vec{r}_f)} \qquad (5.7)$$

= the value of the normalized thermal adjoint flux at $\vec{r}_s$.

For a finite volume noise source and detector, Equation (5.3) and Equation (5.5) are no longer applicable. The detector response function, δR, of a detector with a volume $\Delta\vec{r}_d$ located at $\vec{r}_d$ to a finite volume noise source introduced at $\vec{r}_s$ with volume $\Delta\vec{r}_s$ is then weighted by the following volume integrals over the noise source region

$$\delta R(\vec{r}_s,\vec{r}_d,\omega) = \delta D_1(\omega)\int_{\Delta\vec{r}_s} \nabla\phi_1(\vec{r})\nabla\psi_1(\vec{r},\vec{r}_d)d\vec{r}$$

$$+ \delta D_2(\omega)\int_{\Delta\vec{r}_s} \nabla\phi_1(\vec{r})\nabla\psi_2(\vec{r},\vec{r}_d)d\vec{r}$$

$$+ \delta\Sigma_1(\omega)\int_{\Delta\vec{r}_s} \phi_1(\vec{r})\psi_1(\vec{r},\vec{r}_d)d\vec{r}$$

$$+ \delta\Sigma_2(\omega)\int_{\Delta\vec{r}_s} \phi_2(\vec{r})\psi_2(\vec{r},\vec{r}_d)d\vec{r}$$

$$- \delta\Sigma_{12}(\omega)\int_{\Delta\vec{r}_s} \phi_1(\vec{r})\psi_2(\vec{r},\vec{r}_d)d\vec{r} \ . \qquad (5.8)$$

Note that in Equation (5.8) the $\delta\Sigma_f$ term is omitted because the perturbation in the modeling calculation is due to void generation inside a water bubbler and will not introduce a perturbation in the fission cross section.

In order to evaluate δR from Equation (5.8), the following information is needed

1. The steady state fluxes before the perturbation is introduced which are given by Equation (3.56).
2. The adjoint fluxes with a detector located at $\vec{r}_d$, which are defined by Equations (3.63) and (5.1).
3. The regional flux-adjoint flux integrals for the noise source region.
4. The fluctuations of the macroscopic parameters due to the void generation inside the water bubbler.

The calculated flux-adjoint flux integrals over the noise source

volume for different detector positions are listed in Table 5.1. The fluctuation of macroscopic parameters due to various void generation fractions can be found from Table B.4 in Appendix B.

From an investigation of Table 5.1 and Table B.4, it can be seen that the two dominant terms in Equation (5.8) are

$$\delta\Sigma_{12}(\omega)\int_{\Delta\vec{r}_s}\phi_1(\vec{r})\psi_2(\vec{r},\vec{r}_d)d\vec{r}$$

and

$$\delta\Sigma_2(\omega)\int_{\Delta\vec{r}_s}\phi_2(\vec{r})\psi_2(\vec{r},\vec{r}_d)d\vec{r}\ .$$

These results can be interpreted by the following physical reasoning. For a fairly flat flux distribution region as in the central vertical stringer region of the UTR-10, the volume integrals of the product $\nabla\phi_1\nabla\phi_1$ and $\nabla\phi_2\nabla\phi_2$ are negligible. The generation of voids inside the water bubbler will reduce the water density. Thus, the voids give rise to fluctuations in the slowing down cross section and the thermal absorption cross section which are much more significant than fluctuations in the fast absorption cross section. It is seen from Figure 5.9 that the relative amplitude of ψ_1 is much less than ψ_2. Therefore the value of the fast absorption cross section $\delta\Sigma_1$, which is weighted by the volume integral of the product $\phi_1\psi_1$, is negligible compared to the contributions from $\delta\Sigma_2$, which is weighted by the volume integral of $\phi_2\psi_2$, and $\delta\Sigma_{12}$, which is weighted by the volume integral of the product $\phi_1\psi_2$.

Table 5.1. The flux-adjoint flux integral over the noise source volume for different detector positions

Detector[a] displacement from noise source[b] (cm)	$\int \nabla\phi_1 \nabla\psi_1 d\vec{r}$	$\int \nabla\phi_2 \nabla\psi_2 d\vec{r}$	$\int \phi_1\psi_1 d\vec{r}$	$\int \phi_2\psi_2 d\vec{r}$	$\int \phi_1\psi_2 d\vec{r}$
0	0.9738 E-8	0.2874 E-7	0.1449 E-4	0.8424 E-4	0.4482 E-4
2	0.1006 E-8	0.2323 E-7	0.1440 E-4	0.8344 E-4	0.4435 E-4
8	0.5154 E-8	0.6245 E-7	0.1213 E-4	0.5332 E-4	0.2745 E-4
16	0.1715 E-8	0.2919 E-7	0.9903 E-5	0.2939 E-4	0.1568 E-4
28	0.2946 E-9	0.1645 E-7	0.8372 E-5	0.1907 E-4	0.1018 E-4

[a]Detector size: 2.5 cm x 2.5 cm x 5 cm.

[b]Noise source size: 5 cm x 5 cm x 10 cm.

The calculated results for the normalized detector response function, $N\delta R$, and $NAPSD_{\delta R}$ (the normalized APSD of the detector response function) for several detector positions are given in Table 5.2.

If the perturbation introduced at $\vec{r}_s$ is a point noise source, Equation (5.6) can be rewritten as

$$\delta R(\vec{r}_s,\vec{r}_d,\omega) = [\delta\Sigma_2(\omega)\phi_2(\vec{r}_s)-\delta\Sigma_{12}(\omega)\phi_1(\vec{r}_s)]\psi_2(\vec{r}_s,\vec{r}_d) \qquad (5.9)$$

where the contributions due to δD_1, δD_2, and $\delta\Sigma_1$ are neglected based on the previous analysis.

The ratio of the detector response function δR at different detector positions, according to Equation (5.9) is

$$\frac{\delta R(\vec{r}_s,\vec{r}_{d1},\omega)}{\delta R(\vec{r}_s,\vec{r}_{d2},\omega)} = \frac{\psi_2(\vec{r}_s,\vec{r}_{d1})}{\psi_2(\vec{r}_s,\vec{r}_{d2})} \qquad (5.10)$$

which is the same result as that shown in Equation (5.4).

The normalized detector response functions, $N\delta R$, due to a 5 cm x 5 cm x 10 cm noise source and also due to a point source are compared in Figure 5.11. The corresponding plots for the normalized APSD of the detector response function, $NAPSD_{\delta R}$, are shown in Figure 5.12. It can be seen from Figures 5.11 and 5.12 that $N\delta R$ and the $NAPSD_{\delta R}$ for a finite volume noise source are larger than those for a point source located at the center of the central vertical stringer region.

Table 5.2. The $NAPSD_{\delta R}$'s and $N\delta R$'s as function of the separation between the detector and the noise source

Detector[a] displacement from noise source[b] (cm)	$N\delta R = \frac{\delta R(\vec{r},\omega)}{\delta R(0,\omega)}$	$NAPSD_{\delta R} = \frac{APSD_{\delta R}(\vec{r},\omega)}{APSD_{\delta R}(0,\omega)}$
0	1	1
2	0.980	0.970
8	0.528	0.278
16	0.353	0.125
28	0.229	0.552

[a]Detector size: 2.5 cm x 2.5 cm x 5 cm.

[b]Noise source size: 5 cm x 5 cm x 10 cm.

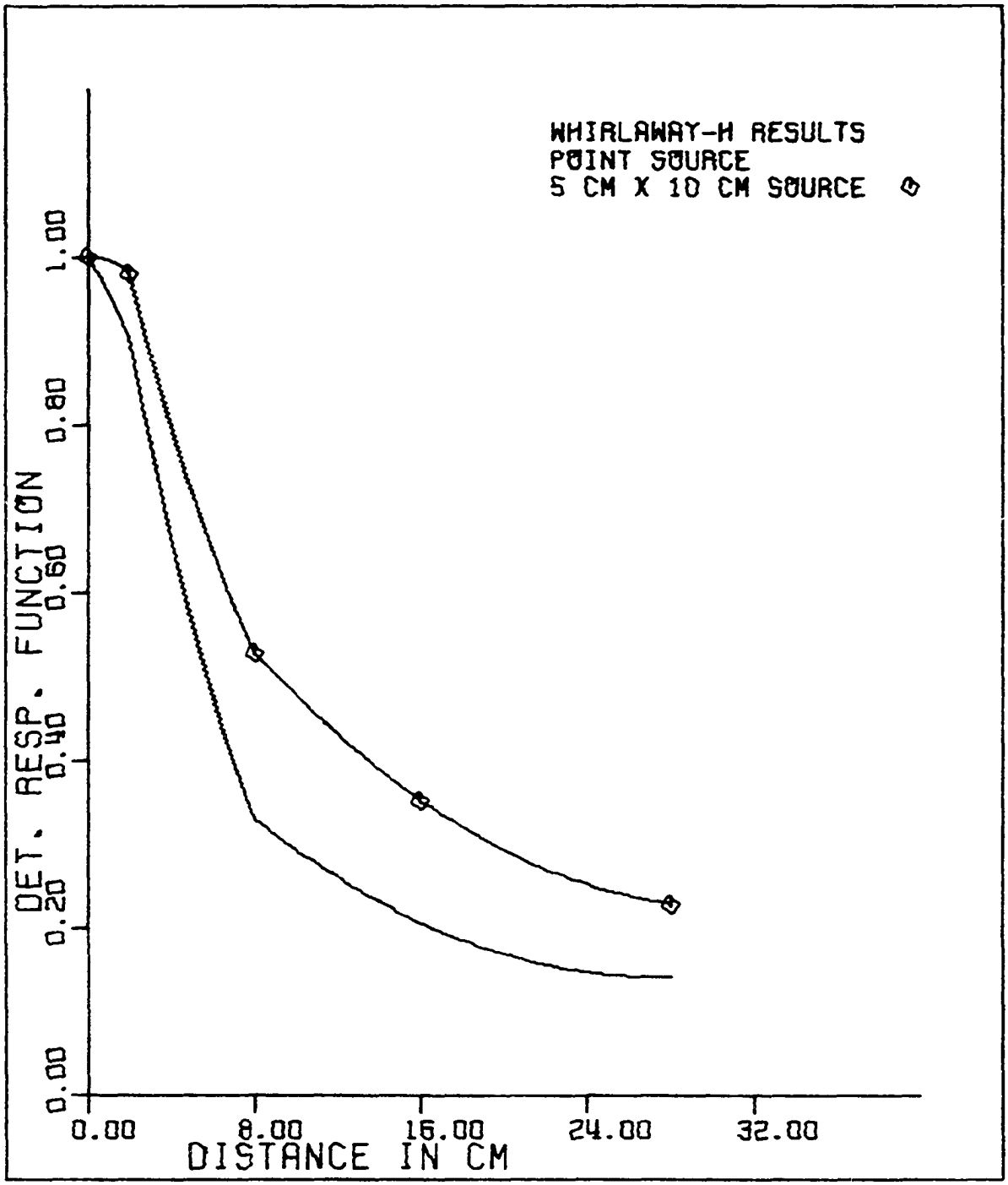

Figure 5.11. δR's for different detector displacement from the noise source and for different noise source volume

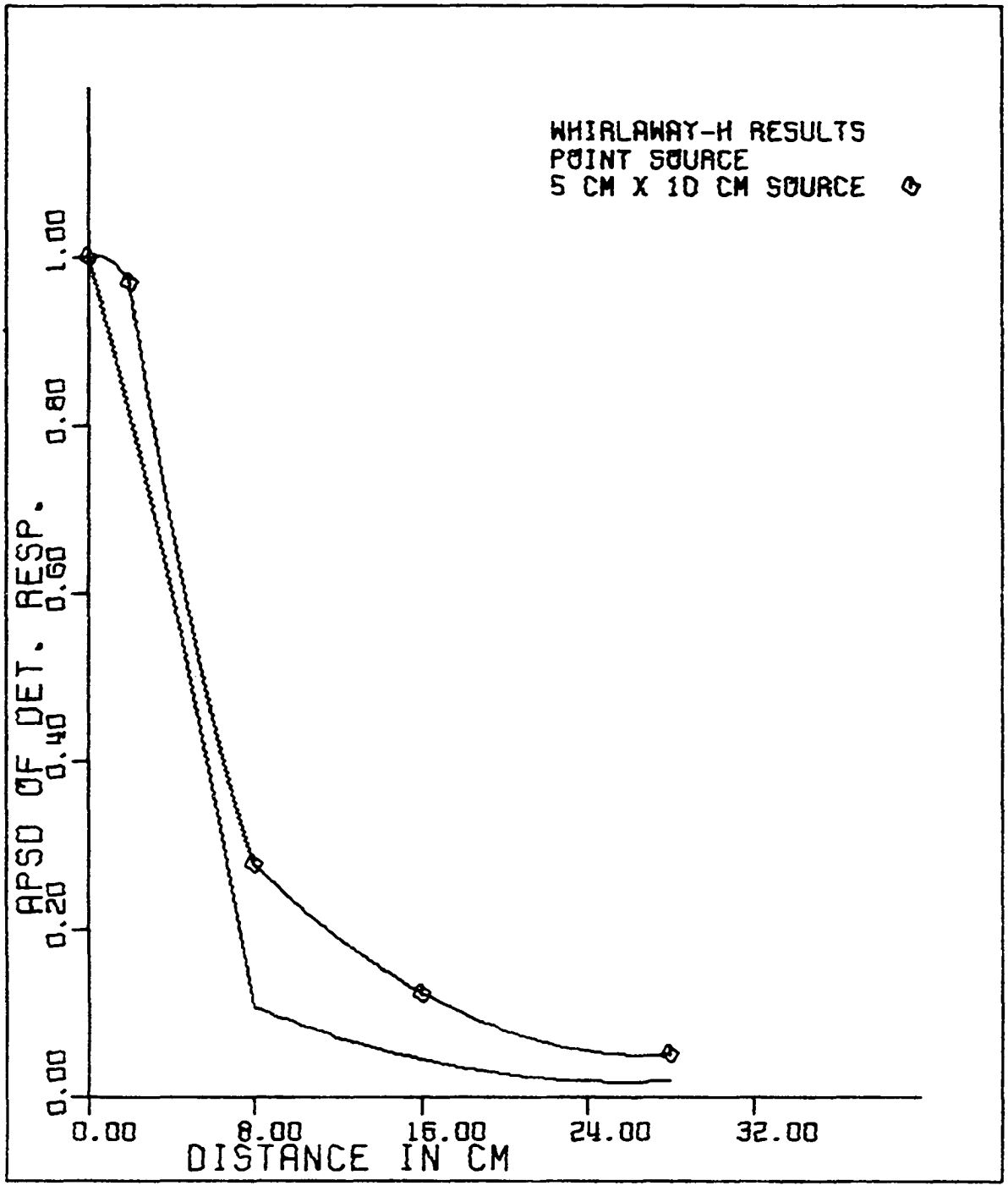

Figure 5.12. $NAPSD_{\delta R}$'s for different detector displacement from the noise source and for different noise source volume

VI. EXPERIMENTAL APPARATUS AND PROCEDURES

Experimental measurements were carried out on the UTR-10 reactor to find the neutron detector response with respect to void generation inside a water bubbler placed inside the central vertical stringer region. The experiment was designed to follow as close as possible the configuration used in the WHIRLAWAY-H three-dimensional modeling calculation described in Chapter IV and Chapter V. A BF_3 detector and a neutron noise detection system were used to analyze the neutron noise signal generated by the water bubbler. Detector signals were recorded on magnetic tape. The playback signals from the magnetic tapes were then analyzed using a microcomputer based data acquisition system to find the auto-power spectral densities of the detector response function for different detector positions. The purpose of the measurements was to verify the validity of the detector response model described in Chapter III for the frequency range of interest, i.e., $0.1 \text{ Hz} << \omega << 10 \text{ Hz}$.

A. Experimental Apparatus

1. The UTR-10 nuclear reactor

The UTR-10 [51, 53] is a 10 KW heterogeneous, light water moderated and cooled, graphite reflected, nuclear reactor. A longitudinal section view of this reactor is shown in Figure 6.1.

The reactor core consists of a 44 in x 56 in (112 cm x 142 cm) stack of graphite 48 in (122 cm) high, in which two rows of fuel

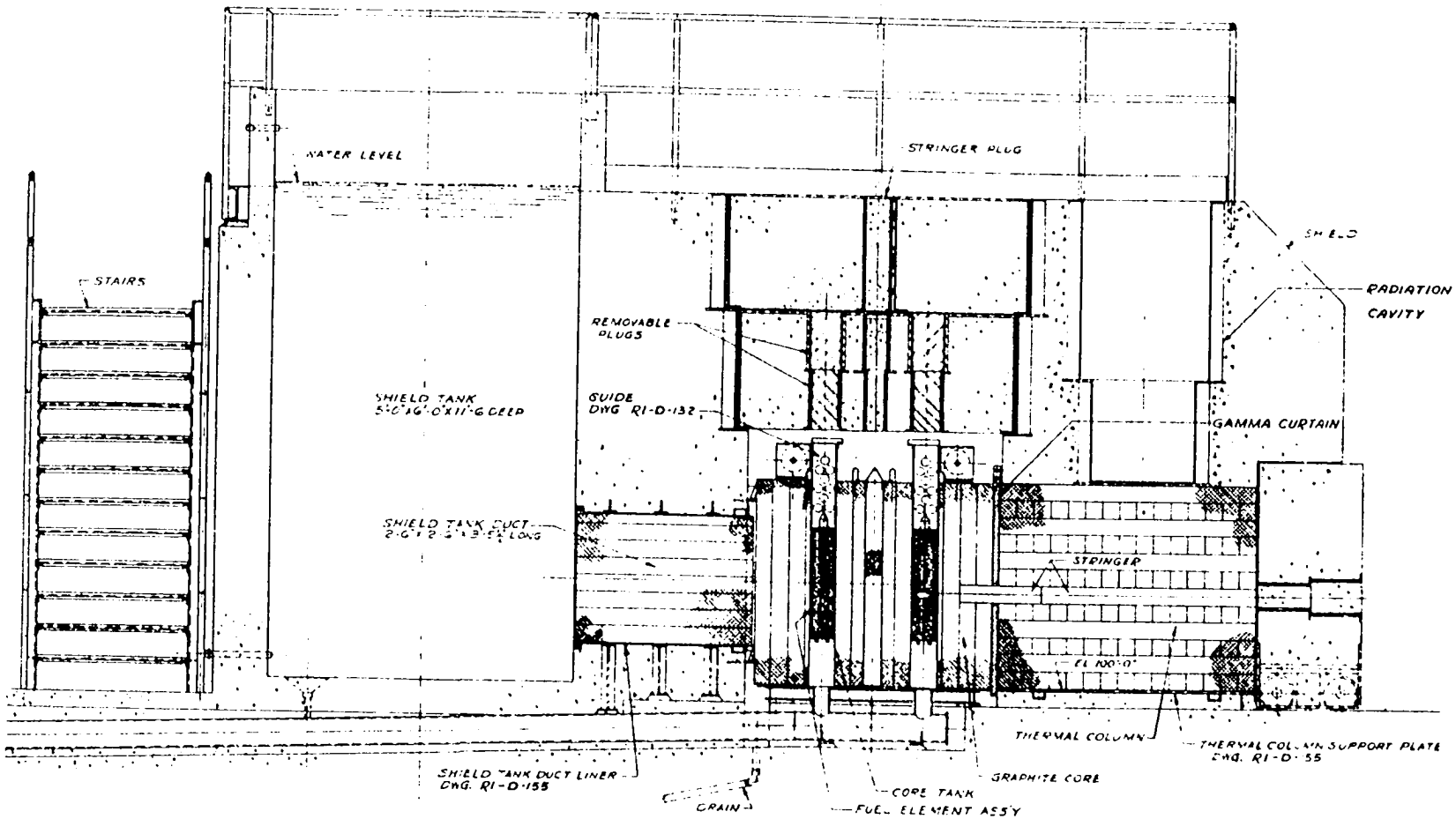

Figure 6.1. The longitudinal cross section view of the UTR-10 reactor

elements are embedded. The fuel elements are positioned within two parallel core tanks spaced 24 in (61 cm) on center. This arrangement provides for an 'external' graphite reflector of 1 foot (30.48 cm) in thickness in each lateral and vertical dimension and an 'internal' reflector of 18 inches (45.7 cm) between the two core tanks. Five graphite stringers are provided in the internal reflector region between the core tanks. One of the stringers is $3\frac{3}{4}$" x $3\frac{3}{4}$" x 48" (9.5 cm x 9.5 cm x 122 cm) and is located at the center of the core. The other four stringers are $1\frac{13}{16}$" x $1\frac{13}{16}$" x 48" (4.6 cm x 4.6 cm x 122 cm) and are grouped around the central stringer. Access to the stringers is provided through ports in the top shield closures as shown in Figure 6.1.

The central vertical stringer (CVS) was removed during the experimental measurements so that the water bubbler, BF_3 detector and some other experimental apparatus could be inserted in the CVS region which has a flux level of approximately 10^{11} neutrons/cm^2-sec. at 10 kW [52].

2. The void generation system

Figure 6.2 shows a block diagram for the void generation system used in this experiment. A nitrogen gas bottle (160 ft^3, 4.25 liters) manufactured by Cook Manufacturing Company was placed on the top of the reactor concrete shield to supply the nitrogen gas. Nitrogen gas was used because of its low cross section for neutron-induced reactions and long half life (5500 year) of its activation

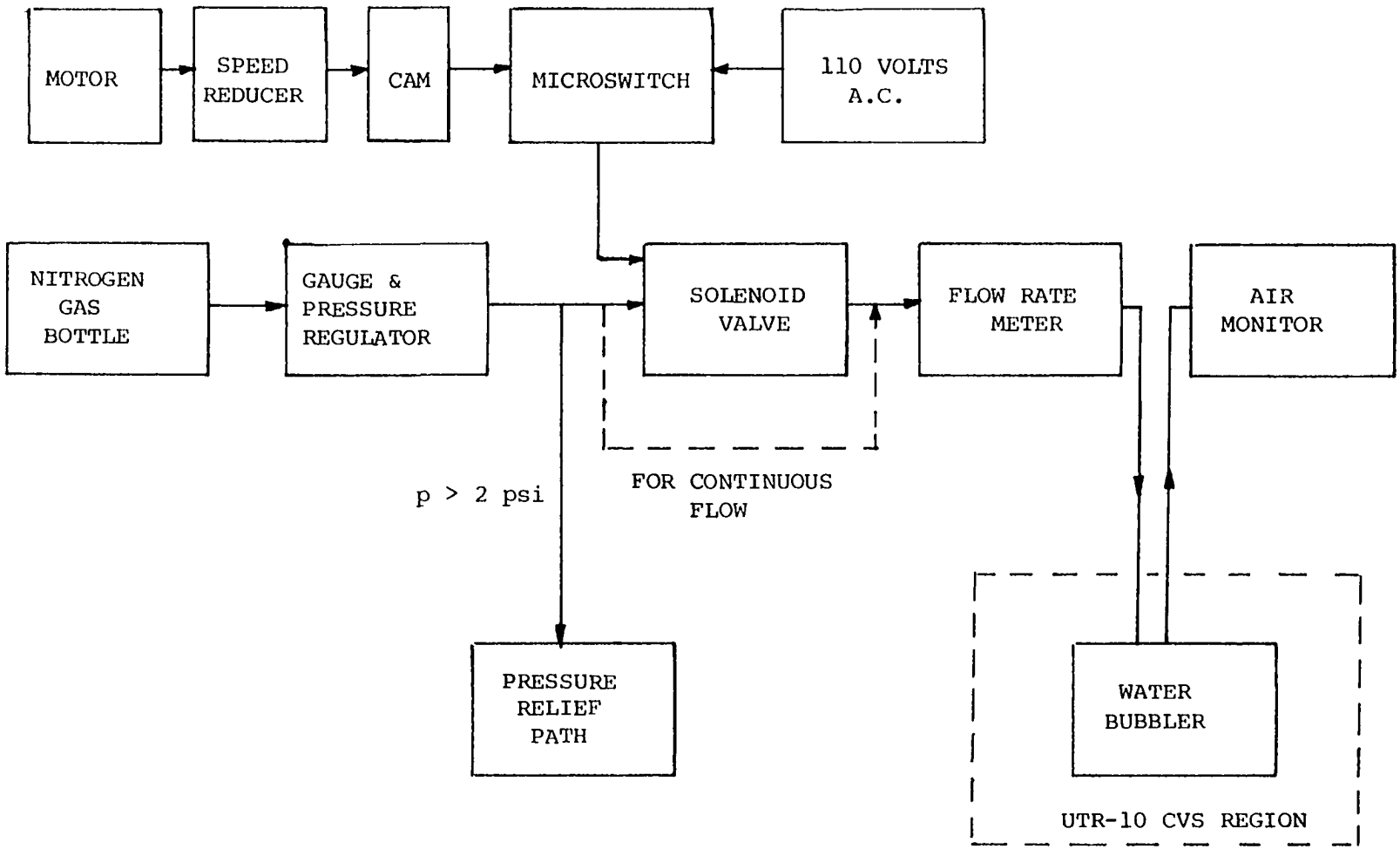

Figure 6.2. Block diagram of the void generation system

product (carbon-14). The flow rate and the line pressure of the nitrogen gas were adjusted using the pressure gauge and the pressure regulator on the gas bottle and monitored by a flow rate meter (Fl200, Roger Gilment Instruments, Inc.) to achieve the desired values. The flow rate meter was calibrated using a water displacement method. The results are shown in Table 6.1 and Figure 6.3.

The water bubbler which was made of plexiglass was 12 cm long and 5 cm in diameter. The thickness of the plexiglass was chosen to be 0.33 cm which was found to be adequate to withstand the operating pressure ($\sim$ 2 psi) of the water bubbler. One plexiglass tube (0.16 cm wall thickness, 0.32 cm ID, and 11.5 cm long) provided a path for the inlet nitrogen gas into the bottom of the water bubbler and one plexiglass tube with a larger diameter (0.16 cm wall, 0.64 cm ID and 3 cm long) served as the path for exhaust nitrogen gas.

If continuous void generation was desired, the nitrogen gas was fed directly to the flow rate meter from the gauge and pressure regulator. If it was desired to generate pulses of bubbles at a specific frequency, a solenoid valve (type 002-4El, Humphrey Products) was then connected between the gauge and pressure reducer, and the flow rate meter. This solenoid valve was opened and closed by means of an A.C. motor (type NYO-34, Bodine Electrical Co.) driving a 20 to 1 speed reducer (type 04-5, PIC Design Corp.) unit turning a cam which closed a microswitch, supplying 110 volt power to the valve, once per revolution. Using a strobe light (Strobotac, type 304,

Table 6.1. Calibration data for the flow rate meter (F1200, GSI)[a]

Ball Position (%)	Flow Rate (ml/min)
10	50
20	220
30	440
40	670
50	920
60	1170
70	1430
80	1680
90	1980
100	2200

[a]Water displacement method was used in the calibration. The volume of the water to be displaced was 253.3 milliliter. The operating nitrogen gas pressure was 2 psi.

General Cambridge), the rpm of the motor was found to be 1800 and the angular velocity at the output of the speed reducer was found to be 90 rpm. Thus, the pulsing frequency of the bubbles would be 1.5 Hz if the pulsing mode is used.

Tygon tubing (0.16 cm wall, 0.64 cm ID) was used for the inlet nitrogen gas path connecting each component shown in Figure 6.2. Tygon tubing with a larger diameter (0.16 cm wall, 0.96 cm ID) provided an exhaust line for nitrogen gas from the water bubbler and

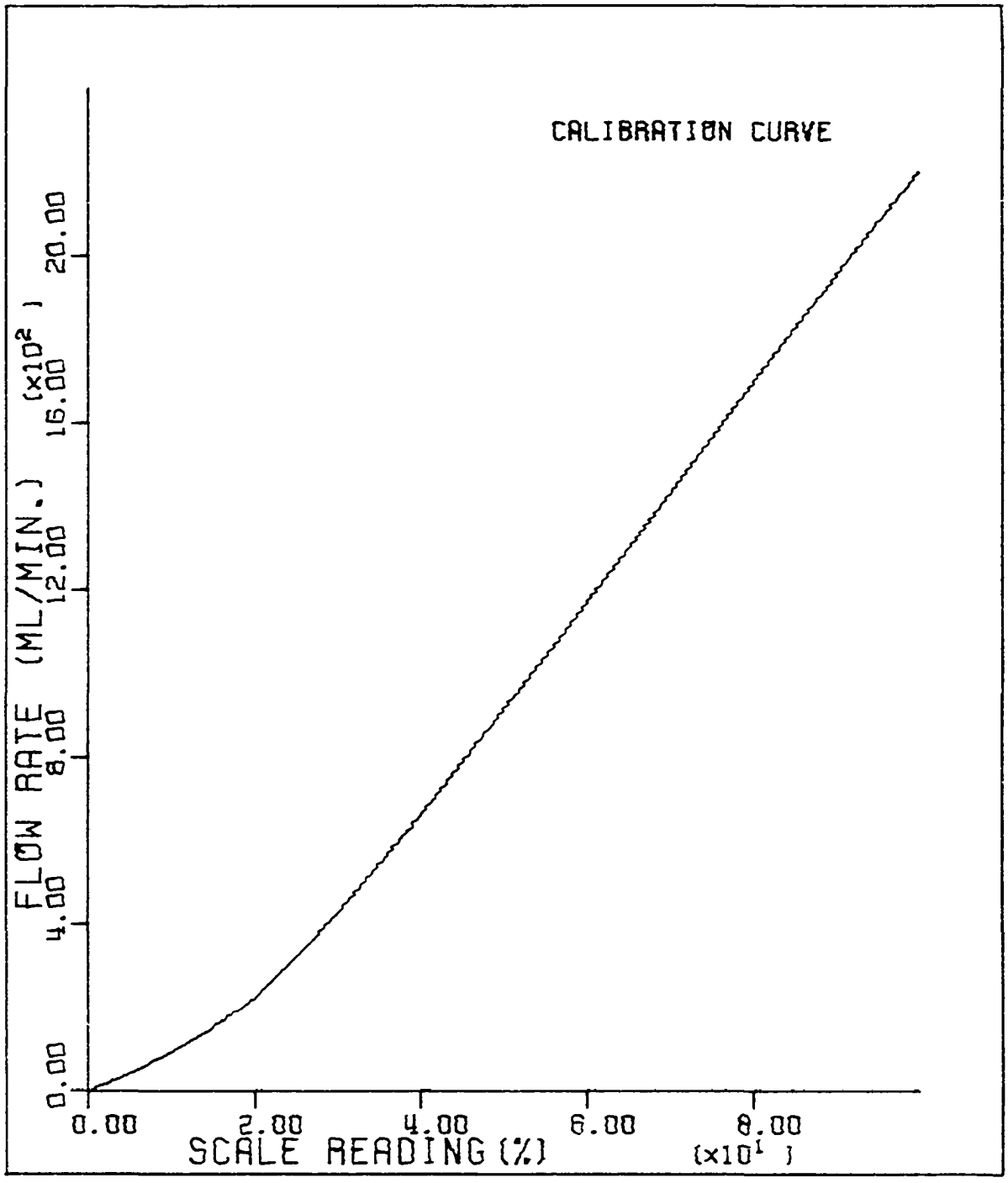

Figure 6.3. The flow rate calibration curve for the RGI F-1200 flow rate meter

for the pressure relief line for the pressure relief path shown in Figure 6.2. The water level in the pressure relief path was chosen so that any operating pressure greater than 2 psi, at 60% steady state flow rate (1170 ml/min), would result in the discharge of gas through the relief path. The exhausted nitrogen gas from the water bubbler was monitored continuously by an air monitor (Model AMS-2, Eberline Instrument Co.) during the experiment to detect any induced radioactivity.

3. The neutron noise detection system

The void generation inside the water bubbler introduced core parametric fluctuations which in turn produced fluctuations of the neutron flux inside the UTR-10 reactor core region. A block diagram of the neutron noise detection system is shown in Figure 6.4.

A type G-10-2A BF_3 neutron detector manufactured by N. Wood Counter Lab., Inc. was inserted beside the water bubbler inside the central vertical stringer region of the reactor. The BF_3 detector, which has a diameter of 2.5 cm and a length of 5 cm, was used in the current mode and operated in the ion chamber region. The operating voltage was chosen to be -90 volts and was supplied by a battery. The current output of the BF_3 detector was fed into a preamplifier, which has a 10^8 volts/amp. conversion gain, and converted into a voltage output. The voltage output from the preamplifier was then amplified before recording on the magnetic tape. A bias control was provided on the amplifier to remove any d.c. component in the noise

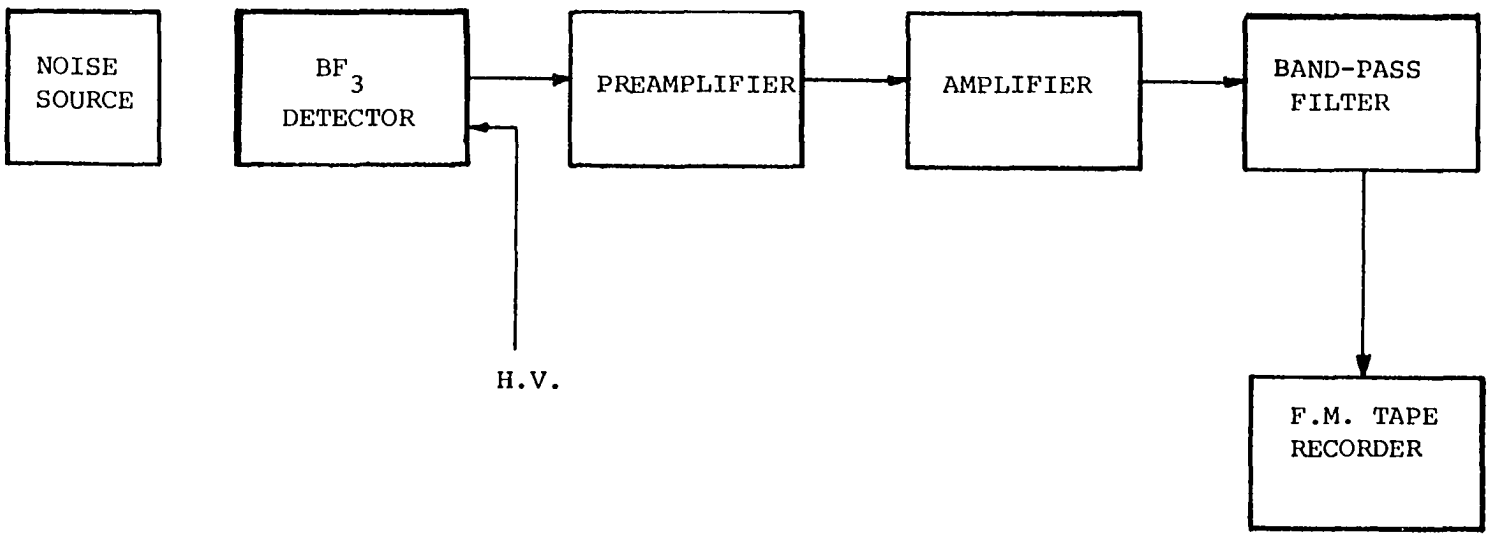

Figure 6.4. Block diagram of the neutron noise detection system

signal. The d.c. battery supply, the preamplifier and the amplifier were manufactured by the Ames Laboratory. The preamplifier has a switch for 10^6, 10^7, and 10^8 volts/amp conversion gain selections. Two stages of amplification were used in the experiment. The calibration of the gain for the amplifiers is given in Table 6.2.

The output noise signal from the amplifier was passed through a bandpass filter (high-pass at 0.1 Hz and low-pass at 10 Hz) and then recorded on Scotch Low Noise tape (type 217) using a PI-6200 FM tape recorder (Precision Instrument Inc.) for later playback and data analysis.

4. Experimental arrangement in the reactor

In order to keep the experiment performed in the graphite environment as close as possible to that used in the modeling calculations, a special graphite stringer was constructed to house the water bubbler, the BF_3 detector, the tygon tubings, the high voltage detector cable and the leakage detector. A detailed view of the graphite stringer construction is shown in Figure 6.5.

The dimension of the graphite stringer was 9.6 cm x 9.6 cm ($3\frac{3}{4}$" x $3\frac{3}{4}$") in cross section and 60.96 cm (24 in) in height. It can be seen from Figure 6.5 that the water bubbler was put into a hole (5.72 cm in diameter and 12.7 cm in height) inside the stringer, so that the water bubbler would assume a fixed position during the entire experiment. A 2.85 cm x 2.85 cm x 60.96 cm ($1\frac{1}{8}$" x $1\frac{1}{8}$" x 24") slot provided a passage for the BF_3 detector and the high voltage cables

Table 6.2. The calibration of amplifier gains

Dial setting	Gain (E out/E in)	
	Channel 1	Channel 3
0	58.0	45.0
0.1	42.6	31.7
0.2	34.6	26.0
0.3	29.5	22.4
0.4	26.2	20.4
0.5	23.9	18.4
0.6	22.0	17.2
0.7	20.6	16.2
0.8	19.3	15.4
0.9	18.4	14.7
1.0	17.4	14.1
1.5	14.5	12.0
2.0	12.7	10.7
2.5	11.4	9.7
3.0	10.2	8.9
3.5	9.4	8.1
4.0	8.5	7.4
5.0	7.0	6.2
6.0	5.76	5.0
7.0	4.5	3.9
8.0	3.3	2.8
9.0	2.2	1.76
10.0	1.06	0.75

Figure 6.5. The graphite stringer containing the water bubbler, BF_3 detector, tygon tubing, high voltage cable and the leakage detector

so that the detector could be moved vertically during the experiment to several predetermined detector positions. The passage of the tygon tubing and the leakage detector cables was provided for by a 1.9 cm x 1.9 cm x 60.96 cm ($\frac{3}{4}$" x $\frac{3}{4}$" x 24") slot on the opposite side of the graphite block. The leakage detector consisted of a 9.6 cm x 9.6 cm x 0.16 cm ($3\frac{3}{4}$" x $3\frac{3}{4}$" x $\frac{1}{16}$") plexiglass plate with two aluminum bolt terminals on it. The resistance between the bolts was monitored at the reactor console by connecting cables to the aluminum bolt terminals and to a multimeter set in the resistance mode. The resistance between the two terminals on the leakage detector is infinite under normal condition (no water present) and will be very small or near zero whenever there is water leaking out of the water bubbler.

During the experiment, the central vertical stringer shown in Figure 6.1 was removed and a half stringer 9.6 cm x 9.6 cm ($3\frac{3}{4}$" x $3\frac{3}{4}$") in cross section and 60.96 cm (24") in height was inserted. The special graphite stringer shown in Figure 6.5 was then put on the top of the half stringer. The entire experimental setup is shown in Figure 6.6.

B. The Data Acquisition System

The data acquisition system is shown in Figure 6.7 and the block diagram for the system is shown in Figure 6.8. The noise signals recorded on magnetic tape were played back from the FM tape recorder.

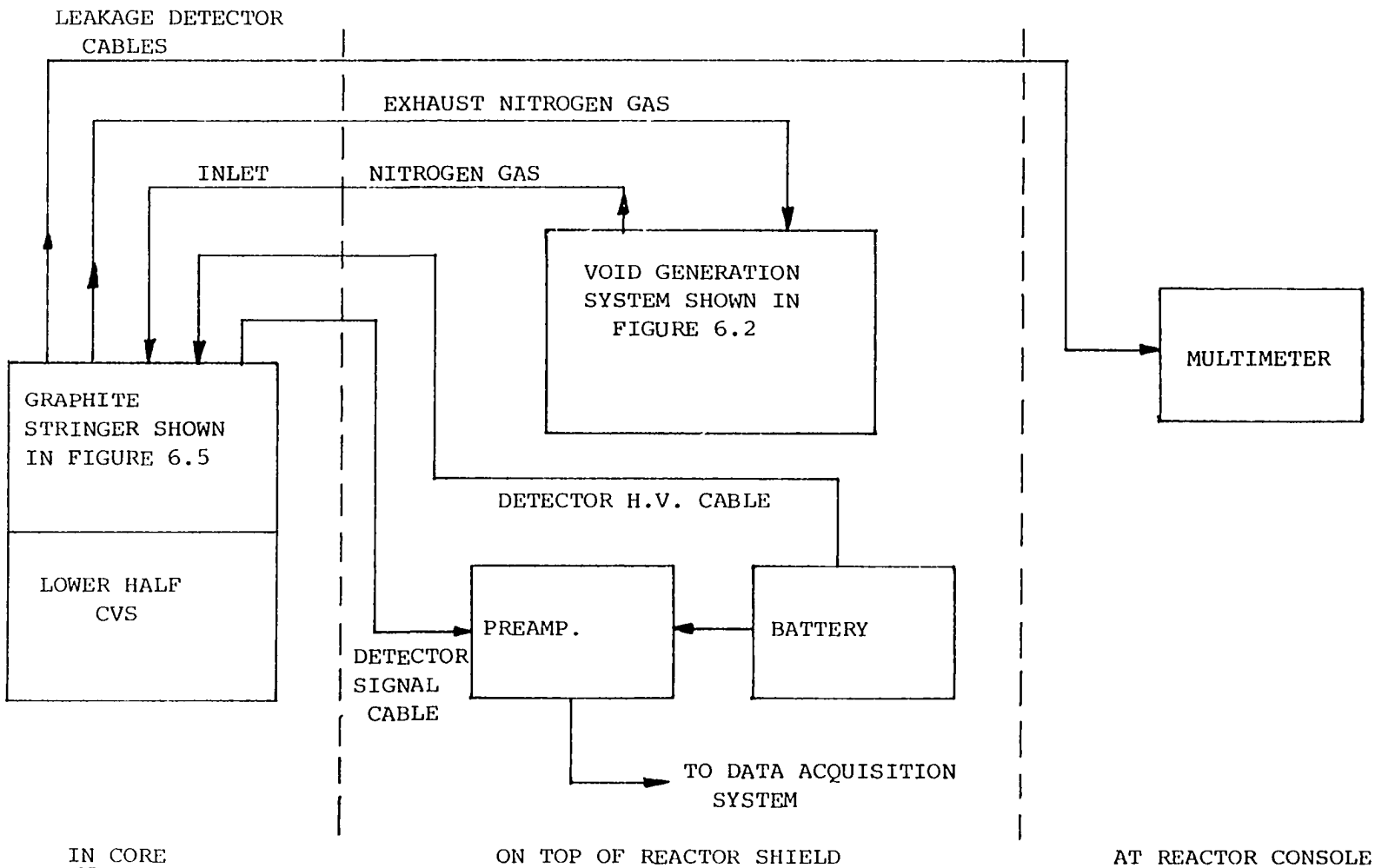

Figure 6.6. The experimental setup in the UTR-10

Figure 6.7. The data acquisition system

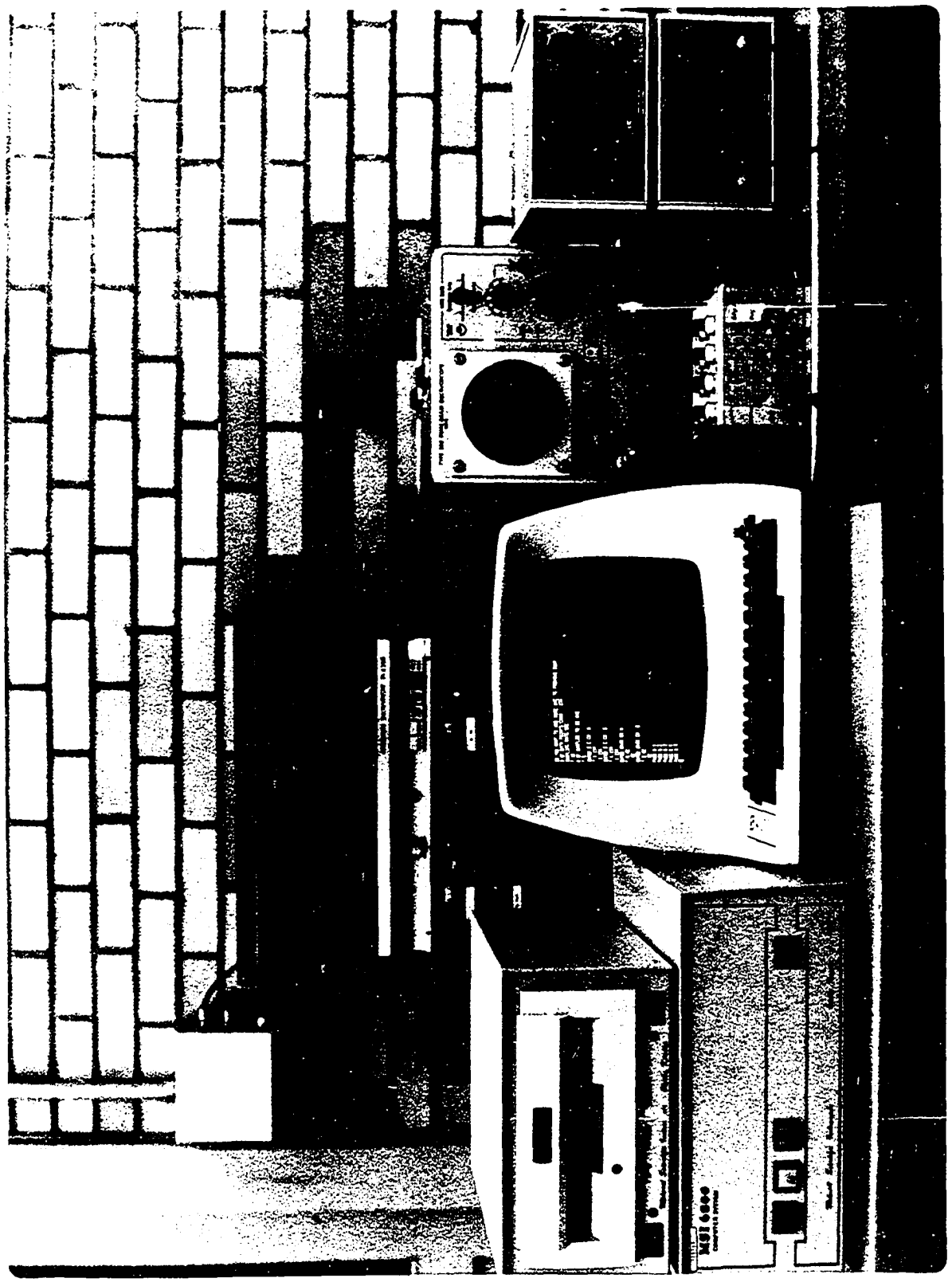

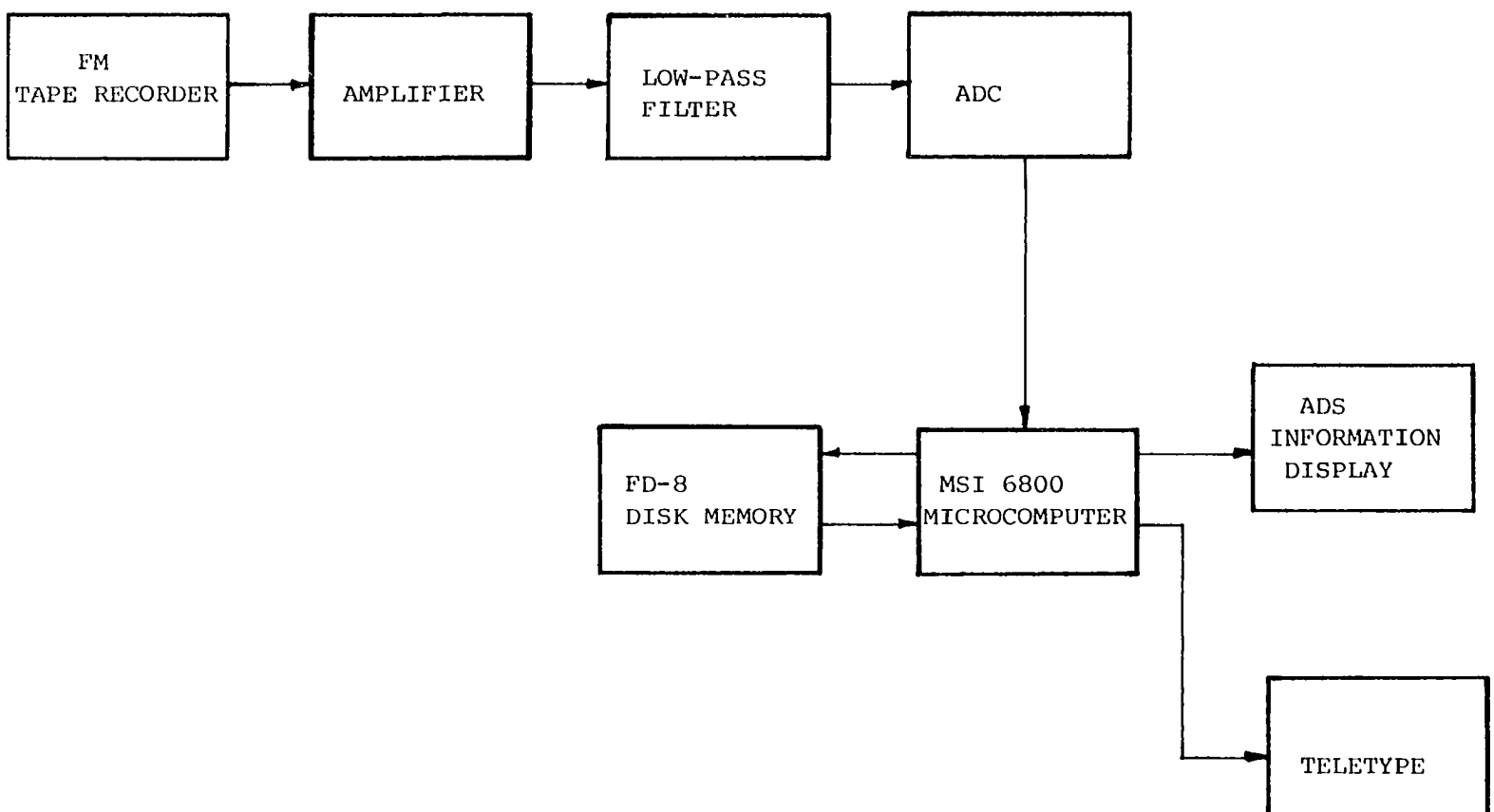

Figure 6.8. Block diagram of the data acquisition system

The gain and the bias control on the amplifier were adjusted such that

1. most of the d.c. component in the noise signal was removed, and
2. the amplitude of the signal at the output of the amplifier was chosen between 0 and 10 volts which was the analog signal voltage range of the analog to digital converter (ADC) used in the data acquisition system.

A potential error which arises in analog to digital conversion is the so-called aliasing problem. For an analog to digital converter sampling at an interval h, the Nyquist frequency is defined as

$$f_c = \frac{1}{2h} = \frac{1}{2} f_s \tag{6.1}$$

where f_s is the sampling frequency of the ADC [5].

If the Nyquist frequency, f_c, is lower than the maximum frequency component in the noise signal, the frequency component higher than f_c will fold back in the frequency spectrum between 0 to f_c and thus produce aliasing.

It is known from the sampling theorem [5, 8] that the sampling frequency, f_s, has to be at least twice the maximum frequency component in the noise signal to avoid aliasing. If the maximum frequency in the signal is unknown, it is a common practice to filter the data prior to sampling so that information above the filter cutoff frequency, f_d, is no longer contained in the filtered data.

A good choice for the sampling frequency, f_s, is between 2 f_d to 2.5 f_d in spectral density analysis as recommended by Bendat [5].

Two filters [Krohn-Hite Corp., Model 3321] were used in the data acquisition system. One filter was operated in the high-pass mode with cut-off frequency of 0.1 Hz so that any residual d.c. component was removed from the signal. The other filter was used in the low-pass mode with the cut-off frequency equal to 10 or 4 Hz, which is the maximum frequency of interest in this research.

A 8-bit ADC (MP-21, Burr Brown) was used to digitize the noise signal. The analog to digital conversion time is about 30 μs to 40 μs. The sampling frequency, f_s, was chosen to be 2.5 f_d.

The digitized data were then supplied to the microcomputer (MSI-6800, Midwest Scientific Instruments) which was connected to a disk memory (FD-8, Midwest Scientific Instruments) having 32 K bites of storage. The auto-power spectral densities (APSD) for the signal were then calculated using a Fast Fourier Transform (FFT) program written in BASIC language. The output data from the FFT were then either viewed from the screen of the ADS display unit (Information Display) or printed on the teletype.

1. The FFT program

The FFT program, written in BASIC, can be used to calculate the auto-power spectral density, the cross power spectral density, the coherence function and the transfer function between two input channels. In this research only the auto-power spectral density

(APSD) of the detector response function for different detector position is of interest. Therefore only one channel of the digitized data from the magnetic tape was used.

The flow diagram of the FFT program is shown in Figure 6.9. This program allows two channels of input data and 512 data points (256 data points per channel). The gain of the amplifier and/or the d.c. level of the noise signal were also used as input to normalize the APSD for different experimental conditions if it is required by the analysis.

The raw APSD was calculated from the transformed data using the expression [5]

$$\tilde{G}_k = \frac{2h}{N} |X_k|^2 \tag{6.1}$$

where

$$X_k = \sum_{n=1}^{N-1} \chi_n \exp[-j \frac{2\pi kn}{N}] \tag{6.2}$$

$= $ discrete Fourier Transform at frequency point k

N = number of data points

h = the sampling interval

$\chi_n = \chi(nh)$

$= $ value of $\chi(t)$ and t is equal to nh

According to Bendat [5], the standard error, ε_r, is estimated as

$$\varepsilon_r = \frac{1}{(B_e T)^{1/2}} \tag{6.3}$$

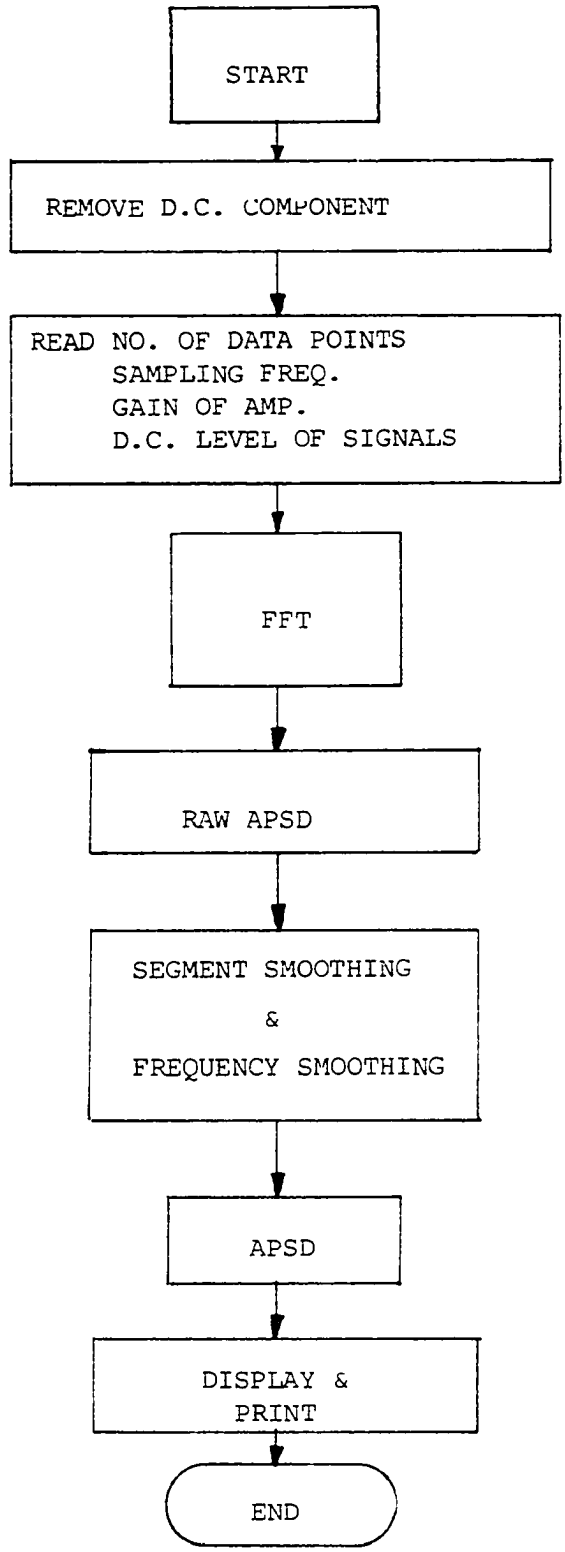

Figure 6.9. Flow diagram of the FFT program

where

B_e = the resolution bandwidth of the APSD

T = the record length of the data.

Equation (6.3) implies that the standard error of the raw APSD estimate is 100% since B_e is equal to the reciprocal of T.

Two different smoothing techniques are used to reduce ε_r, namely, frequency smoothing in which several neighboring frequency points are averaged and segment smoothing in which the results from several separate time records are averaged. For ℓ frequency points averaging and q separate time records, the resultant standard error is given, according to Bendat [5], by

$$\varepsilon_r = \frac{1}{(\ell q)^{1/2}} \quad . \tag{6.4}$$

The number of points used for frequency smoothing, ℓ, and the number of segment averaged, q, will be discussed in Chapter VII.

2. The test of the FFT program

The FFT program was tested by transforming a 0-15 Hz Gaussian white noise generated from a noise generator (Model 3722A, Hewlett Packard) and by measuring the magnitude and phase of a low pass filter. A block diagram of the test setup is shown in Figure 6.10.

The calculated APSD, using the FFT program, for Channel A is shown in Figure 6.11. It can be seen from Figure 6.11 that the APSD is constant over the frequency range from 0 Hz to 10 Hz. This was what was expected since the signal from Channel A was the 0-15 Hz

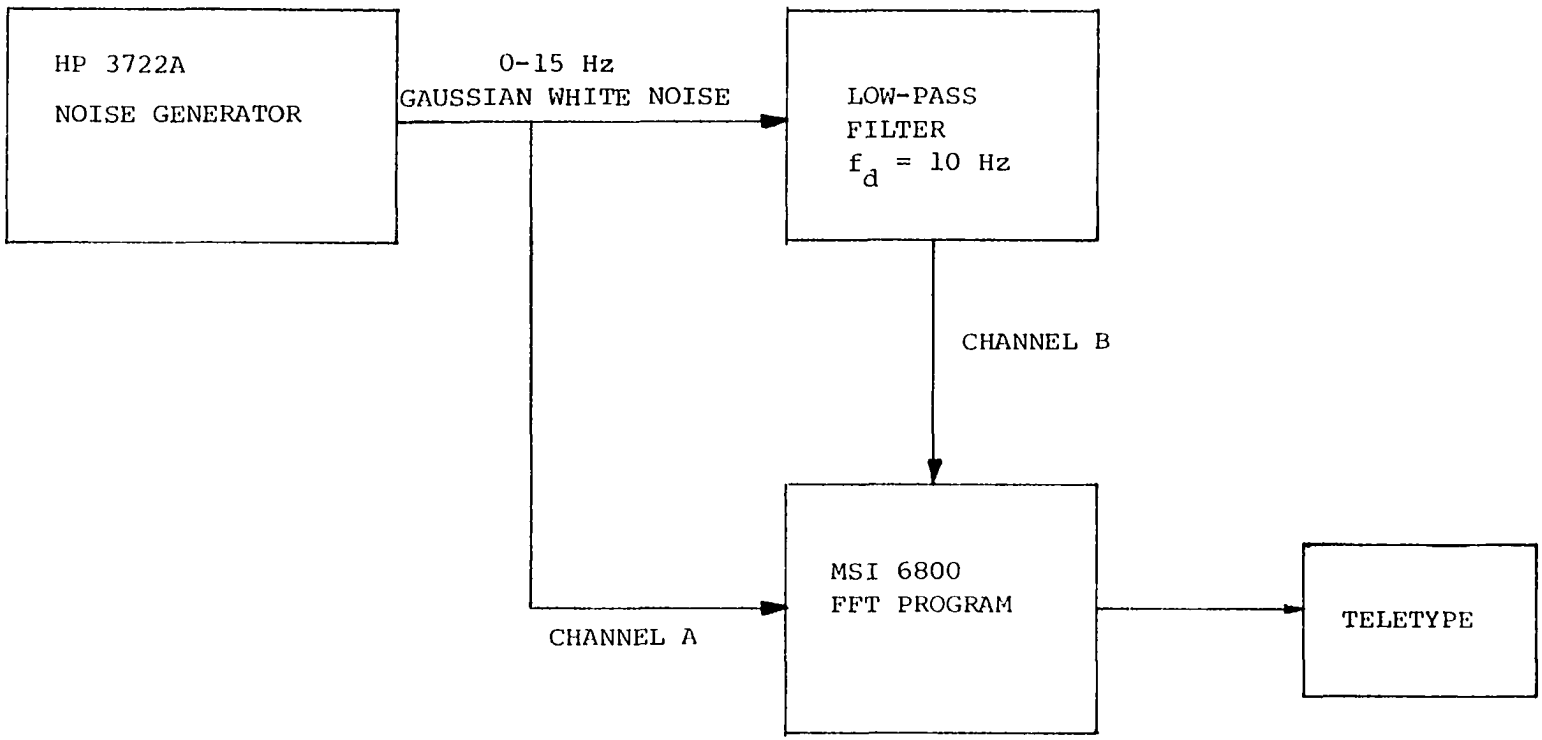

Figure 6.10. Block diagram of the setup for testing the FFT program

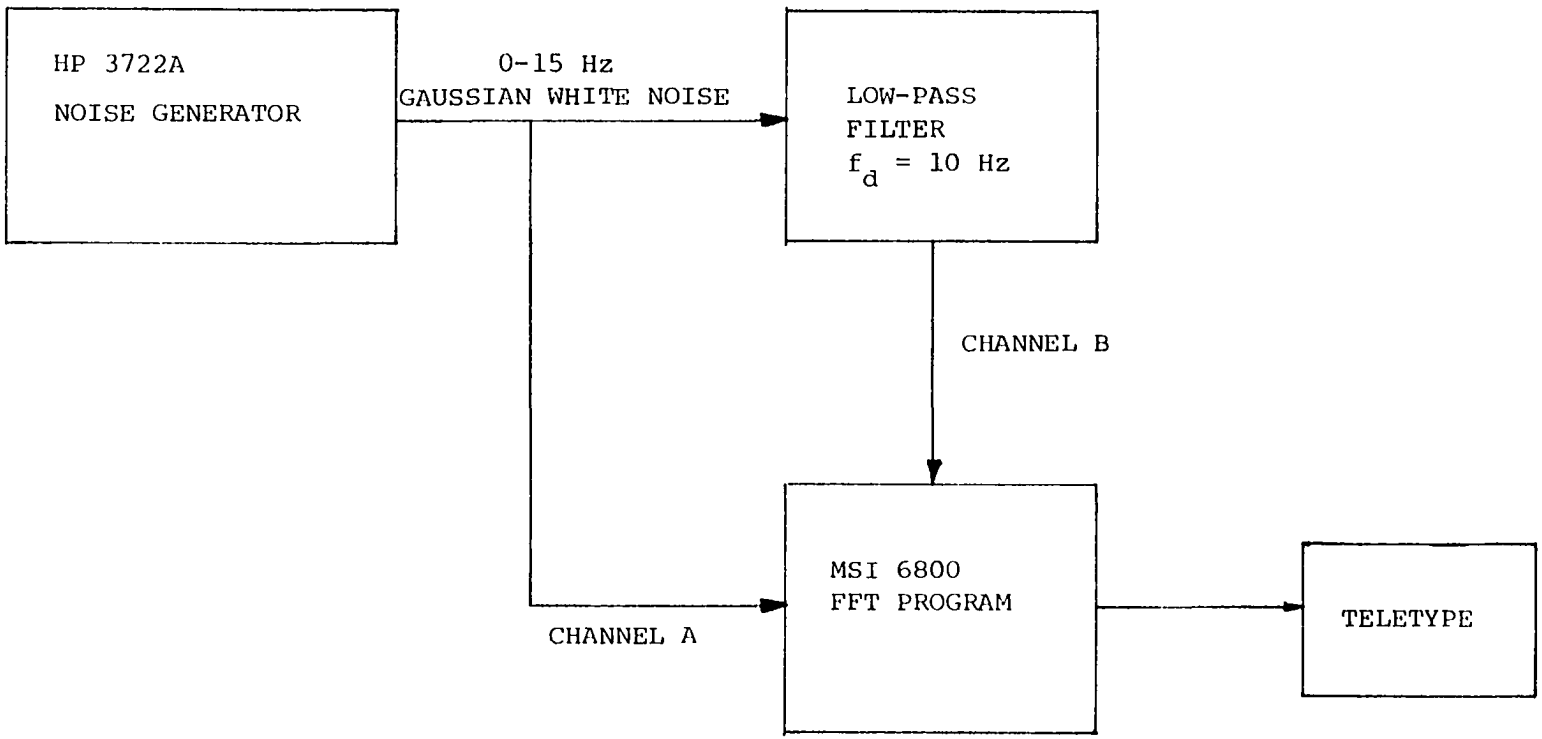

Figure 6.10. Block diagram of the setup for testing the FFT program

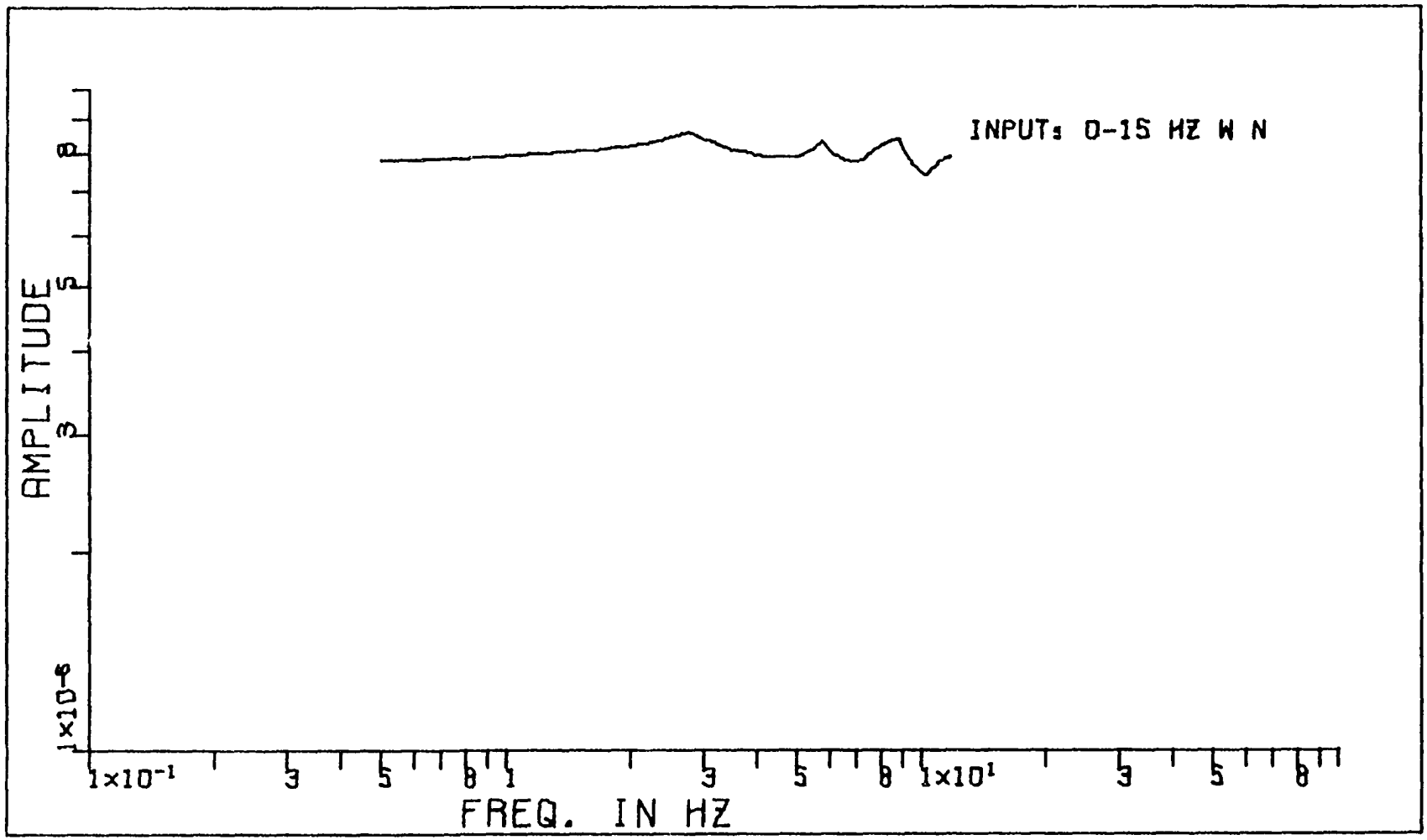

Figure 6.11. The calculated APSD for a white noise input using the FFT program

Gaussian white noise. The calculated transfer function between channel A and channel B should be the same as the transfer function of the low-pass filter. The magnitude and phase plot of the calculated transfer function are shown in Figure 6.12. These results agree well with those given in the manual for the low-pass filter [53].

The FFT program was also tested using a sine wave input from a signal generator (Model 111, Wavetek). The frequency of the signal generator was calibrated and checked by an electronic counter (Model 3735, Hewlett Packard) before testing. It was found that the calculated APSD, using the FFT program, provided peaks at the same frequencies as the input sine wave signal generated by the signal generator.

Based on these tests, it was concluded that the analysis system was working properly.

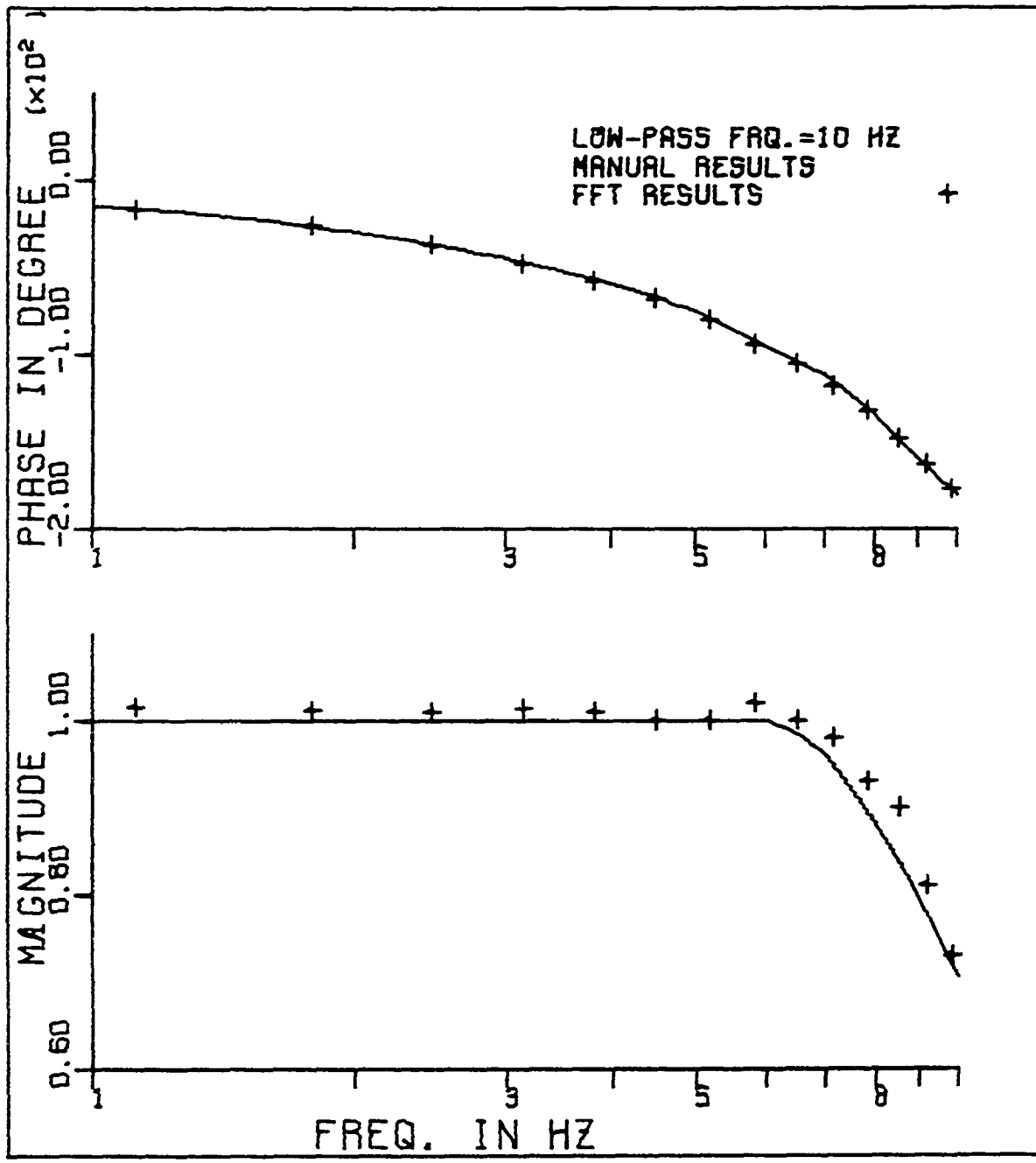

Figure 6.12. The transfer function of the low-pass filter obtained from the FFT program

VII. EXPERIMENTAL RESULTS AND ANALYSIS

As pointed out in the previous chapters, the purpose of this research is to carry out an experimental verification of the properties of the detector adjoint function and the detector response model described in Chapter III. To meet these objectives, a series of measurements were carried out using the UTR-10 reactor and the experimental system described in Chapter VI. These measurements yielded the APSD of the neutron detector response ($APSD_{\delta R}$) as a function of distance from a void perturbation source consisting of a water bubbler. The measured $APSD_{\delta R}$'s could then be compared with the predicted values obtained using the WHIRLAWAY-H code modeling calculations.

Prior to performing the experiment, several preliminary steps had to be completed. A safety analysis of the proposed experiment was prepared and submitted to the reactor safety committee for approval. The flow rate of the flow rate meter was calibrated, the proper operating voltage of the BF_3 detector was chosen, the conversion gain of the preamplifier was calibrated using a current source, the gain of the amplifiers was checked and the Fast Fourier Transform (FFT) program was tested. The experimental conditions for each measurement such as the steady state flow rate and the pressure of the nitrogen gas, the reactor inlet coolant temperature, the control rod position, etc., were kept constant for each measurement.

A. Auto-power Spectral Densities

1. Continuous void generation versus pulsing at a fixed frequency

Experimental measurements were carried out for the following void conditions

a. No void generation inside the water bubbler.

b. Continuous 20% void generation which corresponds to 60% of the full scale reading on the flow rate meter (i.e. 1170 ml/min).

c. Bursts of bubbles produced at 1.5 Hz with a steady state flow rate at a meter reading of 60% before the pulsing was introduced. This is referred to as the pulsing mode.

The calculated APSD's of the noise signal for these three cases were plotted on the IBM 370 computer system using a simplotter routine. Typical results obtained from these measurements are shown in Figures 7.1, 7.2 and 7.3. The calculated APSD's all have the same FFT program inputs:

N = number of data points in the record

= 256

f_s = sampling frequency

= 25.6 Hz

f_d = cut-off frequency of the low-pass filter

= 10 Hz

q = number of segment averages

= 36

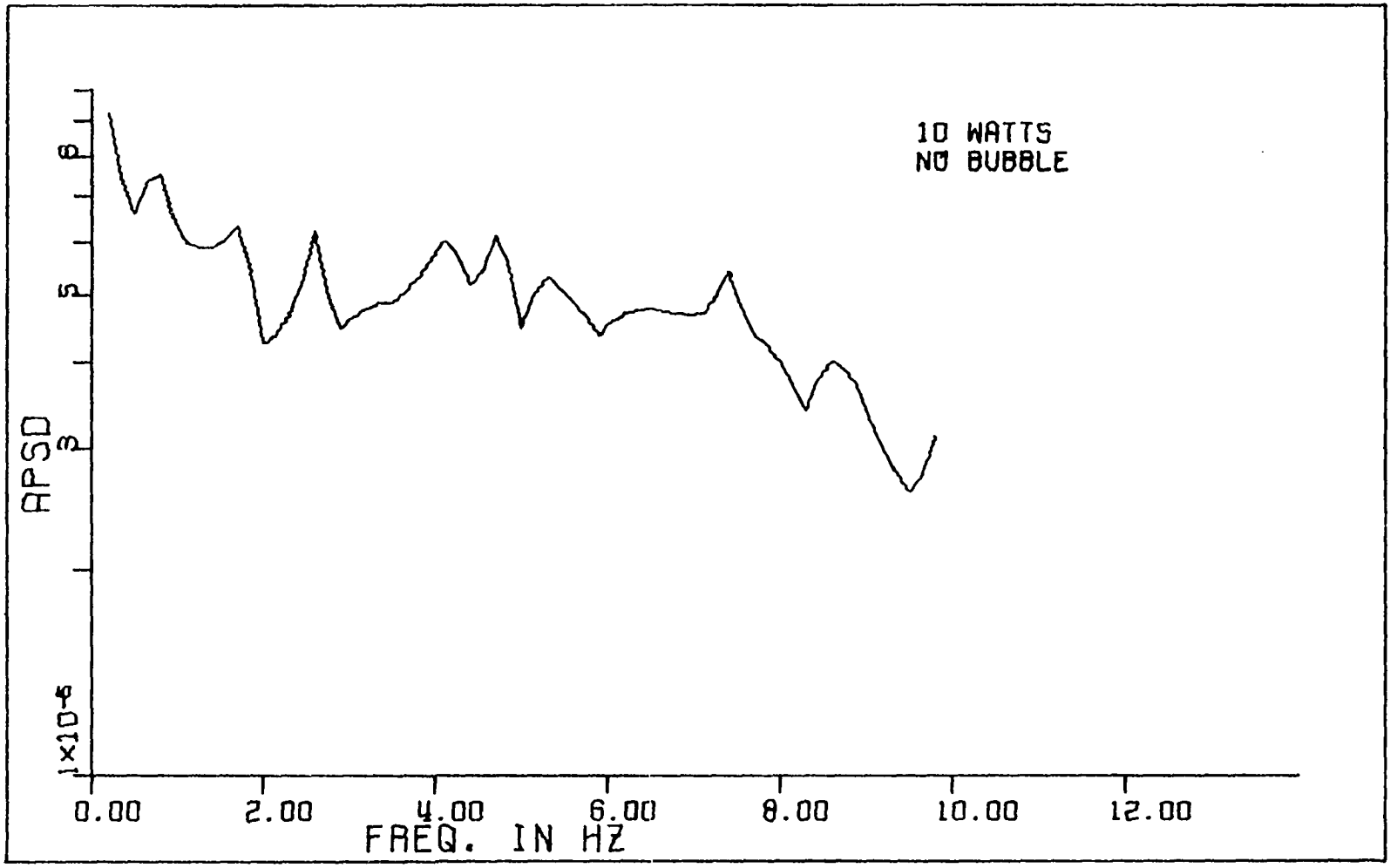

Figure 7.1. APSD for no void generation at a detector displacement of 0 cm and low-pass filter set at 10 Hz

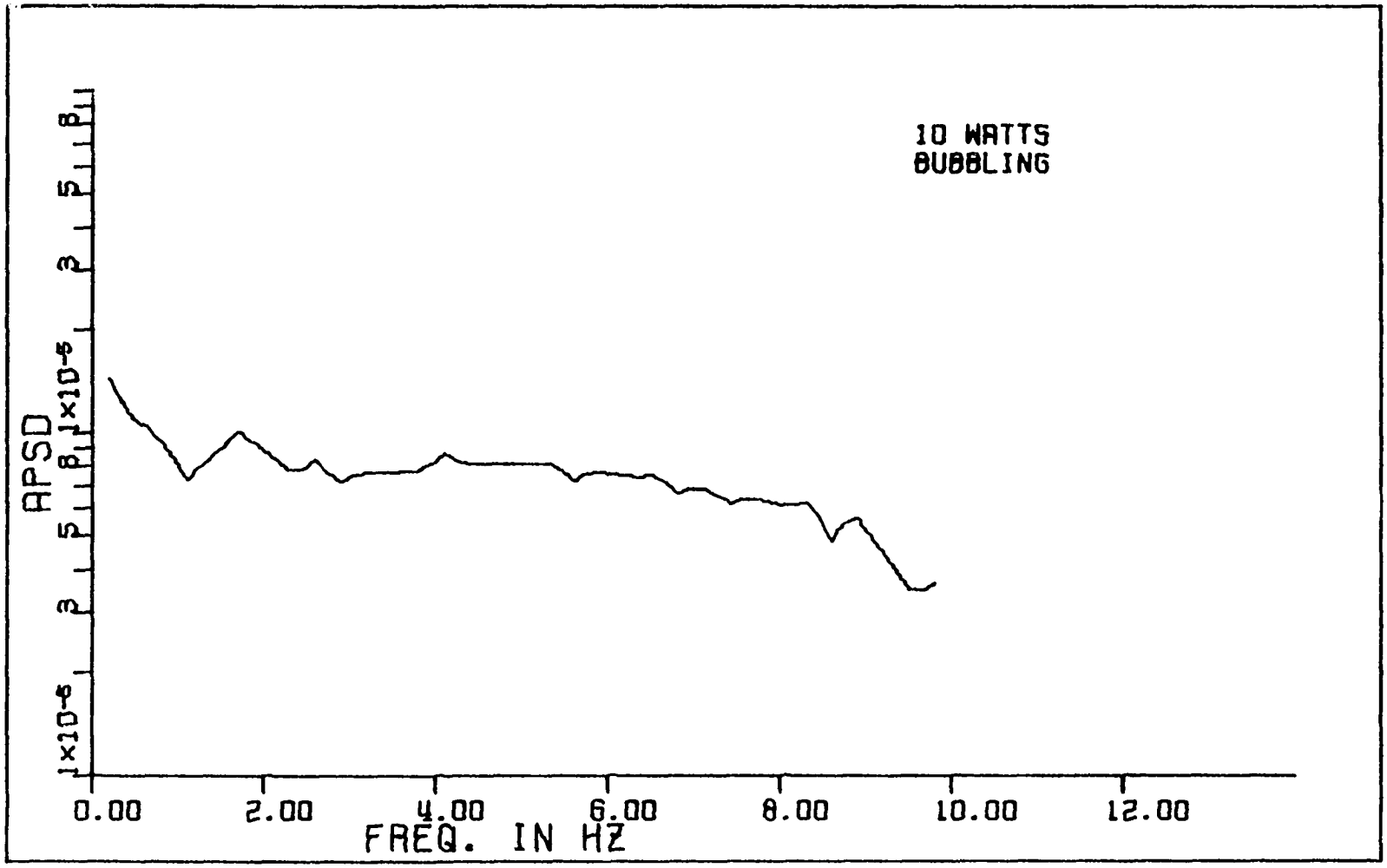

Figure 7.2. APSD for continuous void generation at a detector displacement of 0 cm and low-pass filter set at 10 Hz

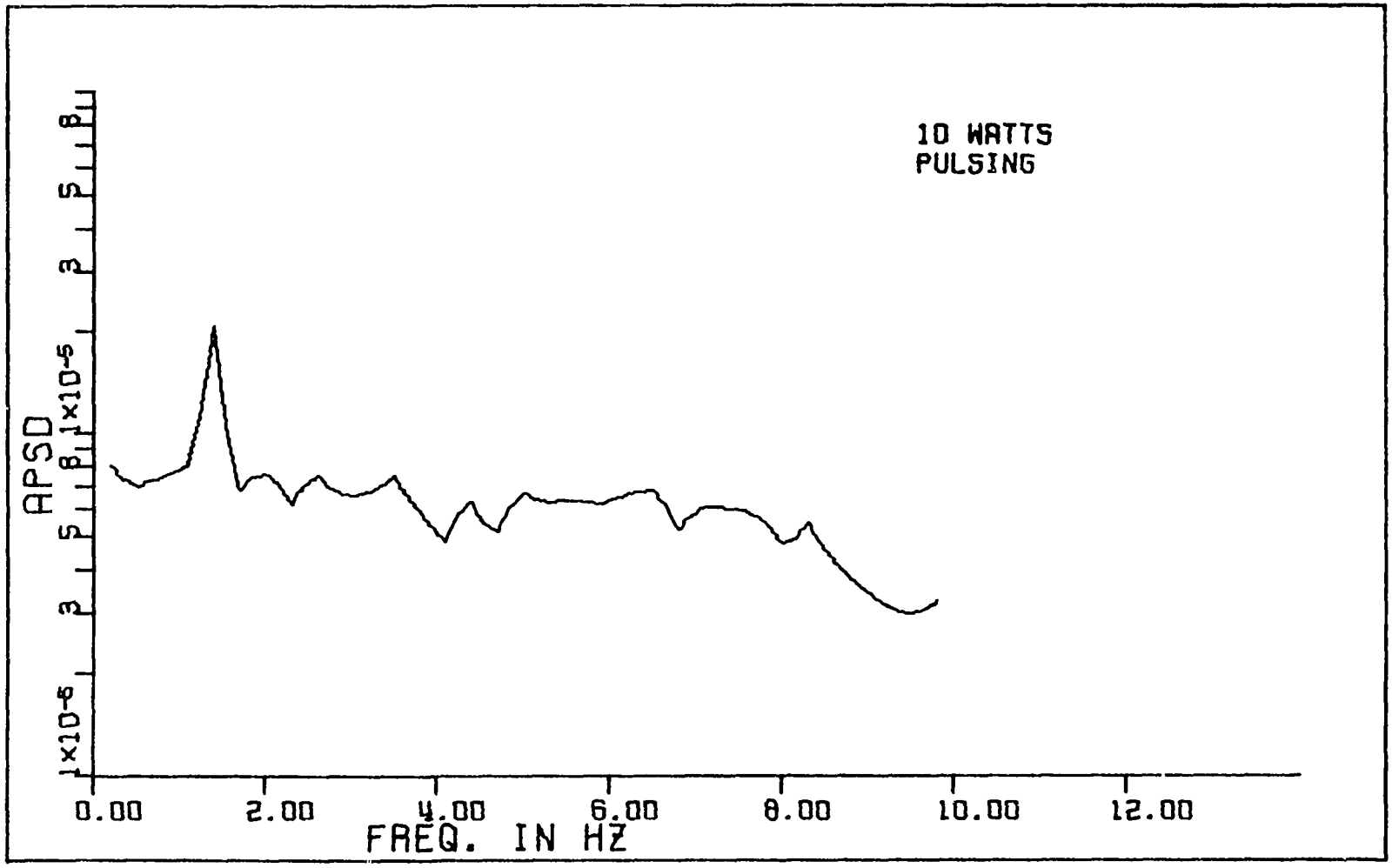

Figure 7.3. APSD for pulsing at 1.5 Hz at a detector displacement of 0 cm and low-pass filter set at 10 Hz

ℓ = number of frequency averages

= 1.

These data gave a record length of 10 seconds for each time segment, a frequency resolution (or bandwidth) of 0.1 Hz and standard error of 16.6%.

No significant chain noise structure, which follows the shape of the zero power transfer function, is found in Figure 7.1. The roll-off at 10 Hz of the APSD in Figure 7.1 is due to the filter cut-off frequency, f_d, which was set at 10 Hz in the experiment. It is found that the APSD of the noise signal (detector current) without void generation is approximately constant in the frequency range between 0.1 Hz and 10 Hz. This implies that the detection noise is dominant over the chain noise and can be viewed as white noise in the frequency range of interest. The APSD for the case of continuous void generation, as can be seen from Figure 7.2, did not provide any noticeable structure change of the spectrum but shows a higher average level. This shows that the APSD for continuous void generation introduced another white noise signal superimposed on the APSD of the detection noise. The APSD for pulsing at 1.5 Hz shows a very sharp peak at a frequency of 1.5 Hz as shown in Figure 7.3. The above results can be seen very clearly in Figure 7.4 in which these three spectra are compared.

These findings can be interpreted using the following physical reasoning. The APSD of the neutron detector current noise, according

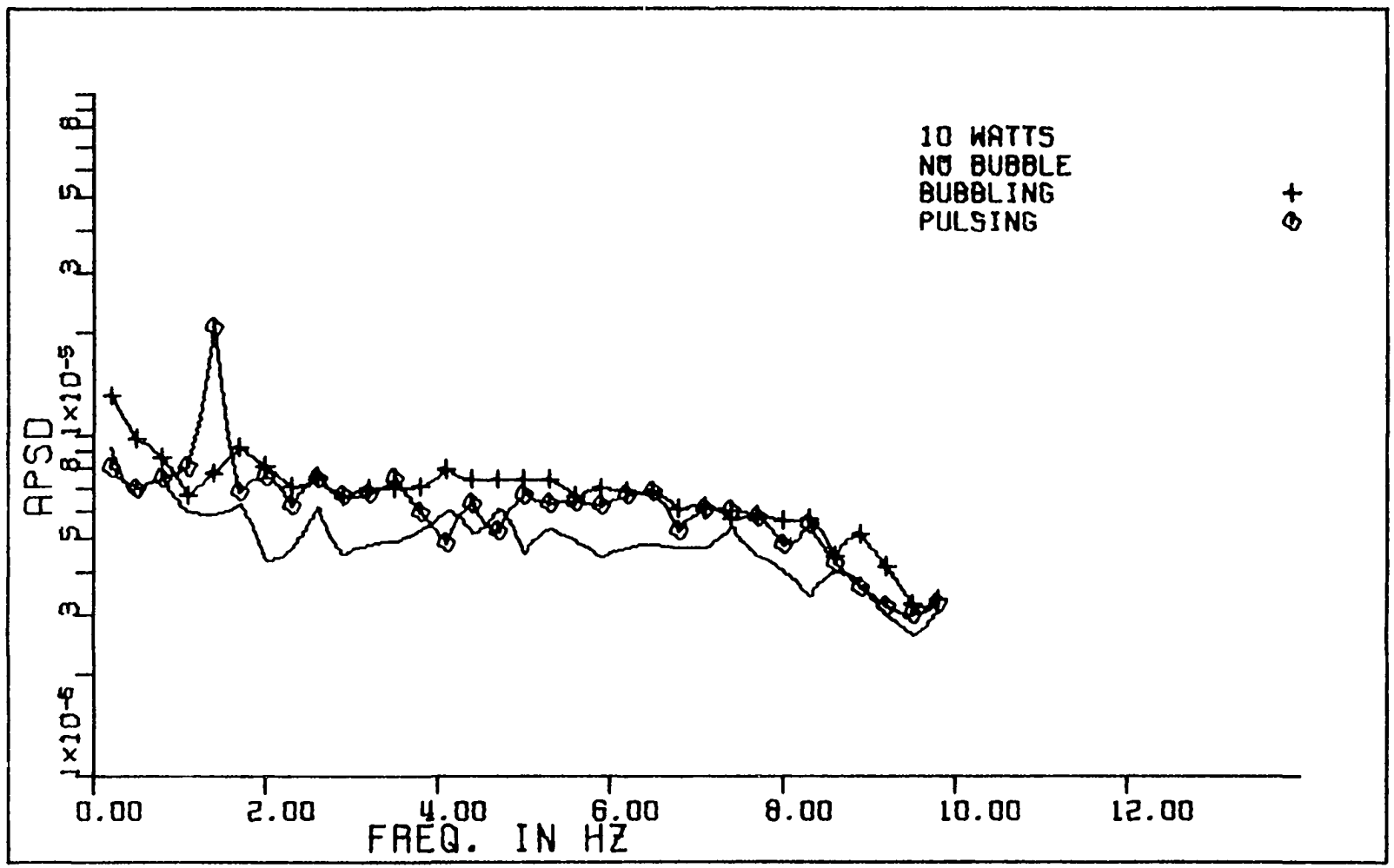

Figure 7.4. APSD's for different void generations at a detector displacement of 0 cm and low-pass filter set at 10 Hz

to Cohn [9] and Seifritz [64], consists of the following three components:

a. The detection noise which is proportional to the product of the reactor power level and the detector efficiency.

b. The chain noise which is proportional to the product of the reactor power level and the square of the detector efficiency.

c. The power noise which is proportional to the square of the product of the detector efficiency and reactor power level.

For the small sized BF_3 detector used in the experiments, the efficiency is very small and is estimated to be approximately 10^{-6} detections/fission. The detection noise is therefore dominant compared to the chain noise when no void generation is introduced. As mentioned earlier in Chapter III, void generation will result in a fluctuation of the neutron flux which is proportional to the reactor power. The APSD of the bubble generation would be proportional to the square of the reactor power and can be treated as power noise in this analysis. With a continuous void generation, the energy from the bubble noise is spread out over the whole spectrum and results in an increase of the mean level of the APSD spectrum. However, with pulsing at 1.5 Hz, the entire energy is concentrated at one frequency point (1.5 Hz and minor amounts in the harmonics) in the spectrum. This is why a very sharp peak was found in the pulsing mode as shown in Figure 7.3.

Based on the above results and analysis, several important conclusions can be made:

a. The chain noise makes negligible contribution to the APSD of the noise signal in the measurements.

b. Without void generation, the detection noise level was found to be much higher than the chain noise. The average detection noise level can be obtained by taking the average value of the APSD spectrum over the frequency range of interest.

c. The detection noise was found to be approximately white within the frequency range of interest. Continuous bubble generation also introduced a white noise input.

d. In order for the detector to "see" the power noise due to void generation, pulsing should be used rather than continuous bubble generation.

e. With pulsing at 1.5 Hz, the frequency range of interest can be reduced to between 0.1 Hz and 4 Hz in which range both the fundamental frequency (1.5 Hz) and the second harmonics (3.0 Hz) are observed.

f. With pulsing at 1.5 Hz, the peak value of the APSD at 1.5 Hz should be the sum of

$$APSD = APSD_c + APSD_d + APSD_{\hat{o}R} \tag{7.1}$$

where

APSD = auto power spectrum density of the experimental measurement

$APSD_c$ = component of chain noise in APSD

$APSD_d$ = component of detection noise in APSD

$APSD_{\delta R}$ = component of the bubble noise in APSD, which is the term defined by Equation (3.65) in Chapter III.

The $APSD_{\delta R}$ (refers to the APSD of the detector response due to the bubble noise) can be estimated by subtracting the average level of the APSD without bubble generation from the measured peak value, given in Equation (7.1), of the APSD at 1.5 Hz.

For the frequency range from 0.1 Hz to 4 Hz, the APSD for pulsing at 1.5 Hz and for no voids are compared in Figure 7.5. The APSD without void generation, as can be seen, is approximately a white noise. A sharp fundamental peak at 1.5 Hz and a relatively high second harmonics peak at 3.0 Hz are found for the pulsing mode as expected.

2. Fixed detector position at different power levels

From the analysis given earlier in this chapter, the component of the APSD due to bubble noise, $APSD_{\delta R}$, is of main interest. It is this value, $APSD_{\delta R}$, which should be compared with that obtained from the modeling calculation using Equation (3.65). Before comparing the results of the $APSD_{\delta R}$ for different power levels at the same detector position, a primary quantitative analysis is given below.

The pulsing of bubbles at 1.5 Hz results in, based on Fourier Series Analysis, a detector current signal which has the form of a summation of sine waves consisting of the fundamental component (1.5 Hz) plus harmonics. Theoretically either the fundamental mode (1.5 Hz) or the harmonics can be used to check the agreement of the experimental

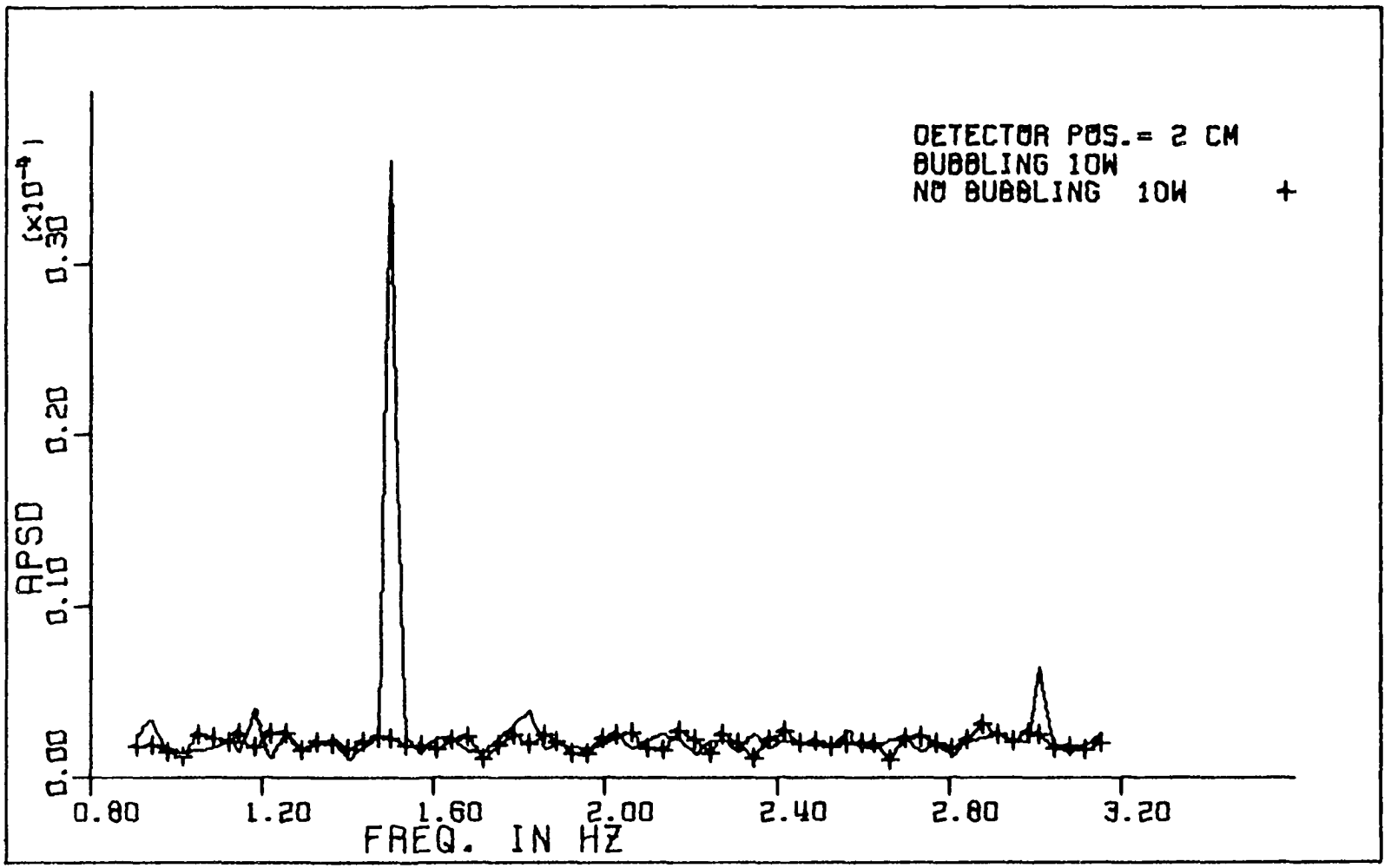

Figure 7.5. APSD's for pulsing at 1.5 Hz and for no voids at a detector displacement of 2 cm

measurement with the detector response model given in Equation (3.65). However, the fundamental mode has a higher amplitude than those of the harmonics. Furthermore, in the detector model derivation given in Chapter III, the Fourier Transform was applied at a frequency which lies between λ and β/ℓ, and the modeling calculations were also carried out based on this frequency. Therefore, the analysis given below will be based on the fundamental mode rather than on the harmonics.

The APSD of the sine wave (fundamental mode) plus random noise (the detector noise plus chain noise, if any) is simply the sum of the power spectrum for the sine wave, which is a delta function centered at the frequency of the fundamental, ω_0, and the random noise. The $APSD_{\delta R}$ due to the fundamental sine wave excitation (which is produced from pulsing bubbles at 1.5 Hz), $APSD_{\delta R}(\omega_0)$, can be found from

$$APSD_{\delta R}(\omega_0) = APSD(\omega_0) - APSD_c(\omega_0) - \text{Avg. } APSD_d(\omega) \tag{7.2}$$

where $APSD(\omega_0)$, $APSD_c(\omega_0)$, $APSD_d(\omega)$, $APSD_{\delta R}(\omega_0)$ are the quantities defined in Equation (7.1). Avg. $APSD_d(\omega)$ represents the average value of the $APSD_d(\omega)$ over the frequency range of interest (0.1 Hz to 4 Hz).

In order to confirm that the bubble noise (power noise) is proportional to the square of the reactor power level, the value of $APSD_{\delta R}$'s at 1.5 Hz ($APSD_{\delta R}(\omega_0)$) for different power levels were calculated and are given in Table 7.1.

In Table 7.1, the input data for the Fast Fourier Transform (FFT) program for the pulsing mode are

Table 7.1. The experimental APSD's for different reactor power and at a detector position of 2 cm

Reactor power (watts)		(a) Avg. APSD(ω) (relative unit)	(b) APSD (ω_0) (relative unit)	(c) $APSD_{\delta R}(\omega_0)$ = (a)-(b)
5	No voids	1.40 E-6 ± 2.32 E-8	-	-
5	Pulsing at 1.5 Hz	-	1.10 E-5 ± 1.76 E-6	0.97 E-5 ± 1.76 E-6
10	No void	2.20 E-6 ± 3.60 E-8	-	-
10	Pulsing at 1.5 Hz	-	3.60 E-5 ± 5.76 E-6	3.38 E-5 ± 5.76 E-6

$N = 256, \quad f_s = 10 \text{ Hz}, \quad f_d = 4 \text{ Hz},$

$q = 36, \quad \ell = 1.$

A hundred frequency points ($\ell = 100$) were averaged in calculating the average detector noise, Avg. $APSD_d(\omega)$.

The ratio of the $APSD_{\delta R}(\omega_0)$ at ten watts to the $APSD_{\delta R}(\omega_0)$ at five watts is given by Table 7.1 as

$$\frac{3.38 \text{ E-5} \pm 5.76 \text{ E-6}}{0.97 \text{ E-5} \pm 1.76 \text{ E-6}} \tag{7.3}$$

From the principles of the propagation of errors [56] the ratio is found to be

$3.48 \pm 0.816.$

The expected ratio for the $APSD_{\delta R}(\omega_0)$ at ten watts and at five watts should be equal to four since the bubble noise is proportional to the square of the reactor power level.

From the above analysis, the experimental value of the ratio of $APSD_{\delta R}(\omega_0)$ for different power level is found to be within the experimental error associated with the measurement as compared to the theoretical value.

Figure 7.6 shows the APSD of the detector response for reactor power at five watts and at ten watts. The differences between the peaks of the fundamental frequency (1.5 Hz) and the average detection noise levels for different power levels can be seen very clearly from Figure 7.6. It is noted here that a second harmonics peak is

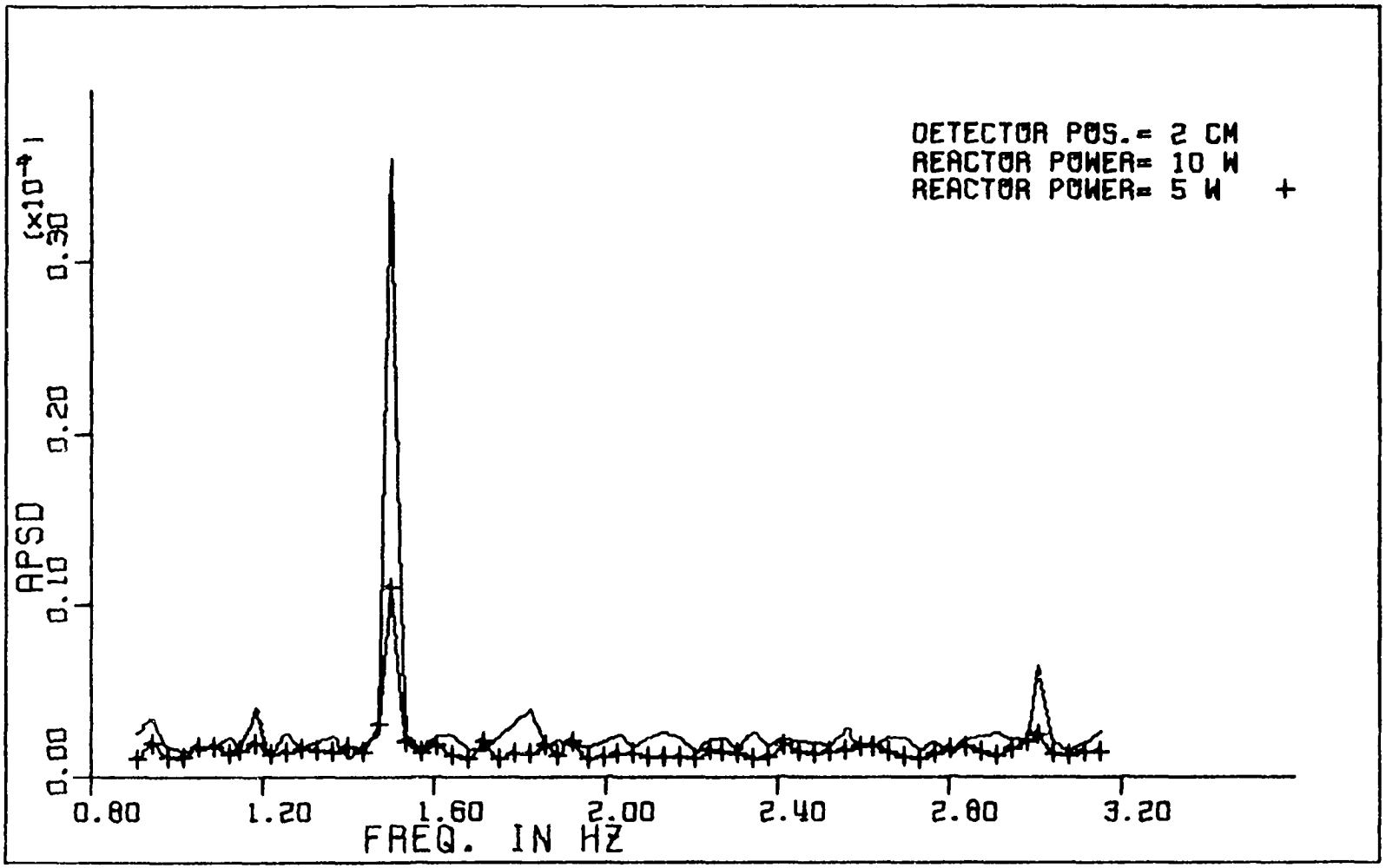

Figure 7.6. The APSD's for the pulsing mode for different reactor power levels at a fixed detector position

found at 3.0 Hz for a reactor power of ten watts. However, no second harmonics peak is found for the case of five watts. This is due to the fact that at five watts the second harmonics peak is so low that it is merged into the detection noise level and does not appear in the APSD.

3. Fixed power level and different detector positions

With the water bubbler at a fixed position, measurements were carried out for several detector positions. The calculated APSD's are shown in Figures 7.7 through 7.10.

By investigating these figures, it is found that

a. All APSD's of the detector response have a sharp peak at the fundamental frequency of 1.5 Hz. The amplitude of the peaks decrease with increasing distance between the detector and the water bubbler.

b. All APSD's of the detector response also have a peak at 3.0 Hz (the second harmonic) except for the cases with a detector displacement of 12 cm and 16 cm.

The disappearance of the second harmonic peak for detector positions greater than 12 cm from the bubbler is because that beyond 12 cm and further, the second harmonics level is approximately the same as the detector noise level and is no longer distinguishable.

The experimental measured APSD's characteristics are summarized in Table 7.2.

Note in Table 7.2 that the value of the $APSD_{\delta R}$'s of the bubble

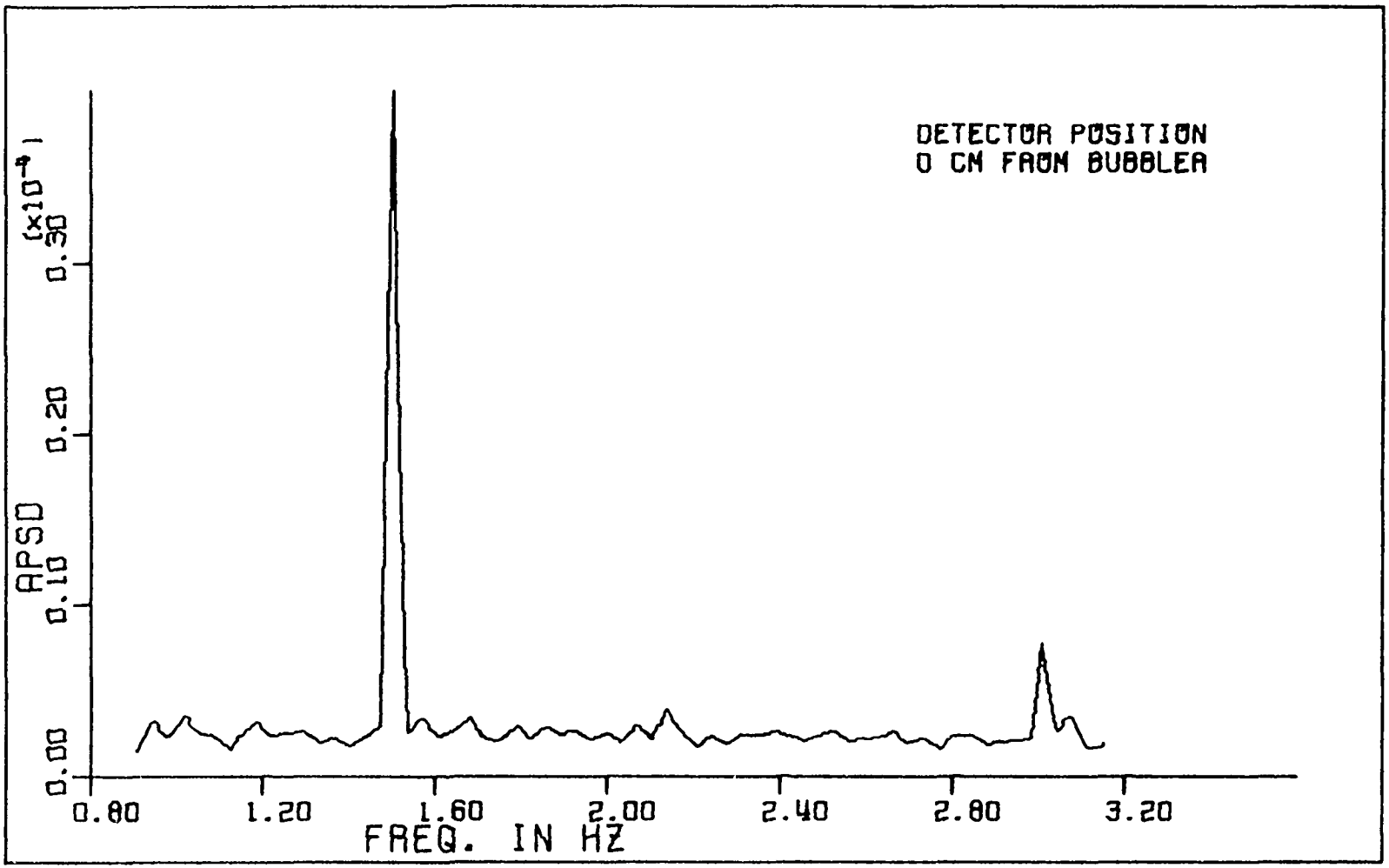

Figure 7.7. APSD for the pulsing mode with reactor power of 10 watts and at a detector displacement of 0 cm

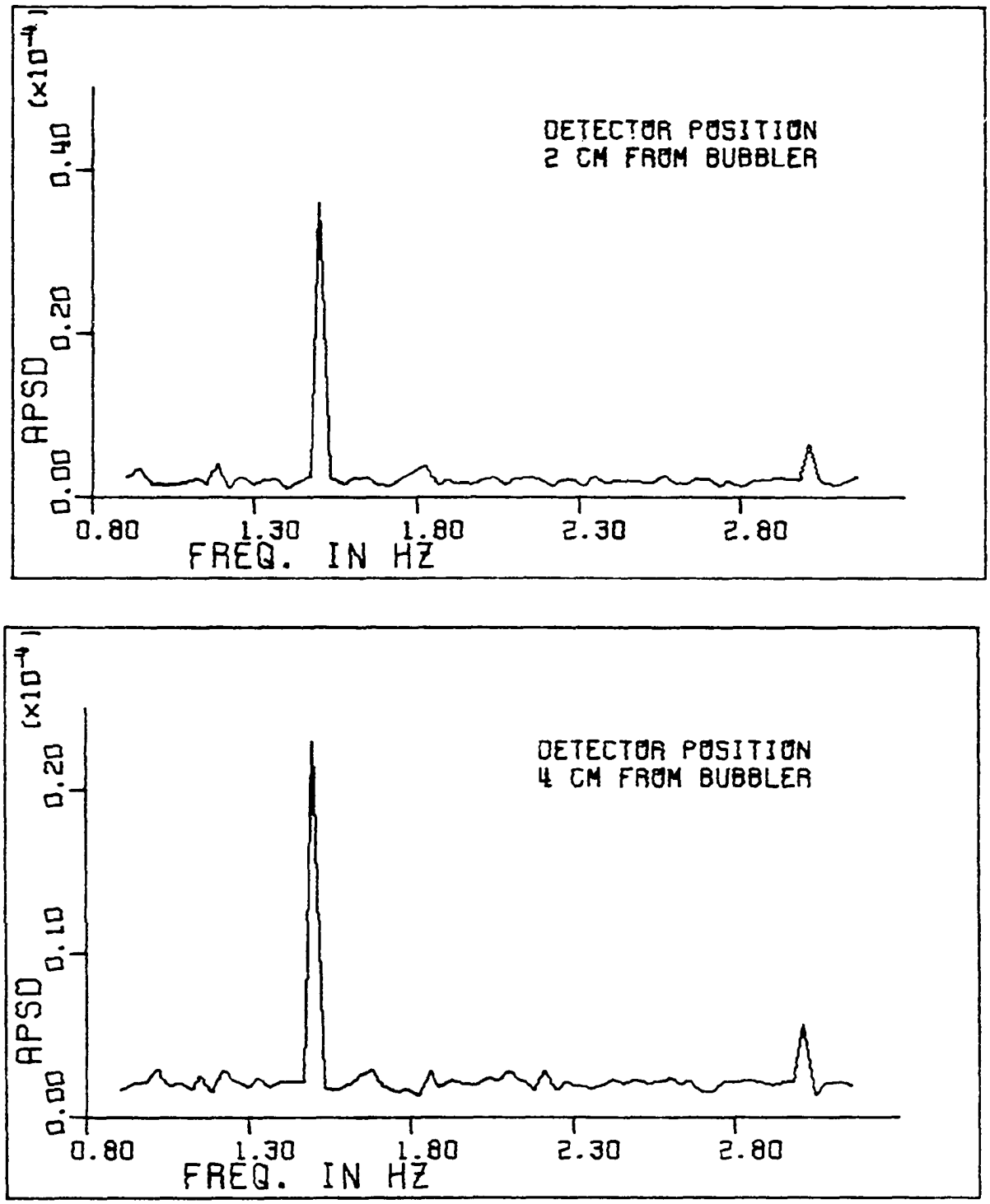

Figure 7.8. APSD's for the pulsing mode with reactor power of 10 watts and at a detector displacement of 2 cm and 4 cm

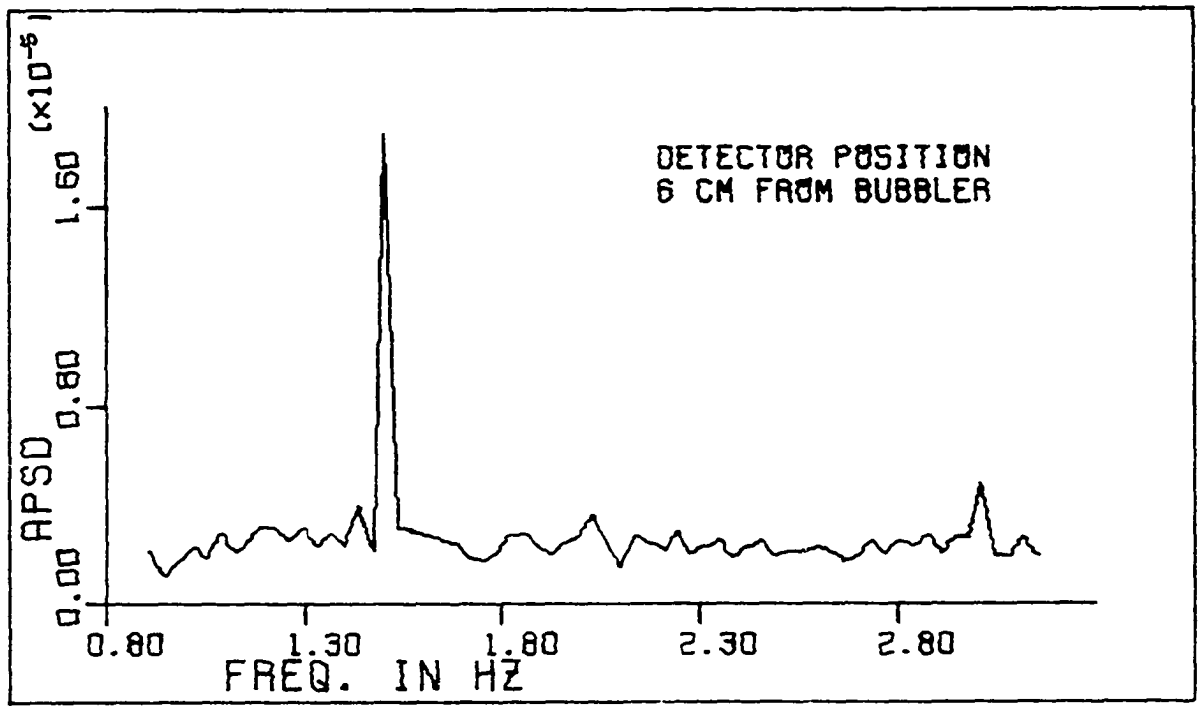

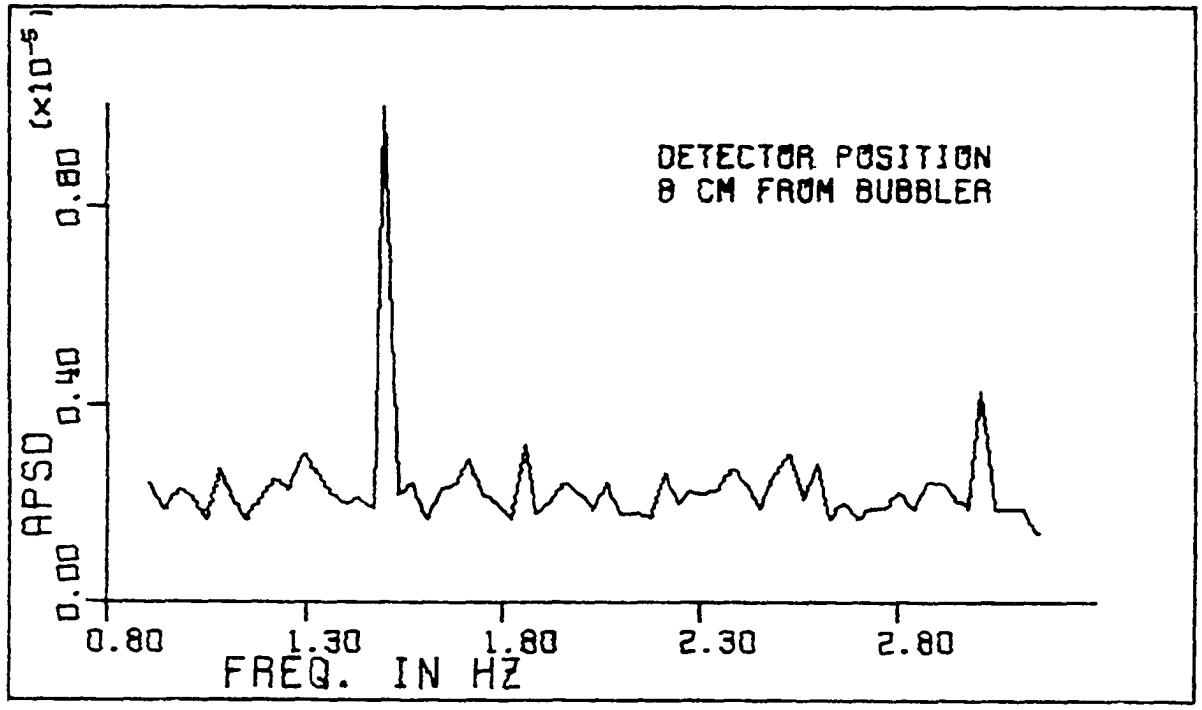

Figure 7.9. APSD's for the pulsing mode with reactor power of 10 watts and at a detector displacement of 6 cm and 8 cm

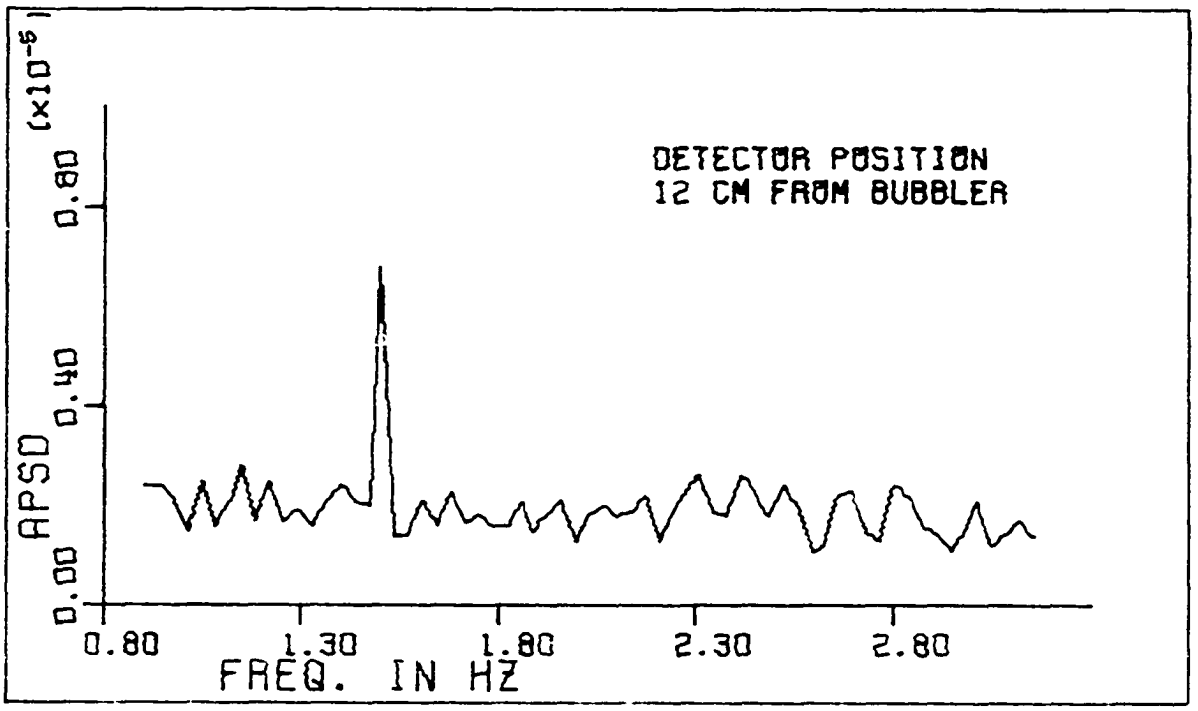

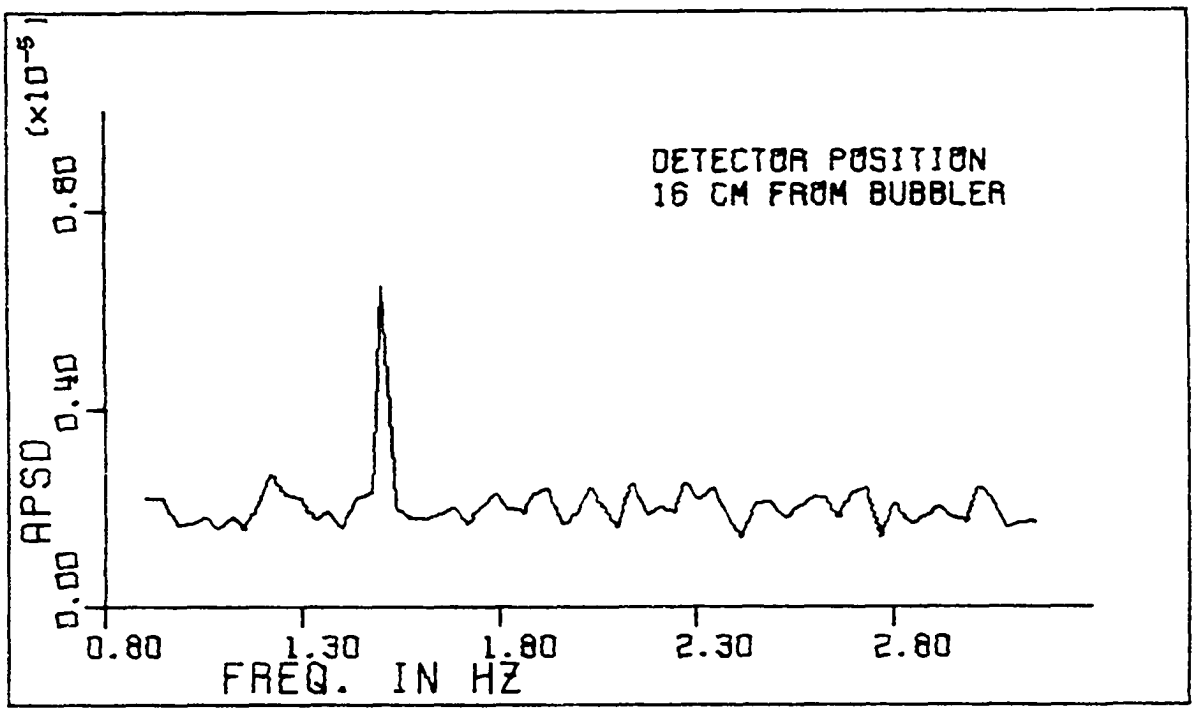

Figure 7.10. APSD's for the pulsing mode with reactor power of 10 watts and at detector displacement of 12 cm and 16 cm

Table 7.2. The experimental APSD's for different detector positions at a fixed reactor power of ten watts

Detector position (cm)	$APSD(\omega_0)$ Freq. (Hz)	$APSD(\omega_0)$ Amplitude (relative unit)	Avg. $APSD(\omega)$ (relative unit)	$APSD_{\delta R}(\omega_0)$ at 1.5 Hz = $APSD(\omega_0)$ - Avg. $APSD(\omega)$
0	1.5	4.00 E-5 ± 6.40 E-6	2.39 E-6 ± 3.51 E-8	3.76 E-5 ± 6.40 E-6
2	1.5	3.60 E-5 ± 5.80 E-6	2.20 E-6 ± 3.51 E-8	3.38 E-5 ± 5.80 E-6
4	1.5	2.30 E-5 ± 3.70 E-6	2.12 E-6 ± 3.31 E-8	2.09 E-5 ± 3.70 E-6
6	1.5	1.90 E-5 ± 3.10 E-6	2.12 E-6 ± 3.31 E-8	1.69 E-5 ± 3.10 E-6
8	1.5	1.00 E-5 ± 1.60 E-6	2.23 E-6 ± 3.52 E-8	0.78 E-5 ± 1.60 E-6
12	1.5	6.80 E-6 ± 1.10 E-6	1.92 E-6 ± 3.11 E-8	0.49 E-5 ± 1.10 E-6
16	1.5	6.50 E-6 ± 1.00 E-6	2.02 E-6 ± 3.22 E-8	0.43 E-5 ± 1.00 E-6

noise are calculated by subtracting the average detection noise from the peak value of the APSD at 1.5 Hz, $APSD(\omega_0)$.

B. The Detector Response Model Evaluation

As mentioned in Chapter III, the detector response model given by Equations (3.65) and (3.59) can be verified experimentally by measuring the APSD of the detector response due to the bubble noise alone, i.e. $APSD_{\delta R}$'s. The $APSD_{\delta R}$'s due to 20% void generation inside the water bubbler were calculated using the WHIRLAWAY-H code modeling calculation and the results are shown in Table 5.2.

Based on the analysis given earlier in this chapter, the measured APSD of the detector response should be the sum of the chain noise due to branching processes in the reactor, the detection noise due to the neutron detection process of the instrumentation, and the power noise (bubble noise) due to void generation. It was found, from the previous analysis, that the chain noise was negligible, the detection noise was approximately white in the frequency range of interest, and the bubble noise ($APSD_{\delta R}$) due to pulsing bubble generation was dominant and had introduced a very sharp, delta function type peak at 1.5 Hz in the APSD spectrum. It was concluded earlier that

$$APSD_R(\omega_0) \simeq APSD(\omega_0) - \text{Avg. } APSD(\omega) \tag{7.4}$$

and these values are given in Table 7.2.

Since only the peak of the $APSD_{\delta R}$'s as a function of the relative distance between the detector and the water bubble is of interest, the $APSD_{\delta R}$'s were normalized to the $APSD_{\delta R}$ at 0 cm detector displacement position. The normalized $APSD_{\delta R}$'s, which are defined as

$$NAPSD_{\delta R}(\vec{r},\omega) = \frac{APSD(\vec{r},\omega)}{APSD(0,\omega)}, \tag{7.5}$$

are given in Table 7.3 along with those evaluated using the WHIRLAWAY-H modeling calculations. Note that as for Equation (7.3), the standard deviation for a quotient, was used in evaluating the standard deviation of $NAPSD_{\delta R}(\vec{r},\omega)$ defined in Equation (7.5). These normalized curves for the experimental measurements and the WHIRLAWAY-H results are shown in Figure 7.11 with the standard error (or deviation) bar drawn on the measured detector positions.

By investigating Table 7.3 and Figure 7.11 it is seen that the agreement between the experimental measurements and the modeling calculations are found to be quite consistent and agree within experimental error.

The deviation between the experimental results and the modeling calculations might arise from:

a. the omission of the imaginary part of the adjoint fluxes in the detector response model evaluation,

b. the slight discrepancy in the UTR-10 three-dimensional modeling due to neglecting the control rods, structure materials and the air gaps,

Table 7.3. The experimental and WHIRLAWAY-H calculated $NAPSD_{\delta R}$ due to pulsing voids at 1.5 Hz for different detector positions

Detector position $\vec{r}$ (cm)	$NAPSD_{\delta R}(\vec{r},\omega_0)$	
	WHIRLAWAY-H results	Experimental results
0	1.000	1.000
2	0.971	0.900 ± 0.211
4	-	0.553 ± 0.136
6	-	0.446 ± 0.085
8	0.278	0.205 ± 0.055
12	-	0.130 ± 0.036
16	0.124	0.115 ± 0.032
28	0.052	

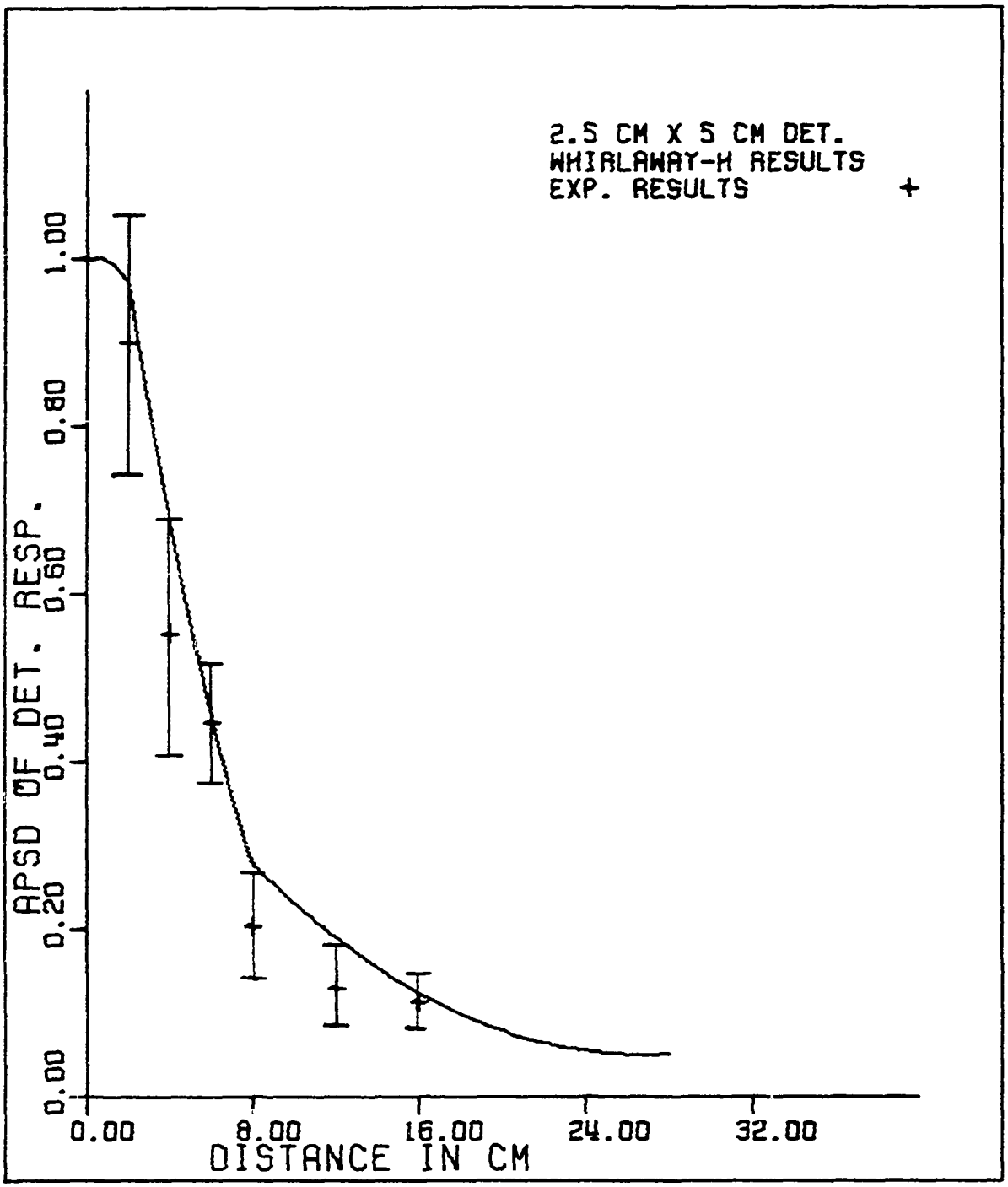

Figure 7.11. The experimental and the WHIRLAWAY-H calculated $NAPSD_{\delta R}$'s for different detector positions

c. the assumption of an infinitely small, uniform void generation which contradicts the real void pattern produced by pulsing the water bubbler, and

d. the approximations used in representing the finite sized detector and noise source in the theoretical model. As shown in Figures 5.11 and 5.12, the results are sensitive to the size of the volumes used in the theoretical model.

VIII. CONCLUSIONS

The detector model developed in this research is more realistic and sophisticated than those developed by other investigators [4, 11, 36, 38, 54] due to the following facts:

1. Both the location and the size of the detector as well as the noise source were taken into account.
2. The modeling calculations, using the WHIRLAWAY-H code, were based on a three-dimensional model of a UTR-10 type reactor and were verified by experimental measurements.
3. A multigroup formulation was used and the adjoint fluxes can be taken as complex quantities if it is required.

The main objectives of this work were to provide a working model which describes the detector response to reactor core parametric fluctuations and to carry out experimental confirmation of the model. It was found that the use of the detector adjoint function and the detector response model provides satisfactory results in analyzing the detector response signal to void generation inside the core region of a UTR-10 type reactor. For the analysis of other kinds of core parametric fluctuations inside a power reactor such as coolant temperature fluctuations, pressure fluctuations, control rod and fuel rod vibration, a better understanding of the noise signal transmission process which extends from the noise fluctuation to detector current is required.

However, the present work provides a basis for further work to

develop a quantitative understanding of the detector signal characteristics due to noise fluctuations and, hopefully, will lead to the possibility of constructing a more realistic and sophisticated detector model.

The important results of this investigation may be summarized as follows:

1. The neutron detector has a volume of sensitivity ($\simeq$ 8 cm in radius) near the noise source. This finding confirms the local-global concept of the detector signal proposed by several authors [36, 38, 54].
2. The detector response function is sensitive to the volume of the noise source.
3. The bubble generation can be treated as power noise. The measured $APSD_{\delta R}$'s of the detector response due to bubble generation, at different reactor power levels, were found to be proportional to the square of the power level. This leads to the conclusion that the $APSD_{\delta R}$ is sensitive to reactor power level.
4. The $APSD_{\delta R}$ is sensitive to the separation between the detector and the noise source.
5. The $APSD_{\delta R}$ with respect to continuous bubble generation, may be treated as white noise within the frequency range

   $$\lambda << \omega << \beta/\ell$$

   for a low power reactor.

6. Pulsing bubbles at a specific frequency produces a very sharp peak at the pulsing frequency in the APSD spectrum of the detector response. This technique helps in the experimental identification of the noise source in the APSD spectrum when the noise source strength is small and the efficiency of the neutron detector is low.
7. The function $\psi(\vec{r}_s,\vec{r}_d)$, i.e. the value of the adjoint function at $\vec{r}_s$ due to detector at $\vec{r}_d$, is a very powerful tool in analyzing the detector response function.

IX. SUGGESTIONS FOR FUTURE WORK

Several suggestions for future work, which would lead to a more realistic and sophisticated detector model and would provide a fundamental basis for better understanding of the noise signal, are the following:

1. Further investigation of the detector response model should be carried out by using neutron detectors with different detector adjoint functions, i.e. threshold detectors in combination with thermal neutron detector.
2. Experimental work should be performed to find the effect of different detector sizes.
3. Two detector cross correlation methods could be utilized to investigate the cross power spectral densities between two detectors. This would provide information on the phase angle of the detector response function.
4. A transport formulation of the detector model could be developed. This would give information on the angular dependence of the neutron detector to noise sources.
5. The detector model could be extended to include the effect of a moving perturbation, such as a vibrating absorber, inside the reactor core.
6. Analysis can be carried out to interpret the effects of the second harmonic of the pulsing bubbles on the detector response function.

X. LITERATURE CITED

1. G. T. Analytis, Investigation of the space-dependent global component of the neutron-to-inlet coolant temperature fluctuations transfer function, Annals of Nucl. Energy 5, 597 (1979).

2. R. F. Barry, LEOPARD - A spectrum dependent non-spatial depletion code for the IBM-7094, WCAP-3269-26 (1963).

3. K. Behringer, G. Kosaly and Lj. Kostic, Theoretical investigation of the local and global components of the neutron noise field in BWR, Nucl. Sci. Engr. 63, 306 (1977).

4. G. I. Bell and S. Glasstone, Nuclear Reactor Theory (Van Nostrand Reinhold, New York, 1970), p. 257.

5. J. S. Bendat, Random Data: Analysis and Measurement Procedures (Wiley and Sons, Inc., New York, 1971).

6. R. S. Booth, Second specialists meeting on reactor noise, Nucl. Safety 19, 468 (1978).

7. M. Chen, A. multipurpose computer code for the UTR-10 reactor, M.S. thesis, Department of Nuclear Engineering, Iowa State University, 1974 (unpublished).

8. D. Childers and A. Durling, Digital Filtering and Signal Processing (West Publishing Company, New York, 1975).

9. C. Cohn, A simplified theory of pile noise, Nucl. Sci. Engr. 7, 472 (1960).

10. A. Colombino, Further developments towards a unified theory for reactor neutron noise analysis techniques, Annals of Nucl. Energy 3, 323 (1976).

11. H. Van Dam, Neutron noise in boiling water reactors, Atomkernenergie 27, No. 1, 8 (1976).

12. H. Van Dam, On the adjoint space in reactor noise theory, Annals of Nucl. Energy 4, 185 (1977).

13. D. D. Ebert, Investigation of the space- and energy department coherence function in zero-power coupled-core reactors, Nucl. Sci. Engr. 55, 363 (1974).

14. D. D. Ebert, Interpretation of coherence function measurements in zero-power coupled-core reactors, Nucl. Sci. Engr. 55, 380 (1974).

15. T. B. Fowler and M. Tobias, WHIRLAWAY - A three-dimensional, two-group neutron diffusion code for IBM 7090 computer, ORNL-3150 (1961).

16. B. Frogner and H. S. Rao, Control of nuclear power plants, IEEE Trans. on Automatic Control AC-23, No. 3, 405 (1978).

17. D. N. Fry, Experience in reactor malfunction diagnosis using on-line noise analysis, Nucl. Technology 10, 273 (1971).

18. R. Fuge and J. Valko, Measurement of the local and global effect of bubbles in a water moderated reactor, Annals of Nucl. Energy 4, 161 (1977).

19. Kohyu Fukunishi, Coherence analysis of boiling water reactor noise, Journal of Nucl. Sci. Engr. 14, No. 5, 351 (1977).

20. Kohyu Fukunishi, Noise source estimation of boiling water reactor fluctuation by autoregression, Nucl. Sci. Engr. 67, 296 (1978).

21. A Gandini, Perturbation methods in nuclear reactor from the importance conservation principle, Nucl. Sci. Engr. 35, 141 (1969).

22. E. Greenspan, Comments on "A note on the adjoint function in time-dependent reactor theory," Annals of Nucl. Energy 3, 329 (1976).

23. E. Greenspan, Some applications of the adjoint function in reactor theory, Annals of Nucl. Energy 3, 147 (1976).

24. E. Greenspan, Perturbation theory and importance functions in integral transport formulations, Nucl. Sci. Engr. 61, 170 (1976).

25. E. Greenspan, On the adjoint space in reactor theory, Annals of Nucl. Energy 3, 323 (1976).

26. E. W. Hagen, ed., Proc. NEACRP specialist meeting on reactor noise (SMORN-I), Rome, Italy, Oct. 1974. Annals of Nucl. Energy 2 (1975).

27. E. W. Hagen, ed., Proc. Second specialist meeting on reactor noise (SMORN-II), Gatlinburg, Tennessee, U.S.A., Sept. 1977. Progress on Nucl. Energy (New series) 1, No. 2-4 (1977).

28. G. E. Hansen and H. A. Sandmeier, Neutron penetration factors obtained by using adjoint transport calculations, Nucl. Sci. Engr. 22, 315 (1965).

29. A. A. Harris, Dynamic effects in radiation diagnosis of fluctuating voids, Nucl. Sci. Engr. 46, 408 (1971).

30. T. J. Hoffman, The adjoint difference method and its applications to deep-penetration radiation transport, Nucl. Sci. Engr. 48, 179 (1972).

31. R. H. Jason, The role of the adjoint flux in determining reactor stability, ANL-7189 (1966).

32. H. Kodaira, Method of experimental power reactor noise analysis without use of high power reactor, Journal of Nucl. Sci. Technology 14, 710 (1977).

33. H. Kokame, Kalman filter applied to estimation of neutron flux distribution and optimum allocation of in-core detectors, Journal of Nucl. Sci. Technology 14, 695 (1977).

34. H. Kokame, A method for rapid detection of unexpected reactivity insertion into a nuclear reactor, Nucl. Sci. Engr. 67, 8 (1978).

35. G. Kosaly, Investigation of the possibility of using static calculations in the theory of neutron noise, Annals of Nucl. Energy 4, 79 (1977).

36. G. Kosaly, Remarks on a few problems in the theory of power reactor noise, Nucl. Energy 14, No. 3, 67 (1973).

37. G. Kosaly, L. Maroti and L. Mesko, A simple space dependent theory of the neutron noise in a boiling water reactor, Annals of Nucl. Energy 2, 315 (1975).

38. G. Kosaly and L. Mesko, Investigation of the local component of power reactor noise via diffusion theory, Report of the Central Research Institute for Physics KFKI-75-27 (1975).

39. G. Kosaly and L. Mesko, Remarks on the transfer function relating inlet temperature fluctuations to neutron noise, Atumkernenergie 20, Nol 1, 33 (1972).

40. G. Kosaly and L. Mesko, Theory of the auto-spectrum of the local component of power reactor noise, Annals of Nucl. Energy 3, 233 (1976).

41. G. Kosaly and M. M. R. Williams, Point theory of the neutron noise induced by inlet temperature fluctuations and random mechanical vibrations, Atomkernenergie 18, No. 3, 203 (1971).

42. J. Lewins, Importance - The Adjoint Function (Pergamon Press, New York, 1965).

43. J. Lewins, Reactor noise theory as a Markov process, Atomkernenergie 31, No. 4, 223 (1978).

44. J. Ligou, The importance factor of a source in reactor kinetics, Nucl. Sci. Engr. 66, 229 (1978).

45. K. Matsubara, Experimental studies of core flow fluctuations as noise source in BWR, Journal of Nucl. Sci. and Technology 15, 219 (1978).

46. C. W. Mayo, In-core neutron noise analysis, Symposium on Power Plant Dynamics, Control and Testing, Knoxville, Tenn. (1973).

47. Eugen Merbacher, Quantum Mechanics (McGraw Hill, New York, 1970).

48. S. T. Munson, The FOG code, M. E. thesis, Department of Nuclear Engineering, Iowa State University, 1973 (unpublished).

49. T. Nishigori, Hidden state-variable and a non-Markoffian formulation of reactor noise, Journal of Nucl. Sci. and Technology 13, 708 (1976).

50. M. J. Nowark, Reactor physics of UTR-10, ASAE-19 (1957).

51. Y. Oka, Some relations of neutronic noise with fluctuations of inlet coolant temperature and vibration of a control rod obtained by simultaneous measurements at KUR, Journal of Nucl. Sci.. and Technology 14, 869 (1977).

52. Operating Manual for UTR-10 Reactor, ATL-136, Advanced Technology Laboratories, Mountain View, California (1959).

53. Operating and Maintenance Manual for Solid State Digitally Tuned Variable Filters, Krohn-Hite Corporation, Cambridge, Mass., 6 (1975).

54. I. Pazsit, Two-group theory of noise in reflected reactors with application to vibrating absorbers, Annals of Nucl. Energy 5, 185 (1978).

55. K. R. Piety and J. C. Robinson, An on-line reactor surveillance algorithm based on multivariate analysis of noise, Nucl. Sci. Engr. 59, 369 (1976).

56. W. J. Price, Nuclear Radiation Detection (McGraw-Hill, New York, 1964).

57. Y. Ronen, A note on the adjoint function in time dependent reactor theory, Annals of Nucl. Sci. Engr. 1, 515 (1974).

58. G. Rothman, Neutron transport in boiling media, Atomkernenergie 21, No. 2, 105 (1973).

59. K. Saito, On the theory of power reactor noise-I, Annals of Nucl. Sci. Engr. 1, 31 (1974).

60. K. Saito, On the theory of power reactor noise - II, Annals of Nucl. Sci. Engr. 1, 107 (1974).

61. K. Saito, On the theory of power reactor noise - III, Annals of Nucl. Sci. Engr. 1, 209 (1974).

62. P. Schweizer, Design of specifically optimal filters for nuclear reactor systems, IEEE Trans. on Nucl. Sci. 25, 403 (1978).

63. W. Seifritz, An analysis of the space dependent neutron flux density fluctuations at Lingen Boiling Water Reactor by methods of stochastic processes, Atomkernenergie 19, No. 18, 271 (1972).

64. W. Seifritz, At power reactor noise induced by fluctuations of coolant flow, Atomkernenergie 16, No. 29, 208 (1972).

65. W. Seifritz, The polarity correlation of reactor noise in the frequency domain, Nucl. Applications and Technology 7, 513 (1969).

66. W. Seifritz and D. Stegemann, Reactor noise analysis, Atomic Energy Review 9, 129 (1971).

67. D. S. Selengut, Variational analysis of multi-dimensional systems, HW-59126, 89 (1959).

68. Om P. Singh and D. Stegemann, Theoretical treatment of noise analysis in BWR, Atomkernenergie 31, No. 2, 74 (1978).

69. D. Stegemann, Operating characteristics of a boiling water reactor deduced from in-core measurements, Symposium on Power Plant Dynamics, Control and Testing, Knoxville, Tenn. (1973).

70. J. A. Thie, Reactor Noise (Rowman and Little field, Inc., New York, 1963).

71. J. A. Thie, The 1974 specialists meeting on reactor noise, Nucl. Safety 16, 308 (1975).

72. M. Tobias, the EQUIPOISE METHOD - A simple procedure for few-group diffusion calculation in two and three dimensions, Nucl. Sci. Engr. 12, 513 (1962).

73. R. E. Uhrig, Random Noise Techniques in Nuclear Reactor Systems (Ronald Press, New York, 1970).

74. D. Wach and G. Kosaly, Investigation of the joint effect of local and global driving sources in in-core neutron noise measurements, Atomkernenergie 23, No. 4, 244 (1974).

75. M. M. R. Williams, Random Process in Nuclear Reactors (Pergamon Press, Oxford, England, 1974).

XI. ACKNOWLEDGMENTS

The author wishes to express his special appreciation to his major professors, Dr. R. A. Danofsky and Dr. R. G. Brown for many helpful discussions and suggestions, and encouragement throughout the course of this research. In addition, the author is indebted to Dr. R. A. Hendrickson for discussing and reviewing the safety analysis of the experiment; to the reactor operating staffs of the ISU UTR-10 reactor for assistance in reactor operation; to Mr. Mikdam Saleh for his help in the data acquisition system. Finally, the author is deeply grateful to his wife, Chi-Yun, for her understanding through the years of study.

XII. APPENDIX A: INPUT DATA PREPARATION AND THE OUTPUT DESCRIPTION OF THE WHIRLAWAY-H CODE

A. The Input Data Preparation

Given below are the instructions for writing WHIRLAWAY-H input. Note that the formats are given in the parentheses immediately following the input cards (unless otherwise specified). A schematic diagram for a three-dimensional cube is given in Figure A.1 for reference.

1. Title card (20A4)

   : The title of the problem

2. Tape control card (2I5)

   NRTAPE = 0 Use the initial fluxes distribution provided by the code

   = 1 Read the initial fluxes from tape #11

   = 2 Read the initial fluxes from tape #12

   NNTAPE = 0 The converged fluxes are not written in any tape

   = 1 the converged fluxes are written on tape #11

   = 2 the converged fluxes are written on tape #12

3. Adjoint source specification card (I10, 2F10.0, I10)

   NNORM = 1 the flux and/or adjoint flux are normalized with respect to the maximum flux or adjoint flux

   = 0 the flux and adjoint flux are normalized to the total fission source.

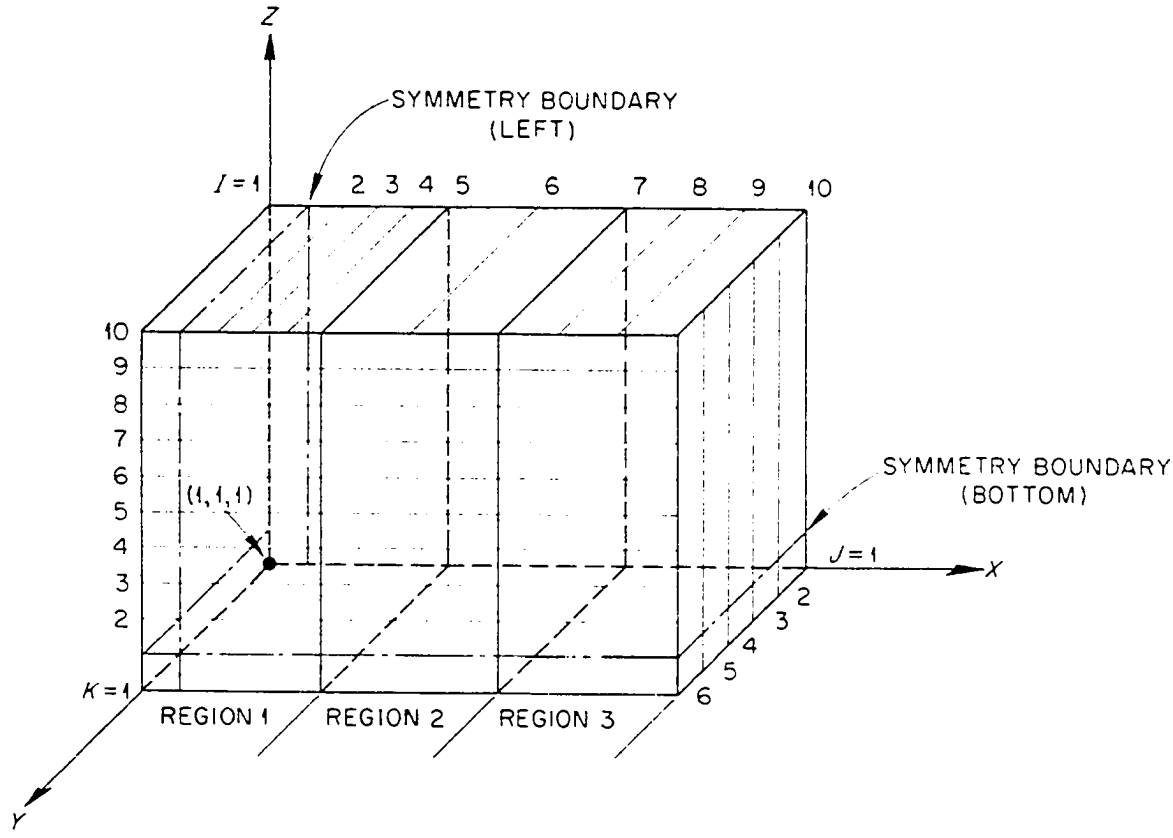

Figure A.1. The schematic of the three-dimensional cube used in WHIRLAWAY-H

SIGMD1: the fast adjoint source, usually the detector cross section for fast group, cm^{-1}

SIGMD2: the thermal adjoint source, usually the detector cross section for thermal group, cm^{-1}

NGEMW: the external neutron source region index number. If no external source is used, put NGEMW equal to 0

4. Graph plotting control card (24I3)

NPLOTI $\leq$ 3: Number of curves to be plotted in X direction

NASJ1, NASK1, NASJ2, NASK2, NASJ3, NASK3
: The first two specify the mesh index of Y plane and the mesh index of the Z plane for the first curve in X direction. The following four numbers specify the second and third curve in X direction

NPLOTJ $\leq$ 3: Number of curves to be plotted in Y direction

NAK1, NAI1, NAK2, NAI2, NAK3, NAI3
: These six mesh index specify the three curves in Y direction

NPLOTK $\leq$ 3: Number of curves to be plotted in Z direction

NNAI1, NNAJ1, NNAI2, NNAJ2, NNAI3, NNAJ3
: The six mesh index specify the three curves in Z direction

5. The graph size card (2F10.0)

XSIZE: The graph size in inches for X-axis

YSIZE: The graph size in inches for Y-axis

If no graph plotting is required, discard the Graph plotting control card and the graph size card. Put two blank cards after the adjoint source specification card.

6. The control card (3I3, E9.5, 11I2, 4E6.3, E8.5)

IMAX $\leq$ 999: Total number of mesh points in the X direction

JMAX $\leq$ 999: Total number of mesh points in the Y direction

KMAX $\leq$ 999: Total number of mesh points in the Z direction

NORM FACTOR: Not used

G1: Geometrical indicator. This number is not used

S1 = 1 Source calculation is applied

= 0 Source calculation is skipped

A1 = 1 Adjoint flux and flux-adjoint flux regional integrals are calculated

= 0 Adjoint calculation is skipped

F1: Not used

C1 = 0 The total λ convergence criterion is used to stop the calculation

= +1 The total λ convergence criterion and the flux convergence criterion are both used

= -1 The point $-\lambda$ convergence criterion and the flux convergence criterion are both used

LB = 0 Left boundary is a zero flux boundary

= 1 Left boundary is a symmetry boundary

RB = 0 Right boundary is a zero flux boundary

= 1 Right boundary is a symmetry boundary

IB, OB, BB, TB: Specify the 'in', 'out', bottom and top boundary conditions as described in LB and RB

χ1: Fraction of neutrons produced from fission that are born in group 1

$\chi 2$: Fraction of neutrons produced from fission that are born in group 2

$\beta 1$: Extrapolated Liebmann coefficient for group 1

= 0 $\beta 1$ computed by the code

= 1 $\beta 1$ provided by the user

$\beta 2$: Extrapolated Liebmann coefficient for group 2

= 0 $\beta 1$ computed by the code

= 1 $\beta 2$ provided by the user

ε: The value for convergence criterion

7. Mesh specification cards

Described below are the three types of cards required to specify the mesh: (1) cards giving the ΔX's and l numbers, (2) cards giving the ΔY's and j numbers, and (3) cards specifying the ΔZ's and K numbers.

1. In columns 1-6 and 7-9, 10-15 and 16-18, etc., supply a value of ΔX (E6.3) and the value of l(13) up to which this ΔX applies, going from left to right of the mesh. Use as many cards as needed, with each card, except possibly the last, being completely filled through column 72. The last number on these cards is equal to lMAX.

2. In columns 1-6 and 7-9, 10-15 and 16-18, etc., supply a value of ΔY(E6.3) and the value of j(13) up to which this ΔY applies, going from "in" to "out" of the mesh. The last number on these cards is equal to JMAX.

3. In columns 1-6 and 7-9, 10-15 and 16-18, etc., supply a value of ΔZ(E6.3) and the value of K(13) up to which this ΔZ applies, going from bottom to top of the mesh. The last number on these cards is equal to KMAX.

8. Region specification cards

The regions are specified as parallelopipeds, with each card completely specifying one region, for as many regions as are needed to fill the mesh. The region-specification cards may be in any order. However, the regions must be numbered consecutively. One card with the number 99 punched in columns 1 and 2 must follow the last region-specification card.

Columns 1-2, KG(12)	Region number
Columns 3-5, I1(13)	Left I coordinate of the region
Columns 6-8, I2(13)	Right I coordinate of the region
Columns 9-11, J1(13)	"In" j coordinate of the region
Columns 12-14, J2(13)	"Out" j coordinate of the region
Columns 15-17, K1(13)	Bottom K coordinate of the region
Columns 18-20, K2(13)	Top K coordinate of the region
Columns 21-26, D_1(E6.3)	Group 1 diffusion coefficient
Columns 27-32, D_2(E6.3)	Group 2 diffusion coefficient
Columns 33-40, ΣR_1(E8.5)	Group 1 macroscopic removal cross section
Columns 41-48, ΣA_1(E8.5)	Group 1 macroscopic absorption cross section
Columns 49-56, ΣA_2(E8.5)	Group 2 macroscopic absorption cross section
Columns 57-64, $\nu\Sigma f_1$(E8.5)	Group 1, ν times the macroscopic fission cross section
Columns 65-72, $\nu\Sigma f_2$(E8.5)	Group 2, ν times the macroscopic fission cross section

B. The Output Description

The output consists of the items shown below:

1. Title

2. Reactor specifications

3. Mesh specifications

4. Dimension specifications

5. Region specifications

6. The values of the extrapolated Liebmann coefficients

7. Flux convergence, point-λ convergence, total-λ convergence, total residue, and λ (labeled NU-CRITICAL) at every tenth iteration. The total residue is calculated as the square root of the sum of the squares of the residues (summed over all points and groups) divided by the total source.

8. The normalized flux values for each group at each mesh point

9. A neutron-balance list calculated from the printed-out fluxes

10. A summary of the region-integrated group absorptions and the region volumes

11. The source density at each octant of each internal mesh point

12. A summary of convergence levels for the adjoint calculation

13. The normalized adjoint-flux values at each mesh point

14. The flux times the adjoint-flux region integrals and the region integrals of the dot products of the gradients of the flux and the adjoint flux

    For one region, the printout would be as follows:

    REG PHI(1)XPH1(K)* PHI(2)XPH1(I)* DELPH1(KO·DELPH1(K)* K=1,2

    $$\int \phi_1 \psi_1 d\vec{r} \qquad \int \phi_2 \psi_1 d\vec{r} \qquad \int \Delta\phi_1 \nabla\psi_1 d\vec{r}$$

    $$\int \phi_1 \psi_2 d\vec{r} \qquad \int \phi_2 \psi_2 d\vec{r} \qquad \int \nabla\phi_2 \nabla\psi_2 d\vec{r}$$

15. The plots for fluxes and/or adjoint fluxes distribution along X, Y, or Z direction.

XIII. APPENDIX B: THE UTR-10 REACTOR AND THE CALCULATED MACROSCOPIC PARAMETERS FROM LEOPARD

The UTR-10 reactor core region consists of two core tanks. Each core tank contains six fuel elements and each fuel element contains twelve fuel plates which are made of 93.25% enriched uranium. The fuel plate is 40 mils of UAl_4 + Al fuel matrix clad on each side with 20 mils of aluminum. The water gap between the fuel plates is 0.4 inch. The dimension for each fuel plate is 26 in x 3 in x 0.04 in (66 cm x 7.6 cm x 0.1 cm).

Using these data, a volume fraction of 0.975 was calculated for the fuel matrix. The U-235 concentration in the fuel matrix was calculated as 0.001168×10^{24} atoms U-235/cm^3, and a U-238 concentration of 0.0000081×10^{24} atoms U-238/cm^3 was obtained. In the cell calculation, an extra region of 14.86% was added to take account of the aluminum tanks and dividers in the fuel region.

The two-group macroscopic parameters were calculated using LEOPARD based on the specifications given in the previous paragraph. The sample input data to LEOPARD for different regions are given in Appendix C. The calculated two-group macroscopic constants for different regions are given in Table B.1 through Table B.4.

Table B.1. Macroscopic parameters for the fuel region of the UTR-10 at a coolant temperature of 90°F and no voids

Energy Group	D	$(\Sigma_s)_{i\rightarrow i+1}$	Σ_a	$\nu\Sigma_f$
1st group	2.30847	0.0813495	0.0016907	0.00026532
2nd group	1.163952	0.1066567	0.00024492	0.0003347
3rd group	0.774892	0.1047691	0.0045654	0.00510796
Combined fast group	1.421447	0.341292	0.0019626	0.00186632
Thermal group	0.231576		0.0524102	0.07640672

Table B.2. Macroscopic parameters for the graphite reflector region

Energy Group	D	$(\Sigma_s)_{i\rightarrow i+1}$	Σ_a	$\nu\Sigma_f$
1st group	2.2393188	0.2388177	0.63324 E-7	0.0
2nd group	1.0509005	0.0103966	6.1601857 E-8	0.0
3rd group	0.9314399	0.00574158	0.88038 E-7	0.0
Combined fast group	1.152864	0.00287363	0.5326368 E-7	0.0
Thermal group	0.991810		0.3066133 E-3	0.0

Table B.3. Macroscopic parameters for water at a temperature of 90°F

Energy Group	D	$(\Sigma_s)_{i\rightarrow i+1}$	Σ_a	$r\Sigma_f$
1st group	2.206438	0.1051795	0.00139486	0.0
2nd group	1.0930185	0.1494903	0.000012605	0.0
3rd group	0.5915430	0.1506139	0.00094565	0.0
Combined fast group	1.322587	0.0483673	0.000797165	0.0
Thermal group	0.1552289		0.01878511	0.0

Table B.4. Two-group macroscopic parameters for various void fractions in water

% Void	D_1	D_2	Σ_{12}	Σ_{1a}	Σ_{2a}	$r\Sigma_{f1}$	$r\Sigma_{f2}$
0	1.322587	0.1552289	0.048367	0.0007971	0.01878511	0.0	0.0
5%	1.3891	0.16296	0.04595	0.000757	0.017841	0.0	0.0
10%	1.4553	0.17072	0.04353	0.0007173	0.0169	0.0	0.0
15%	1.52145	0.1785	0.04111	0.000677	0.01596	0.0	0.0
20%	1.5876	0.1862	0.0387	0.000637	0.01502	0.0	0.0

XIV. APPENDIX C: SAMPLE INPUT DATA TO LEOPARD

LEOPARD, a zero-dimensional cross section code, was used to calculate the two-group macroscopic parameters of the UTR-10 reactor. The sample input data to LEOPARD, used in the modeling calculation, for different reactor regions are shown below.

1. Fuel region of UTR-10

```
 1  0  1  2  1  1  1          0          -2   0

          9  0.975      1.0      0.0        1.0
         18  0.001168   0.0      0.0        0.0
         20  0.000085   0.0      0.0        0.0
        777  0.0        0.0      0.0        0.0
        777  0.0        0.0      0.0        0.0
        90.  90.  90.   90.      0.00194    1.0
        0.02 0.04 0.48                      0.1486
        14.7
```

2. Graphite region

```
          4  0.9999     0.9999   0.9999     0.0
        100  0.00001    0.00001  0.00001    0.0
        777  0.0        0.0      0.0        0.0
        777  0.0        0.0      0.0        0.0
```

3. Water region

```
        100  1.0        1.0      1.0        0.0
        777  0.0        0.0      0.0        0.0
        777  0.0        0.0      0.0        0.0
```